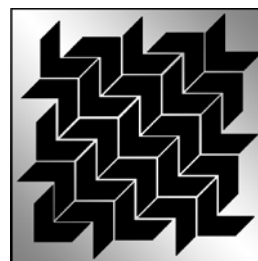UNIVERSITY OF MILANO-BICOCCA

Department of Materials Science

PhD School in Nanostructures and Nanotechnologies

NANOPOROUS DIPEPTIDE CRYSTALS
AS SELECTIVE GAS SORBENTS AND
POLYMERIZATION NANOVESSELS

Supervisor: prof. Piero SOZZANI

PhD Thesis

Gaetano DISTEFANO

Matr. Nr. 049408

Academic Triennium 2009-2011

Acknowledgements

As I'm approaching to the end of the doctoral triennium, I feel the urge to express my gratitude to all the people directly or indirectly involved in my research. I wasn't alone in this enterprise and the results presented herein were achieved with the help of many.

*   *   *

Generally, those people remembered in the second page of the Acknowledgements are the most important. This isn't an exception. They are those who silently bustle in the "rear lines" and their contribution makes life much pleasant.

Thanks to all the friends of the Materials Science department, Sozzani group members and undergraduate students (present and past) and all GCS members. Thank you for the good time spent together in our U5 building. Thanks to my brotherly friends, who providentially show up and make me smile even in the hardest times.

Thanks to my family: Dad, Chiara and Doni, Salvo and Alessandra, together with my relatives in Sicily, for always being there. You definitely give more than you get and this makes me feel grateful, indebted and irremediably selfish. Thanks to the "other" family, too: Elia, Gina and Paola. Truly, without you all (and Mum from Above) I wouldn't even know who I am.

And thank you, Chiara. Time has passed since "last time" but you are still there, cheering me up and supporting me as always. Thank you for your patient love that can turn long faces into the joy of being together.

Bergamo, 20th December 2011

Preface

"But still we are blind […]: blind, and we don't have those small tweezers, that we often dream of at night like a thirsty person dreams of wellsprings, that would allow us to take a segment, hold it firmly and straight, and to correctly paste it on the segment that is already assembled. If we had those tweezers (and it's not said we won't have them one day) we would have already managed to do some nice things only God could do, for instance assemble, if not a frog or a dragonfly, at least a microbe or the seed of a mold."

Primo Levi, "*The Wrench*", 1978

One of the most sought goals of both physicists and chemists is the fine control over matter. For instance, the ability to manipulate single molecular fragments would enable, as the inspiring excerpt cited above suggests, the easy assembly of complex molecules, or the building of exotic structures and devices that cannot be produced by ordinary chemical procedures.

What Levi envisages in his "thought experiment" is nothing but a kind of nanotechnology imagined before the invention of the word nanotechnology itself. In fact, nanotechnology (and nanoscience), namely the interdisciplinary field of science dealing with phenomena emerging when matter is organized at lengths of a billionth of a meter, requires the ability of building organized structures with molecular precision.

During the last forty years, as the conceptual basis for molecular manipulation developed in the scientific community and the appropriated tools were discovered (such as electron or tunnel microscopies), the gap between macroscale and nanoscale was filled and nanotechnology, as an autonomous scientific field, was born. At the same time, the distance

between imagination and reality was reduced: out of metaphor, to the today reader, Levi's *small tweezers* closely remind of the famous STM tip which spelled "I B M" moving individual atoms on a metal surface. Indeed, what once dwelled in the domain of imagination, now has become more familiar.

However, the realization of chemical reactions using an STM tip (or Levi's *small tweezers*) would be useless and frustrating if molecules were manipulated one at a time. In this regard, nanoporous materials (with pore diameter around the nm) can be the key to the manipulation of large amounts of molecules at once: for instance, exploiting the nanometrically tailored interactions between the nanocavities of the host material and guest molecular species. More than *small tweezers*, nanoporous materials provide an enormous array of *small baskets* where guest can be accommodated. Such *small baskets* would also amplify the phenomena occurring in the nanoscale, making them easily detectable on the macroscale (without the need of a scanning tunnel microscopy, for instance).

A class of promising nanostructured materials is the one of peptides (Chapter 1). Living beings (even the "seed of a mold") are extremely complex chemical entities that would require highly sophisticated tools to be "synthesized". Indeed, living systems are built by proteins: structural and functional components of living beings are made by polypeptides and natural materials biosynthesis (most of which have nanometer order) are directed by enzymes. In the quest of novel materials, peptides play an important role because their ubiquitous presence and immense variability sparks a learning process that, from the characterization and understanding of natural proteins, leads to the development and synthesis of compounds with desired nanostructures. In this frame, the systematic structural investigation of short peptide crystals serendipitously lead, in the last fifteen years, to the discovery of a new family of materials with permanent nanoporosity: the dipeptides the title of the present work addresses.

Such biologically inspired compounds, presented in the first Chapter, are able to self-assemble by means of hydrogen bonds and form architectures having channels with diameter in the sub-nanometer domain: therefore, they provide a suitable environment to molecular species.

It is known that nanoporous materials can be employed in a large number of applications, such as catalysis, gas storage and separation, nanovessels or host for functional molecules. In a

certain sense, all these applications can be reduced to holding "firmly and straight" molecules in order to perform desired chemical reactions, to selectively bind gas molecules, to impart anisotropy to functional guests.

For instance, it is possible to take advantage of the differential affinity between gases and the dipeptide nanopores to attain selective gas sorption. In fact, dipeptide channels, whose sizes match the size of a methane and carbon dioxide molecules, could be effective in distinguishing CO_2 from CH_4, achieving gas separation (as discussed in Chapter 2). Instead, in Chapter 3 is discussed the use of dipeptides as polymerization nanovessels: taking advantage of the affinity between dipeptide pores and monomer molecules and exploiting the pore linear geometry, it was investigated their influence on radical polyadditions reactions. The attaining of polymer microstructures impossible to obtain under ordinary conditions (bulk or solution) was the main objective. Moreover, nanopores can be used not only to control the macromolecular microstructure but also to imprint anisotropic properties to the guest, as discussed in Chapter 4, where the fabrication of polymer (and carbon) microfibrils is described.

Moreover, this thesis tries to give a contribution to the better understanding of these novel peptide-based materials not only as tools to perform molecular manipulation (Chapters 2, 3 and 4) but also from the point of view of their general chemico-physical properties (Chapter 5).

In conclusion, this thesis represents only a tiny contribution to the choral scientific effort aiming at the fine control over matter Levi's chemist longed for. However, cross and delight, the domain of dreams is intact and continuously inspires scientists to stubbornly persist in their enterprises. With humility and the awareness of its perfectibility, the author delivers this work, hoping that his efforts will be appreciated by the reader.

Contents

Contents

Contents

Contents

Contents

Chapter 1 – Peptide Materials

1.1. Introduction

Naturally available materials have been used since ages by mankind. Our ancestors created their tools using, beside stone and metals, wood and bark, horn, shells and bones, sponges, cotton, wool, fur, silk, rubber, leather and so on. Not only man used natural materials produced by other living beings, but man himself is *made* by natural materials: bones, tendons, muscles, cartilage, skin *et cetera* are all examples of biological materials we are all formed of and, unaware, *use* every day, since the dawn of times.

Natural materials evolved together with living beings because their performances could determine the survival of an individual against natural selection, and individuals made of or producing the most suited materials had a higher chance of surviving and reproducing. For instance, those individuals having stronger shells, warmer wool and more flexible wood could better resist the attack of predators, survive cold winters or not being torn apart by storms. Indeed, when manufacturing our tools, clothes and houses, we borrowed evolved materials from other living beings, adapting their natural functions to our needs.

Among all the biochemical compounds, proteins play a pivotal role in biological materials "manufacturing": they allow for enzymatic biosyntheses, direct bio-mineralization and

constitute tissues. As known, proteins are macromolecules obtained by the copolymerization of the twenty natural amino acids: the potentially endless combinations of amino acids in affording the protein primary structure (the amino acid *sequence*) reflects into the enormous variability of hierarchically self-assembled structures (so called *secondary*, *tertiary* and *quaternary* structures) which ultimately define the protein's three dimensional shape and therefore its physiological function. Primary structure endless variability was domesticated by Nature through evolution: genetic code represents the proteins' *blueprint* and evolution acts on DNA's mutations in order to select those genetic sequences coding for proteins which eventually offer marginal increase of *fitness* in the host bearing the mutation. Million years of natural evolution produced proteins and natural materials man used since his appearance on Earth.

Proteins' properties depend on their organization at the nanometer scale: spider silk, for instance, owes its strength to its unique hierarchical nanophase self-assembly[1]; on the other hand, biological signaling (e.g. insulin[2]) and enzymatic biosynthesis (e.g. DNA polymerases[3]), are mediated by cooperative and complementary supramolecular interactions which are enhanced by the precise arrangement of amino acid residues in space. Moreover, dynamical behavior of proteins makes them suited candidates for the realization of "smart materials", namely materials which can adapt to external *stimuli* in a reversible way, since proteins can respond to changes in solvent conditions (pH, salt concentration), temperature, light, oxidation states, the presence of metals and other more complex ligands[4]. Combining space patterns (nanostructures) together with time patterns (dynamic behavior) is a challenge in modern materials science and that's the reason why many scientists undertaking the task of novel materials discovery devoted their efforts to proteins (or better peptides) in order to exploit their potential: learning from Nature, using its building blocks and self-assembly motifs and, at the same time, speeding up natural selection through design[5].

Human civilizations are named after materials (the Stone, the Bronze, the Iron, the Plastic and the Silicon ages); curiously, none of these "ages" are called after a biological material (there isn't any "Wool", "Wood" or "Bone" age) since the historical classification points out the technological milestones that where set, rather than the materials actually used. But as scientists will master protein synthesis and self-assembly, a "Protein Age" could finally

disclose, where biologically inspired materials will emerge and become fundamental for future society.

1.1. Amino acids and supramolecular interactions

The structure of an amino acid is shown in Fig. 1: natural amino acids feature a carboxylic acid functionality at the C *terminus* of the molecule while, the N *terminus* is constituted by an amine group. The structurally variable position in an amino acid is the central carbon (α-carbon) to which the side chain (-R) is attached. When -R is different than a mere proton (as in the case glycine), the α-carbon is stereogenic, and a pair of enantiomers can be produced (L- or D- amino acids); in case of proteogenic amino acids, the L- form prevails, being the absolute configuration that was selected by biochemical evolution. Polypeptides are formally obtained by the condensation of the C *terminus* of an amino acid with the N *terminus* of the following one in the peptide sequence, forming a peptide (or amide) bond and giving the primary structure an overall directionality.
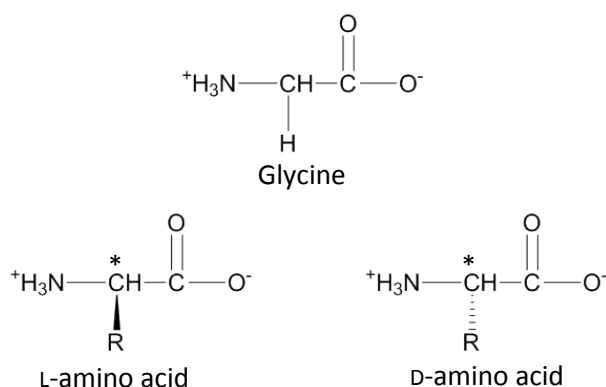
Fig. 1 – General structures of amino acids. Glycine (top) is the only non-chiral natural amino acid, while amino acids substituted in the α position generate two specular entaniomers (bottom)

While polypeptide's primary structure is based upon covalent bond, namely the peptide link between terminal carbon and nitrogen between two adjacent amino acids, hierarchically higher structures are built upon supramolecular forces that can act on an intramolecular (secondary and tertiary structure) or intermolecular (quaternary structure) basis. Supramolecular bonds are weaker than covalent ones when considered singularly but supramolecular interactions acting synergistically can reach considerable binding energies on

the whole. Among supramolecular interactions we can enlist hydrogen bonding, Van der Waals and electrostatic interactions (mediated by polarity or ionic charges), π-stacking, ion complexation; each interaction feature different properties such as angle dependence or directionality, distance decay and binding energy, as reported in Table 1.

Table 1 – Summary of the most relevant properties of supramolecular interactions

	Effect	Bond energy / kJ mol^{-1} per bond	Distance dependence	Angular dependence
Hydrogen bond	Attractive	4 - 120	$1/d^4$ - $1/d^6$	Yes
Electrostatic interactions	Attractive (opposite charges) or repulsive (same charges)	50 - 200	$1/d^2$	No
Dipole-Dipole	Attractive (antiparallel) or repulsive (parallel)	5 - 50	$1/d^3$	Yes
Coordination	Attractive	5 - 80	discrete bond distances	Yes
π- π interaction	Attractive and repulsive depending on arrangement	~ 8	complex	Yes
Van der Waals	Attractive	0 - 5	$1/d^6$	No

All the supramolecular interactions are potentially represented in a polypeptide chain since the twenty proteogenic amino acids bear side chains capable of participating in various recognition patterns (Fig. 2). Moreover, polypeptide backbone provides additional hydrogen bonding moieties (amide functionalities) which mainly promote secondary structure assembly. The range of supramolecular interactions can be further extended with the introduction, in a peptide chain, of non-proteogenic, artificial, amino acids provided with side chains with tailored supramolecular properties[6]. Finally, some natural amino acids (such as aspartic acid, glutamic acid and cisteine) have functional groups that can easily be modified using ordinary organic chemistry, paving the way to the so called "peptide conjugates", that combine peptides to non-peptide building blocks[7].
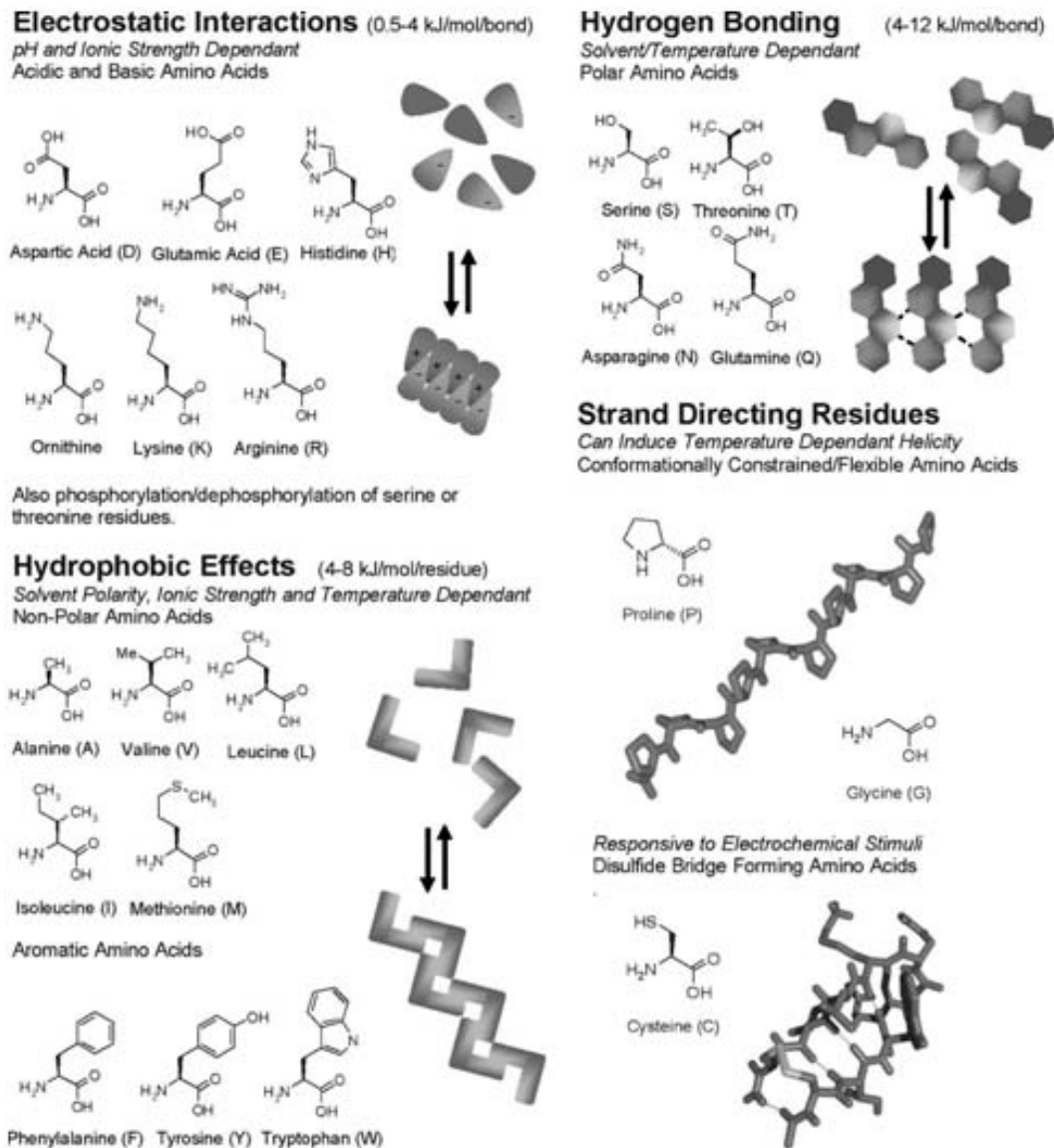
Fig. 2 - Schematic descriptions of different classes of amino acids and the types of peptide interactions they are involved in (the twenty-first amino acid ornithine is a non proteigenic amino acid). Adapted from Ref. [8]

1.2. Polypeptides, proteins and peptides

A polypeptide is a linear biopolymer obtained by the connection of the twenty natural amino acids through peptide bonds. The polypeptide's biological synthesis occurs in the cell where genes are expresses and translated into polypeptides through a complex biochemical mechanism: amino acids are assembled one after the other to yield the final polymer whose length and sequence (the so called *primary structure*) are precisely controlled by genetic code.

The distinction between polypeptides and proteins resides in the biologically functionality of the latter, which is often obtained upon polypeptide folding and combination with non-protein ligands. In fact, the linear polypeptide self assembles locally into well defined structural motifs (α-helix, β-strand, β-turn *etc.*) to afford the *secondary structure*; the so called *tertiary structure* represents how secondary structure motifs are arranged in space and is completely described by atomic positions; finally, *quaternary structure* arises from the aggregation of multiple folded polypeptides. Tertiary and quaternary structures are the functional form of polypeptides in living beings and are therefore addressed as proteins: they accomplish several tasks such as physiological regulation and signaling, enzymatic synthesis, chemical transport and storage, together with structural functions (they are present in the cytoskeleton, in ligaments and tendons, muscles, bones). Functional proteins can be inactivated by *denaturation*, namely changing the physiological environment of the protein (salt concentrations, pH, temperature, solvent) in order to destroy its assembly, thus leading to a loss of functionality, with the adoption of *random coil* conformation by the linear chain.
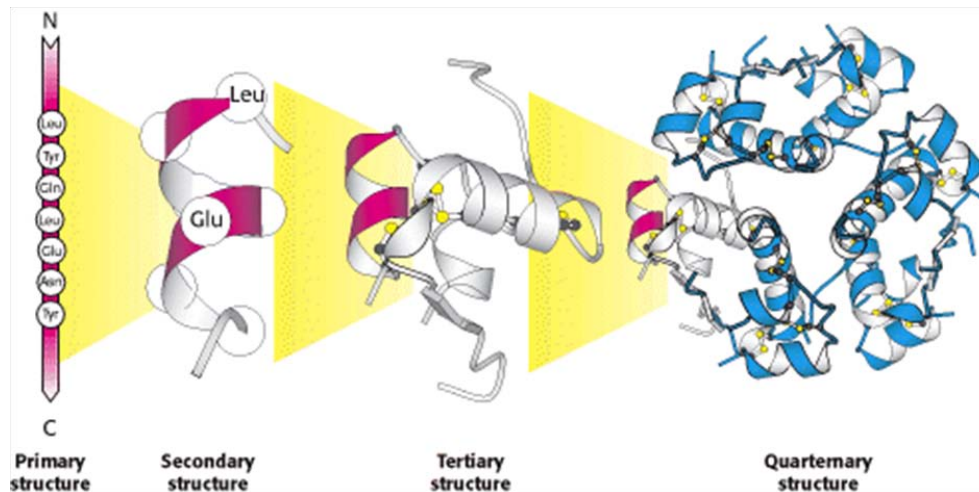
Fig. 3 – Hierarchical self-assembly of insulin protein (adapted from Ref. 9)

Folded proteins are classified in two mutually exclusive classes: globular proteins and fibrous proteins. Globular proteins (or *spheroproteins*) are soluble in aqueous medium, such as physiological solution present in living beings, where they form colloidal suspensions. In their tertiary structure, hydrophobic amino acids are buried in the molecular interior, while

hydrophilic amino acids point towards the external surface, allowing water solubility. Globular proteins generally act as enzymes, messengers, transporters, stock of amino acids and fulfill regulatory functions. On the other hand, fibrous proteins (also called *scleroproteins*) are insoluble and adopt anisotropic fibrillar arrangement (keratin, collagen, elastin and fibroin are some examples) covering structural functions (mainly protection and support). Fibrous proteins are insoluble in water and aggregate due to hydrophobic interactions; in addition, covalent cross-links can occur and enhance their stability.

The definition of *peptides* is purely formal and, according to an accepted criterion, are called *peptides* those polypeptides which do not exceed 50 amino acid residues in length; according to another operational definition, peptides are those polypeptides *short enough* to be synthetically obtained in the laboratory. It is evident how the latter definition is ambiguous and prone to shift peptide definition towards higher molecular weight as synthetic strategies are improved. For our purposes, we will adopt the term *peptide* when referring to synthetic polypeptides while use the term *protein* in case of naturally occurring polypeptide chains preserving their functional integrity.

1.3. Self-assembly motifs in polypeptides

Polypeptides' secondary structures can adopt various arrangements mainly leading to α-helices, β-sheets and β-hairpin with different structural features.

α-helices (Fig. 4) are a key secondary structure of peptides, characterized by a single, spiral chain of amino acids stabilized by intra-molecular hydrogen bonds. Peptide chains which form α-helices exhibit amino acids of similar character every three or four residues and lead to helices with 3.6 amino acids per helical turn. Moreover, opportunely designed peptides can be provided with additional complementary recognition sites on the outer surface of the helix, leading to so called *coiled-coils*. β-sheets instead are formed by adjacent parallel or anti-parallel arrangement of peptide strands involved in inter-molecular hydrogen bonds. β-sheets are frequently stable and this stability is often related to protein-accumulating diseases such as Alzheimer's and Parkinson's diseases. Another secondary structure available to peptides is the β-hairpin, where the polypeptide chain turns on itself, leading to intra-molecular hydrogen bonding between consecutive segments of the peptide chain. β-hairpin occurs when an amino

acid sequence contains a pair of turn-inducing residues such as proline followed either by glycine or threonine.
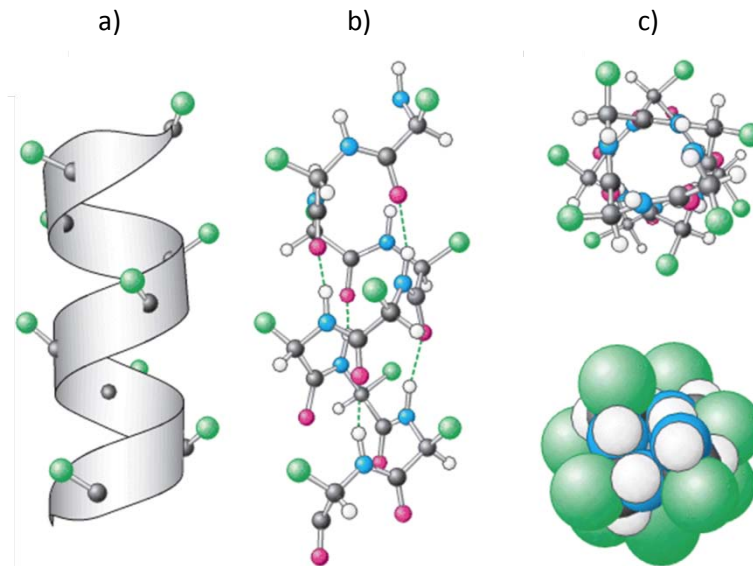
Fig. 4 – α-helix secondary structure. a) helical conformation and protrusion of amino acid side chains (in green), b) ball-and-stick representation highlighting intermolecular H-bonds and c) view along the helix axis (ball-and-stick and Van der Waals volumes). Adapted from Ref. 9
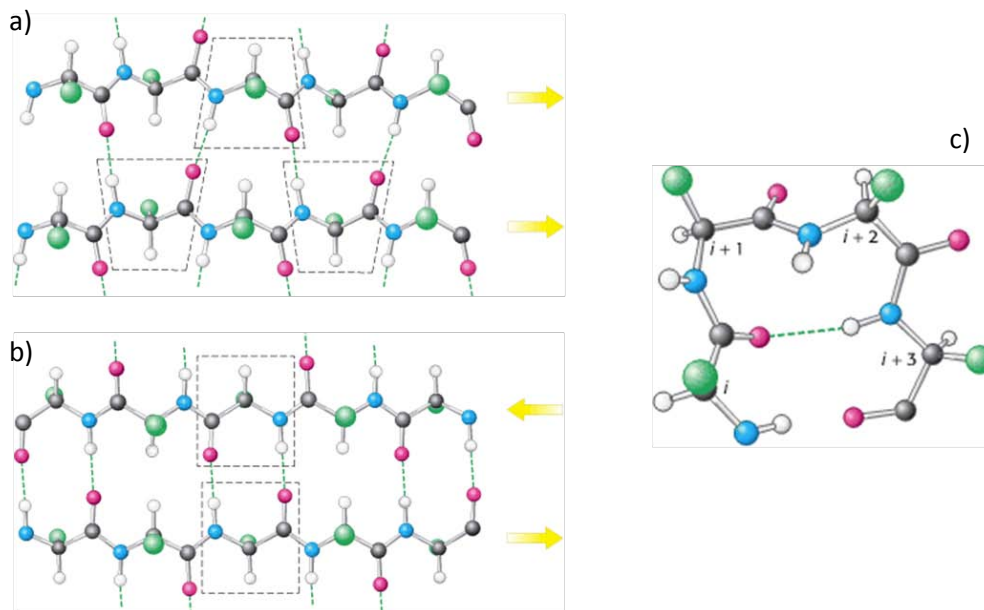
Fig. 5 – β-sheet secondary structure. a) parallel β-sheet, b) antiparallel β-sheet and c) β-turn. Adapted from Ref. 9

1.4. Protein Materials

1.4.1. Natural proteins as nanomaterials

Foreseeing the folding of synthetic polypeptides is, at the present state, an extremely complex task; for this reason one of the strategies used in protein technology consists in employing polypeptides whose structure is already known and that are available in nature, exploiting their native three dimensional shapes and functions for *ex-vivo* applications. These materials can be processes by techniques that are normally employed for synthetic materials (such as coating, electro-spinning, grafting *etc.*), regardless their natural origin.

This approach is particularly indicated where biocompatibility (and bioactivity) is a stringent requirement, like in tissue engineering where recreating the ideal conditions for cell growth is imperative. In this regard, elastin is a unique example of a protein derived from natural sources which is manipulated artificially to confer special properties to the final materials and devices[10]. In fact, elastin is a component of the extracellular matrix (ECM) in tissues which require elasticity as part of their function (skin, lungs, vasculature). Moreover, it is part of the core architecture which supports cell growth and bestows signaling functions to tissues, promoting responses including chemotaxis, cell growth and tissue homeostasis[11]. Elastin was then used as coating for polymer biomaterials and metallic implantable devices (stents and heart valves), in order to promote cell adhesion[12] and to reduce inflammation and blood coagulation[13], respectively. Electrospinning can be used to spin elastin (together with collagen and polyethyleneoxide, PEO) and produce three dimensional porous scaffolds where smooth muscle cells (SMC) were successfully grown, yielding an engineered construct which mimics blood vessel tissue[14].
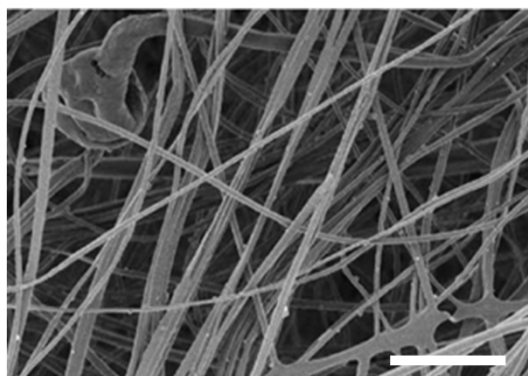
Fig. 6 – Multi-component electrospun fibers of elastin-collagen-PEO. Scale bar equals 10μm (adapted from Ref. 14)

Already existing proteins can also be used as nanoreactors, exploiting their *in vivo* storage function. For instance, ferritin protein naturally stores iron as crystallites in a cavity with well defined dimensions (7 nm cross section) and is suitable to synthesize monodisperse iron and cobalt oxides crystals[15]. Based on this approach, various inorganic nanoparticles such as quantum dots, metal oxides, transition metals and metal alloys have been synthesized in ferritin cages[16]. Similarly, urease was used to template monodisperse Ag_2S nanocrystals in aqueous solution[17].

A remarkable example of the deep interconnections between molecular biology, nanotechnology and materials science is provided by virus capsids. Virus capsids are well-defined monodisperse cages, formed by the precise self-assembly of proteic subunits, which contain the viral genetic code. A capsid, freed from the virus genome, can be used as nanocontainer for various purposes. For instance, the cowpea chlorotic mottle virus (CCMV) is an icosahedral virus whose capsid has a 18 nm diameter inner cavity; upon suitable stimulus (a change in pH) the capsid is able to swell, becoming permeable to guests which, after de-swelling, are trapped in the nano-cavity: using this approach it was possible to introduce molecular tungstate anions (WO_4^{2-}) which then mineralize in the capsid yielding ~15 nm diameter oxide crystals[18] (Fig. 7).
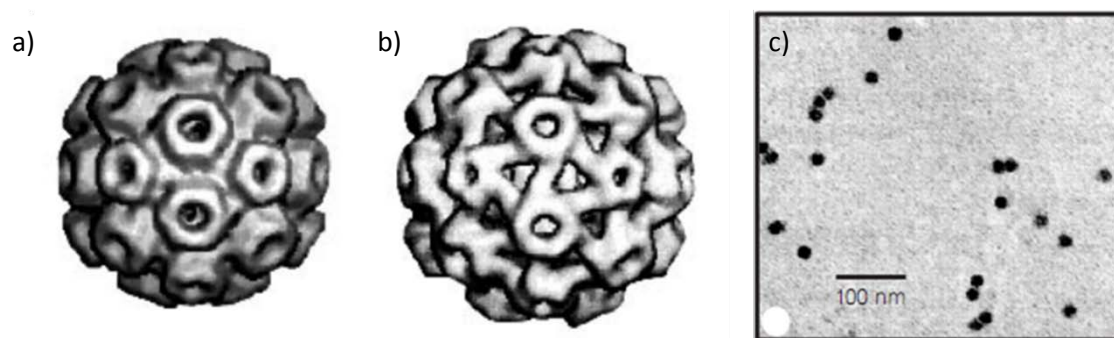
Fig. 7 – Cryo-electron microscopy and image reconstruction of a cowpea chlorotic mottle virus (CCMV) in a) unswollen (low pH) and b) swollen (high pH) state. c) TEM image of paratungstate-filled virus capsids. (Figures adapted from Ref. 18)

Bio-inspired mineralization utilizes natural small proteins which are involved in the *in vivo* growth of inorganic phases. For instance, calcification-associated-peptide (CAP-1), which is isolated from the crayfish exoskeleton, can be used to prepare uniaxially oriented thin-films crystals of calcium carbonate on chitin matrices[19]. In another example, silicateins, a class of enzymes involved in biomineralization processes, promoted the sol-gel room temperature synthesis of titanium dioxide[20].

It is also possible to take advantage of the spatial extension of proteins which are objects spanning the mesoscale. By crystallizing globular proteins it was possible to build porous crystals[21]; in fact, due to their spherical shape, these macromolecules pack inefficiently, leaving empty pores which are filled by solvent molecules. Pore size and distribution is controlled by crystalline structure and taking advantage of the rich polymorphism of proteins it is possible to select crystallization condition yielding the desired phase and uniform pore properties (with pore sizes beyond those attained by inorganic zeolites). Thermolysin, lipases, human serum albumin (HSA) and bovine serum albumin (BSA) were used for this purpose. Chemical cross-linking between proteins in protein crystals confer additional stability to external stresses (both chemical and mechanical) which these materials undergo in their fields of application (heterogeneous catalysis, enantioselective chromatography, bioremediation)[22].

Moreover, specific interactions between proteins and selected compounds (such as antibodies) can be used to reveal desired analytes, where binding triggers a detectable (e.g. optical or electrochemical) signal. For instance, glucose oxidase (GOx) is, among other

applications[23], used to measure glucose concentration *via* electrochemical detection of oxidation products (H_2O_2)[24].

The aforementioned examples show how already available proteins can be used as found in nature, without severe modifications in their chemical structures. The next paragraph will deal the logical step ahead, namely protein tailoring, which is in the scope of *protein engineering*.

1.4.2. Protein Engineering

The laboratory synthesis of long polypeptide sequences is nowadays out of reach for ordinary synthetic protocols and materials scientists have found alternative strategies for obtaining protein materials in higher yield and more economically than extraction and purification from their natural sources. The strategy is borrowed from biotechnology where *protein engineering* protocols have been developed and transferred to materials science during the last fifteen years. Protein engineering techniques allow the introduction of desired *recombinant* DNA sequences in a host organism (most commonly *E. coli*) which is then used as a bioreactor to synthesize the designed protein, after gene expression activation.[25]

As an example, this approach was applied to the biosynthesis of spider dragline silk of the *Nephila clavipes*. This structural protein is a high performance fiber with high molecular weight (up to 300 kDa) and remarkable mechanical properties (10-50 GPa elastic modulus, 10-30% elongation to break and 1.1-1.4 GPa tensile strength); unfortunately, unlike silkworm silk, there is no readily available source for such an exceptional material.
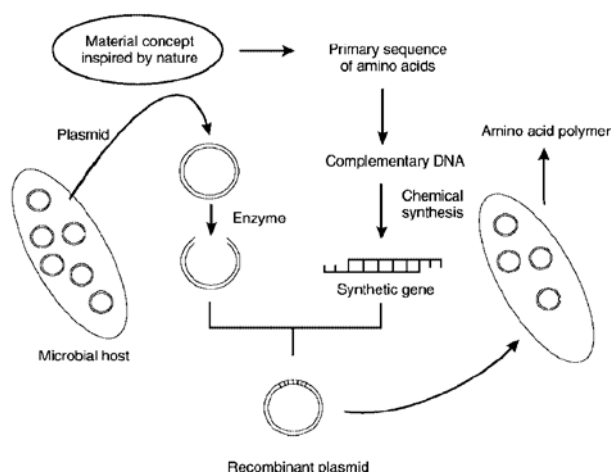
Fig. 8 – Conceptual overview of protein engineering methodology (Ref. 25)

Structural studies on spider silk have elucidated its nanophase composition consisting in crystalline β-sheet domains surrounded by amorphous peptide matrix: using protein engineering, a block copolymer mimicking spider dragline silk was obtained. [26]

Of course, this approach can be extended to smaller peptides for high throughput synthesis, like for the case of recombinant human insulin (51 amino acids) which was expressed in a variety of different organisms, including bacteria, yeast, fungi, mammalian cell cultures and transgenic plants[27].

1.5. Reducing complexity

Nowadays, completely synthetic peptides are obtained mainly by solid phase synthesis, introduced for the first time by Merrifield in his seminal paper[28]. Notwithstanding continuous improvements in the technique lead to higher molecular weight products, the synthesis of long peptides (>50 amino acids) in high yield is still a challenge. As we have seen above, when high molecular weight polypeptides are needed, it is necessary to recur to already available proteins or biotechnological techniques. Anyways, since tertiary structure of *de novo* non-trivial high molecular weight polypeptides is barely foreseeable, such potent synthetic procedures, which are still to come, would be almost useless until computational prediction tools aren't improved.

However, notwithstanding their relative simplicity, synthetic peptides can show a wide range of behaviors, leading to advanced applications, thanks to their intrinsically great structural modularity. In the next paragraphs we will review some relevant peptide nano-materials with an highlight on the shortest peptide materials available, namely dipetides.

1.5.1. Self-assembling peptides

According to a recent review, linear self-assembling peptide materials can be classified in four categories[29].

Type I self-assembling peptides contain alternating hydrophobic and hydrophilic amino acids; when the peptide chain is in elongated conformation, amino acids in odd positions face one side of the molecule while those in evens position face the other side, conferring opposite properties to each side. Moreover, the hydrophilic side of the peptide features complementary ionic charges (e.g. lysine and glutamate, positive and negative charge respectively) which allow for self-recognition through electrostatic interactions in aqueous media, yielding β-sheets aggregates in the shape of interwoven nanofibers[30]. These peptide materials have been used successfully as scaffolds for cell growth and proliferation.

Type II self-assembling peptides are *stimuli* responsive materials derived from Type I peptides. In this case, polypeptide chains can drastically change their secondary structure from β-sheet to α-helix and *vice versa*, leading to modifications in self-assembly capabilities[31].

Type III self-assembling peptides undergo self-assembly onto surfaces, forming covalently attached monolayers which can functionalize and tune the surface properties, making it, for instance, compatible to cell adhesion and proliferation[32].

Type IV self-assembling peptides have surfactant-like structure (hydrophobic amino acid tail with a hydrophilic aminoacid head) and undergo self-assembly to form nanotubes and nanovescicles having 30-50 nm average diameter, similarly to phospholipids[33].
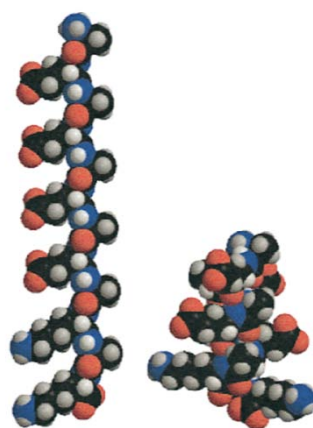
Fig. 9 – Type II self-assembling peptide EAK-12d (AEAEAEAEAKAK, A = alanine, E = glutamic acid, K = lysine) conformations adopted in β-sheet (left) and α-helix (right). Depending on pH or temperature, one if the two forms is favored, leading to the assembly or disassembly of nanostructures (adapted from Ref. 31)

While the above mentioned petide systems employ mainly β-sheet arrangements in a systematic way, also α-helices (coiled-coils)[34,35] and β-hairpins[36] have recently been exploited. Moreover, polypeptide chains accessible conformations can be reduced by the synthesis of cyclic structures where pre-organization can favor self-assembly of the macrocyclic units. In fact, the octapeptide *cyclo*-[(L-Gln-D-Ala-L-Glu-D-Ala)$_2$-] is able to form stacks through antiparallel β-sheet hydrogen bonding, forming ordered hollow tubes with internal diameters of 7.5 Å[37]. The ease of functionalization of the cyclic D,L-α-peptides lead to the discovery of new tubular ensembles bases on this robust self-assembly motif[38].
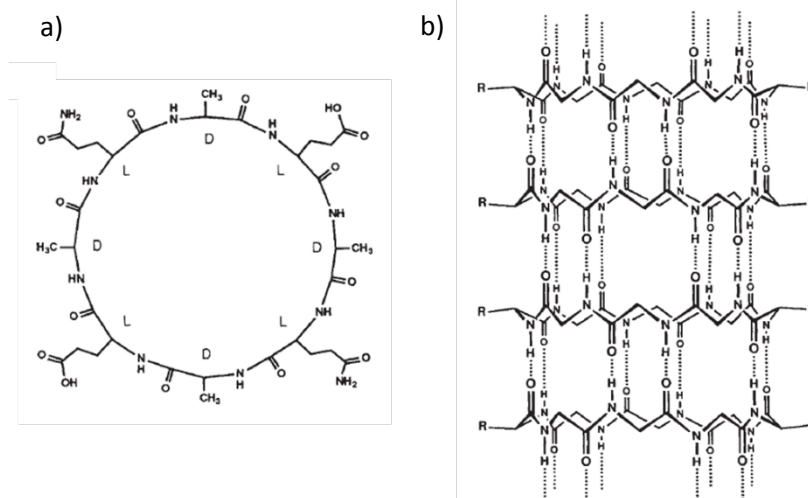
Fig. 10 – a) *Cyclo*-**[(L-Gln-D-Ala-L-Glu-D-Ala)₂-] molecular structure**
b) representation of the extensive network of antiparallel β-sheet-like hydrogen bonds (adapted from Ref. 37)

1.5.2. Dipeptides

In the last decade, a class of low molecular weight peptides has increasingly attracted the interest for their unusual self-assembled structures. In fact dipeptides can afford non-trivial arrangements, despite their simplicity. For instance, recently, phenylalanyl-phenylalanine dipeptide (FF) was associated to the core recognition motif of amyloid fibers in Alzheimer's desease and was found able to form aggregates such as nanotubes[39], nanowires[40] and nanovescicles[41]. π stacking, considered responsible for the generation of such nanostructures, is involved also in the formation of spherical nano-aggregates by phenylglycyl-phenylglycine dipeptide, a close analogue of FF[42]. Similarly, isoleucyl-phenylalanine (IF) is able to self-assemble into an interpenetrated amyloid-like fibrillar structure having the appearance of a transparent hydrogel[43].

1.5.2.1.   Nanoporous hydrophobic dipeptides

Like a protein's higher level structure is dictated by its primary structure, it was found out that the crystal structure of dipeptides can be rationalized and, to a certain extent, predicted by their sequence[44]. During a systematic survey of dipeptide self-assembly, several new crystal structures were discovered having three-dimensional H-bonded networks and stable

nanoporous architectures. In particular, hydrophobic dipeptides are able to form well-defined nanochannels.

In the crystal structures of unprotected, zwitterionic dipeptides, a common hydrogen bond motif corresponds to two -NH$_3^+$···$^-$OOC- head-to-tail chains in a two-dimensional sheet, where the third amino H atom is accepted by a functional group in one of the side chains, or solvent guest molecule. In case of hydrophobic dipeptides, whose side-chains lack H-bond acceptors or donors, such possibility is frustrated, prompting unconventional solutions to the "packing problem"[45].
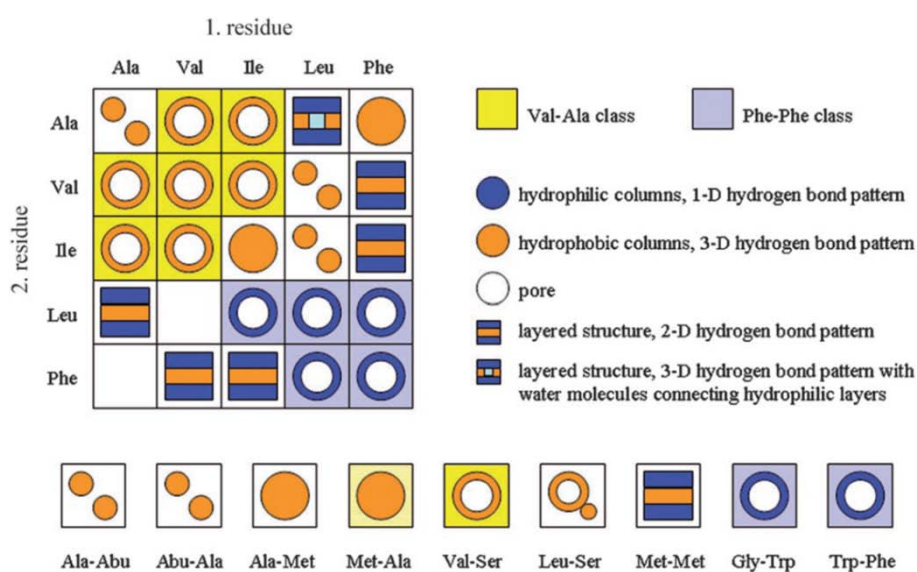
Fig. 11 – Summary of hydrophobic dipeptide structures. Of the 25 pairwise combinations of alanine, valine, isoleucine, leucine and phenylalanine, 12 crystallize in a porous architecture. Seven dipeptides belong to the "Val-Ala class", while five to the "Phe-Phe class", each one having different H-bond patterns and opposite pore hydrophobicity (adapted from Ref. 45).

It was found that seven out of the nine pair-wise combinations of the hydrophobic amino acids L-alanine (Ala, A), L-valine (Val, V) and L-isoleucine (Ile, I) form nanopores. L-Ala-L-Val (AV), L-Val-L-Ala (VA), L-Ile-L-Val (IV), L-Val-L-Ile (VI), L-Ile-L-Ala (IA), L-Ala-L-Ile (AI) and L-Val-L-Val (VV) (Fig. 12) constitute a unique series of isostructural dipeptides having identical three-dimensional hydrogen bond networks. Hydrophobic side chains are segregated on the surface of the nanopores, that run parallel to the hexagonal axis of symmetry, describing right-handed helicoidal channels (P6$_1$ space group), conferring apolar nature to the pore surface. In addition,

by varying the steric hindrance of the dipeptide side chains it is possible to tailor the pore diameter (from 3.7 to 5.0 Å) and influence the pore helicity.

L-alanyl-L-valine (AV)

L-valyl-L-alanine (VA)

L-valyl-L-isoleucine (VI)

L-isoleucyl-L-valine (IV)

L-alanyl-L-isoleucine (AI)

L-isoleucyl-L-alanine (IA)

L-valyl-L-valine (VV)
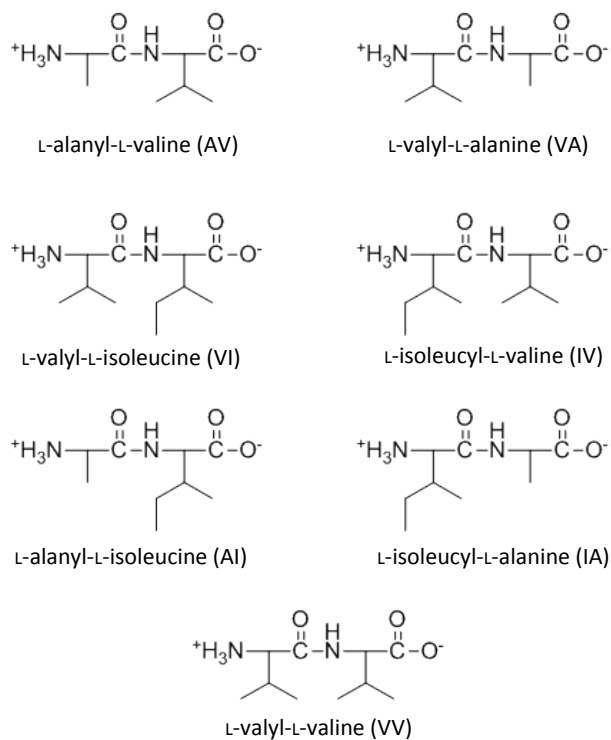
Fig. 12 – Molecular structures of the seven porogenic dipeptides belonging to the Val-Ala class
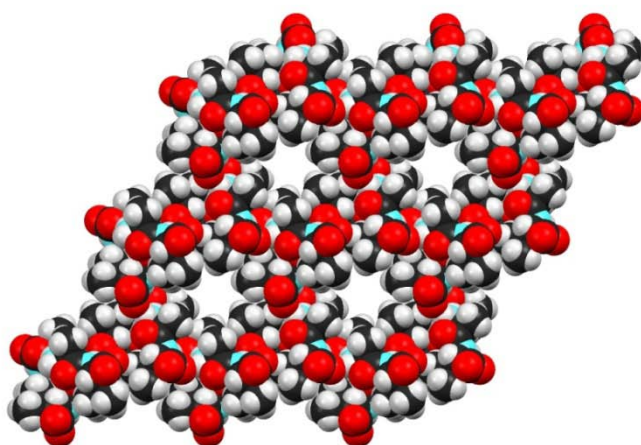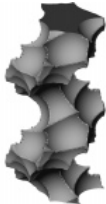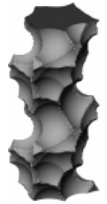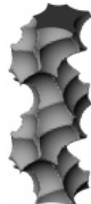
Fig. 13 – Spacefill model of the hexagonal structure of L-alanyl-L-valine (AV) dipeptide (2x2 unit cells) viewed along *c* axis. Channel surface is hydrophobic, as aliphatic side chains are exposed towards the pore.

Table 2 – Van der Waals volumes, porosity and cristallographic data of hydrophobic dipeptides

Channel shape	VA	AV	VI	IV	AI	IA	VV
Molecular formula	$C_8H_{16}N_2O_3$	$C_8H_{16}N_2O_3$	$C_{11}H_2N_2O_3$	$C_{11}H_2N_2O_3$	$C_9H_{18}N_2O_3$	$C_9H_{18}N_2O_3$	$C_{10}H_{20}N_2O_3$
Molecular weight (Da)	188.2	188.2	230.3	230.3	202.3	202.3	216.3
Crystallographic system, Space group	hexagonal, $P6_1$	hexagonal, $P6_1$	hexagonal, $P6_1$	hexagonal, $P6_1$	hexagonal, $P6_1$	hexagonal, $P6_1$	hexagonal, $P6_1$
a (Å)	14.462(2)	14.461(2)	14.774(2)	14.871(2)	14.261(2)	14.481(2)	14.573(2)
c (Å)	10.027(4)	10.083(1)	10.319(1)	10.305(1)	10.221(1)	10.037(1)	10.354(1)
Z	6	6	6	6	6	6	6
Calculated average pore diameter (Å)	4.724	5.014	3.702	3.904	4.740	3.736	4.390
Range diameter (Å)	4.63-4.77	4.98-5.05	3.66-3.75	3.85-3.93	4.66-4.78	3.70-3.76	4.26-4.48
He pycnometry average pore diameter (Å)	5.08(8)	5.36(8)	3.0(2)	3.4(1)	4.3(1)	3.6(1)	4.0(1)
He pycnometry porosity (%)	11.2(2)	12.5(2)	3.7(2)	4.8(2)	8.3(2)	5.7(2)	6.9(2)
Calculated porosity (%)	9.68	10.90	5.69	6.25	10.02	6.04	8.23
Helix radius (Å)	1.13	0.60	0.32	0.92	0.58	1.01	0.57
Helicity	high	low	low	high	low	high	low

Dipeptides of this new class of *biozeolites* permanently maintain their porous structures even after crystallization solvent removal, proving their overall stability. For instance, in the case of

L-alanyl-L-valine, the crystallization solvent molecules can be removed by thermal treatment and substituted with other suitable low molecular weight solvents, without severe structural changes during the whole process. Anyway, it was shown that introduction of bulkier guests affords irreversible changes in the structure, which is able to adapt its channel shape to the guest upon introduction, showing a dynamic behavior[46].

Nanopores are freely accessible not only to low molecular weight solvents but to gas molecules, too. He picnometry, for instance, has allowed an independent estimation of pore size and overall porosity which was found in overall agreement with geometrical evaluation based merely on the crystal structure. On the other hand, free gaseous diffusion was demonstrated using Xe atoms as nanoprobes in advanced solid-state [129]Xe NMR experiments, to explore the channel geometry and evidence how pore size affects the isotropic chemical shift of the [129]Xe *nuclei* in confined space[47]. Continuous Flow hyperpolarized [129]Xe two-dimensional exchange NMR spectroscopy also allowed the direct observation of Xe atoms entering and exiting AV nanopores[48].

Notably, Xe is able to diffuse apparently unhindered even in dipeptides whose Van der Waals channels appear to be smaller than the Xe Van der Waals diameter (4.3 Å): such discrepancy has been considered a hint of the host's flexibility and its ability in participating in cooperative dynamic motion. In fact, due to its interaction time-scale, X-ray diffraction unable to detect dynamic events taking place on longer timescales and pore sizes estimated geometrically from crystalline structure might not be able to take into account collective motions. Specific characterization techniques are thus needed.

An independent confirmation of the dynamical nature of the dipeptides architecture came from terahertz (THz) spectroscopy. In fact, terahertz vibrational modes are characterized by non-local, collective molecular motions which are relevant to conformational changes and molecular functions (transport processes) in biological systems: occurrence of these vibrational modes was recently investigated on the class of hydrophobic dipeptides considered as simplified models of membrane pores. Normal mode analysis on therahertz vibrations confirmed the existence of low frequency motions involving hydrogen bonds and inducing rearrangement of the aliphatic side chains which constitute the nanotubes. In almost all dipeptides investigated channel *breathing* modes, where side chains synchronously vibrate towards the channel center (e.g. 6_1 axis), where evidenced: such motions increase the pore

diameter, facilitating transport of gas and solvent molecules through the pores and explaining why Xe atoms could enter pores only apparently smaller[49].

The flexible nature of the dipeptide nanopores was shown by studying AV crystal structure under hydrostatic pressure: under the applied load, the structure undergoes remarkable unit cell volume reduction (compared to other non-porous dipeptides) and partial closure of the pores *via* corkscrew motion, without phase change[50].
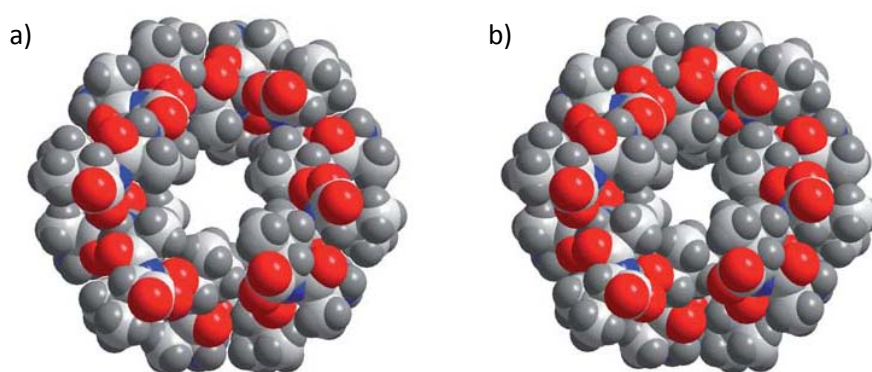
Fig. 14 - Space-filling plots of L-alanyl-L-valine (AV) at (a) ambient pressure and (b) 0.2 GPa as viewed along the c-axis. Note the closure of the central void on increasing pressure (adapted from Ref. 50)

For their unique structure, dipeptide biozeolites were recently exploited as adsorptive materials towards gases of relevant industrial and environmental interest such as methane, carbon dioxide and hydrogen. Our group has characterized the adsorption properties of AV, VA, IV and VI evidencing how merely structural features (channel diameter and helicity) can influence and differentiate the sorption performances of the nanoporous material[51]. In fact, having tailorable pore dimension enables the choice of the most appropriated dipeptide for every single application.

Other than preferential adsorption, selective exclusion of adsorptives is possible using nanoporous dipeptides, by means of a purely steric hindrance of guests. In this regard, single crystal membranes were prepared using either L-alanyl-L-alanine (AA)[52], L-valyl-L-isoleucine (VI) and L-leucyl-L-serine (LS) from where argon, nitrogen and oxygen were sequentially excluded: while LS, having the largest pores of the series, admitted all three gases in its pores, VI, having slightly smaller pores, excluded argon while AA (having the smallest cavities) excluded both argon and nitrogen[53].

1.6. Aim of the thesis

Microporous materials have drawn great interest in the last twenty years and have been used for a number of applications such as heterogeneous catalysis, adsorption, separation, gas storage and as nanovessels. Such interest has been aimed at extending the conventional nanoporous materials offer, which consisted mainly of crystalline inorganic frameworks (e.g. zeolites and related structures) and amorphous structures (e.g. activated carbons). However, in the last decade there have been major advances in the preparation of crystalline materials with permanent nanoporosity using molecular components: metal-organic frameworks (MOFs also called porous coordination polymers, PCPs) are a remarkable example of a strategy which allows the precise tailoring of pore size, dimensionality and functionalization.[54,55,56]

Purely organic nanoporous materials, based on supramolecular interactions only, became also available comprising TPP (Tris(*o*-phenylenedioxy)cyclotriphosphazene) and analogues, cucurbit[*n*]urils (n=5, 6 and 8), cyclodextrins *et cetera*.[57,58]

In our case, nanoporous dipeptide materials combine self-assembly, peptide modularity, ease of synthesis, bioavailability and biodegradability. In a future where chemistry is progressively unbound from fossil feedstocks, these environmentally friendly materials, built on biologically available building blocks, are attractive candidate as "green" porous materials. The above mentioned reasons prompted this thesis, having the aim to propose dipeptide materials as new alternatives to conventional ones in the field of gas storage and separation and to investigate their ability to act as nanoreactors, specifically in polymerization reactions. Attention is also paid to a deeper understanding of the general chemico-physical properties with regard to the thermal stability and high temperature transformations of these novel materials.

Chapter 2 – Gas separation by dipeptides

2.1. Gas storage and separation

One of the most widely investigated applications of nanoporous materials is gas storage and separation through adsorption. Porous materials benefit from large specific surface areas and high specific pore volume that can be explored by gas molecules: physical interactions between the gas and the pore surface can loosely stabilize the adsorptive, making nanoporous materias suitable in the field of reversible gas storage and release. Affinity of a gas for a specific porous material can vary according to surface functionalization, pore size and the gas properties such as its Van der Waals volume and polarity. Moreover, by taking advantage of differential adsorption affinity, it is possible to selectively adsorb one gas from a binary mixture, attaining gas separation. It is therefore of key importance having at one's disposal nanoporous materials with monodisperse pore distribution to correlate pore structure to overall sorption performances and to finely tune material properties: crystalline porous materials have uniform pore size by definition and are excellent candidates for this purpose.

2.1.1. Carbon dioxide capture

Carbon dioxide (CO_2) is a gas normally present in the atmosphere at low concentration (parts per million). It is colorless and odorless and denser than air and is produced by aerobic respiration of living beings and by hydrocarbon combustion. Nowadays, CO_2 is considered responsible, together with other gases (chlorofluorocarbons, CFCs, and methane), of the greenhouse effect whose consequence is the so called global warming. CO_2 increase in the atmosphere has been correlated to the massive exploitation of fossil fuels (started in the 19th century with the Industrial Revolution) and the progressive reduction of rainforests with consequent overall perturbation of the carbon cycle on a planetary scale. Moreover, the appearance of fast developing countries whose energetic needs are growing at high pace and the lack of economically viable alternatives to fossil fuels prompted the international community to adopt conservative strategies in order to set limits to the allowed CO_2 emissions (*e.g.* the Kyoto Protocol) which governments enforce using systems of incentives and sanctions. These measures are meant to accelerate the transition to renewable energy sources and, thanks to the impact in the media, to raise the consumers' awareness towards environmental problems, inducing the modification of lifestyles and the build-up of a social control which is expressed by responsible consumer choices. In this regard, post-combustion CO_2 removal from flue gases in power plants and factories is one of the possible alternatives to postpone the transition to the, at the moment, more expensive renewable sources, reducing emission of CO_2 in a centralized way, directly where CO_2 is produced. Since flue gas has a CO_2 content of about 15% and is released at ambient pressure, high capture performances are required to sequestrate carbon dioxide efficiently. Many techniques have been investigated so far, comprising amine-based systems and emerging technologies like carbonate-based systems, aqueous ammonia, selective membranes, ionic liquids, enzyme-based systems and microporous materials (especially metal-organic frameworks) [59].
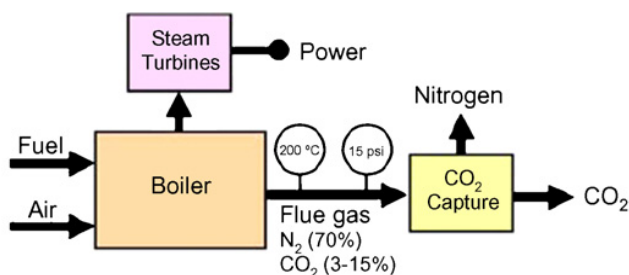
Fig. 15 – Block diagram illustrating post-combustion systems (adapted from Ref. 59)

2.1.2. Methane enhancement

Of particular industrial relevance is the problem of methane purification from carbon dioxide which is connected to at least two crucial industrial issues such as methane enrichment in biogas and carbon dioxide removal from natural gas; in fact, CO_2, beside decreasing the energy content of the gas, can have a detrimental effect on pipelines, causing corrosion and requiring additional maintenance and therefore higher operative costs. Many countries established standard rules for the concentration of contaminants for transportation of methane through pipelines, so meeting such specifications is desirable for increasing methane market and commercial value.

Among the techniques employed in methane *upgrading* it is possible to enlist three main technologies: chemical absorption, physical absorption and cryogenic distillation. Chemical absorption consists in streaming natural gas through monoethanolamine (MEA), or a combination of amines, to remove acidic CO_2 which is then released during the regeneration step of the solvent at about 400K; physical absorption employs solvents other than MEA which still allow CO_2 capture but have the advantage of lower regeneration temperatures; finally, cryogenic distillation where CO_2 is liquefied at low temperature. These three alternatives have the drawback of consuming large amounts of energy during solvent regeneration or during liquefaction, therefore new strategies have been suggested to decrease the separation costs[60].

In fact, adsorption-based technologies can reduce the energy needed for the regeneration of the separation agent (the adsorbent) and have become a valid alternative to traditional techniques. Pressure swing adsorption (PSA) in particular is a process that employs a solid adsorbent which selectively adsorbs CO_2 by different equilibrium capacities or by differences in uptake rates. In PSA, the gas is pressurized in a chamber containing the adsorbent material which sequestrates CO_2, leaving methane-enriched superincumbent gas-phase which is collected; sorbent material is regenerated by simply lowering the pressure in the vessel. Of course, it is of primary importance having at one's disposal an adsorbent with high selectivity[61]. In this regard, many materials have been suggested and studied so far, in order to identify the structural properties which promote differential sequestration: inorganic zeolites, silicalite, activated carbons and Metal-Organic Frameworks are the most common, especially for the structural variability they allow by synthesis that enable systematic investigations. On the other hand, completely organic zeolites, have been neglected mainly because of their

uniqueness which made them unsuited for comprehensive study. Nanoporous dipeptides fill this lack, offering a series of tailorable nanopores with varied geometry which can allow for a structure-properties assessment.

2.2. Dipeptides as selective sorbents

2.2.1. CH$_4$ and CO$_2$ adsorption isotherms of dipeptides

Methane and carbon dioxide adsorption isotherms have been previously measured by our group for IV and AV dipeptides up to 1 atm, at low temperature (195 K) and room temperature[62]. Adsorption isotherm profiles reveal the microporous nature of the materials (Langmuir or "type I" isotherm, see Appendix A) with gradual increase of pore loading at increasing equilibrium pressure, without hysteresis or discrete adsorption steps. CO$_2$ was always adsorbed more than CH$_4$ in single gas adsorption at both room and low temperature, indicating higher affinity of carbon dioxide towards the aliphatic pore surface of the microporous peptides, due maybe to the polarization of the C-O bond. While AV attains higher capacity at final pressure with respect to IV for both gases, IV has higher adsorption energies at low coverage (estimated through Clausius-Clapeyron equation): 23 kJ/mol versus 13 kJ/mol in case of CO$_2$ and 19 kJ/mol versus 9 kJ/mol in case of CH$_4$. Therefore, higher stabilization is obtained thanks to smaller pore size. If we define *selectivity* as the ratio between CO$_2$ loading and that of CH$_4$ at a given equilibrium pressure, it is possible to state that at low temperatures, selectivity in the AV and IV systems are comparable, reaching 5 below 100 torr and progressively decreasing with increasing pressure. Higher selectivity al lower pressures indicates high affinity for CO$_2$ towards the aliphatic pores and faster saturation of the sorbent, while in the case of CH$_4$ saturation occurs more slowly and the curves approach to each other as pressure is increased. However, at room temperature selectivity has a value between 1 and 2 for AV, while for IV it attains a value between 4 and 5, suggesting that dipeptide materials (IV in particular) could be used for practical methane purification, with selectivity comparable to recently proposed porous materials[63].
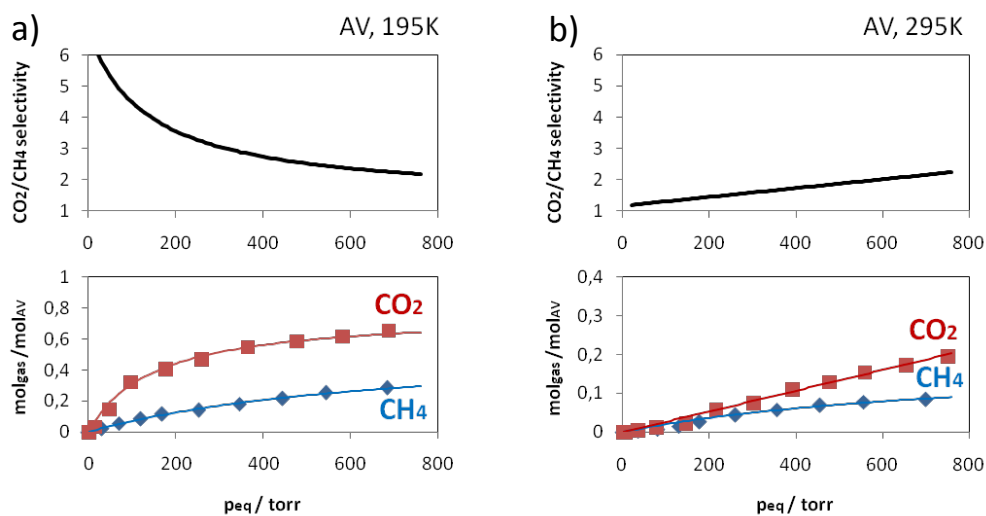
Fig. 16 – CO_2 and CH_4 adsorption isotherms and CO_2/CH_4 selectivity on L-alanyl-L-valine. a) T = 195 K b) T = 295 K
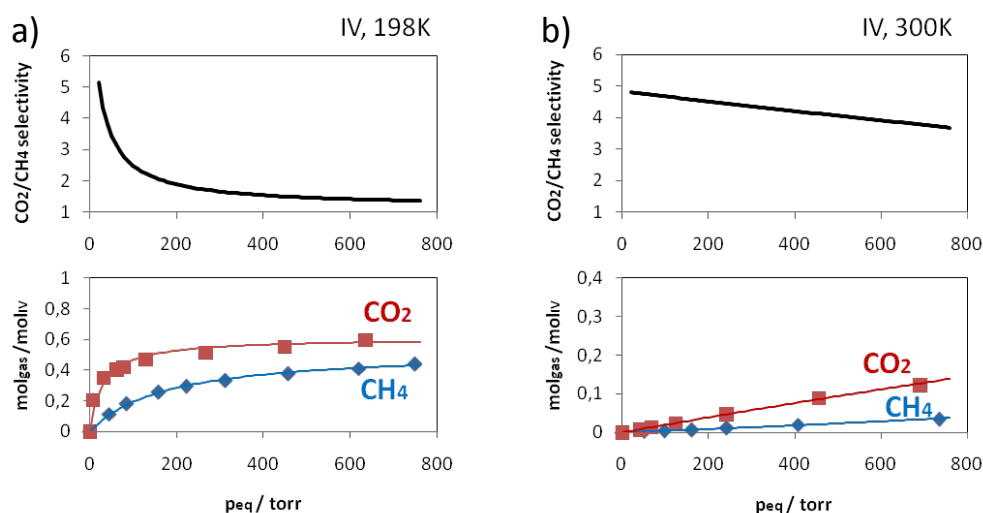
Fig. 17 – CO_2 and CH_4 adsorption isotherms and CO_2/CH_4 selectivity on L-isoleucyl-L-valine. a) T = 198 K b) T = 300 K

2.2.2. Validation by column breakthrough experiments

Sorption selectivity by dipeptides is suggested by the single gas isotherms on methane and carbon dioxide but only mixed gas adsorption experiments can operationally demonstrate this hypothesis. Thus, gas discrimination experiments where performed using a "breakthrough" system developed in-house for the purpose.

2.2.2.1.   Description of the breakthrough apparatus and experimental method

The breakthrough apparatus (Fig. 17) consists in:

- three gas lines for CO_2, CH_4 and He whose gas pressure and mass flow can be controlled by pressure reducers and electronic mass flow controllers (Fig. 17, a);
- a mixing chamber (about 5 l) equipped with vacuum gauge, where the gases are dosed until desired composition and pressure (Fig. 17, b);
- a rotary vane vacuum pump connected to the mixing chamber (Fig. 17, c);
- a glass column (10 cm height, 1 cm diameter) to be packed with sorbent, connected to the mixing chamber (inlet) and the gas cromatograph (outlet). The column can be by-passed (Fig. 17, d)
- a PC-operated gas chromatograph (Fig. 17, e).

In a typical experiment, 1.5 g of activated dipeptide (evacuated at 60 °C and 10^{-3} torr overnight) is packed in the glass column which is then connected to the system. Mixing chamber, gas lines and glass column are thoroughly evacuated (10^{-3} torr). In a first series of experiments, the activated microporous material was purged with helium and kept under a helium atmosphere (1.3-2 atm) before being invested by the CO_2/CH_4 gas mixture. Then, a second series of experiments were carried out without He gas, i.e. microporous material was kept *in vacuo* before adsorption. In both cases, the column containing the dipeptide bed is isolated and CO_2 and CH_4 are allowed to enter the mixing chamber up to the desired composition (e.g. 1:1 equimolar composition at 2 atm) which is continuously monitored by the gas chromatograph. Then the gas is deviated through the column containing the peptide sorbent and the superincumbent gas phase is analyzed along with time to assess changes in composition with respect to gas feed. Gas chromatograph analysis method was optimized to decrease the sampling frequency to about 90 seconds between consecutive injections.
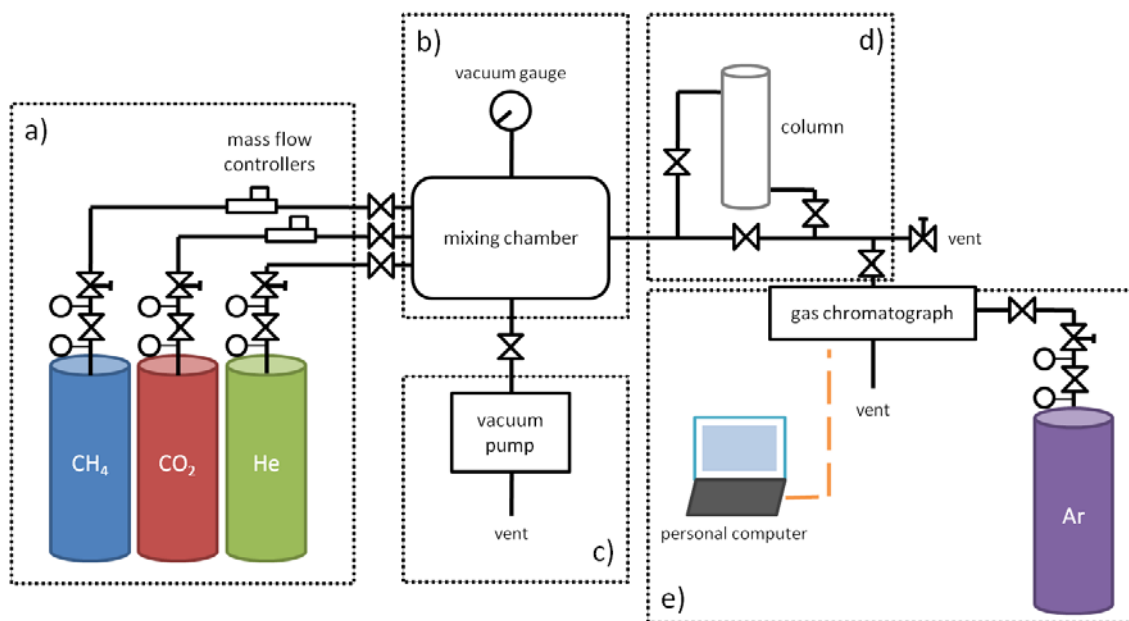
Fig. 18 – Scheme of "breakthrough" apparatus. a) methane, cabon dioxide and helium gas lines provided with pressure reducers and mass flow controllers, b) mixing chamber, c) vacuum pump, d) glass column holding microporous sorbent and e) gas analyzer (gas chromatograph, PC, Ar carrier line)
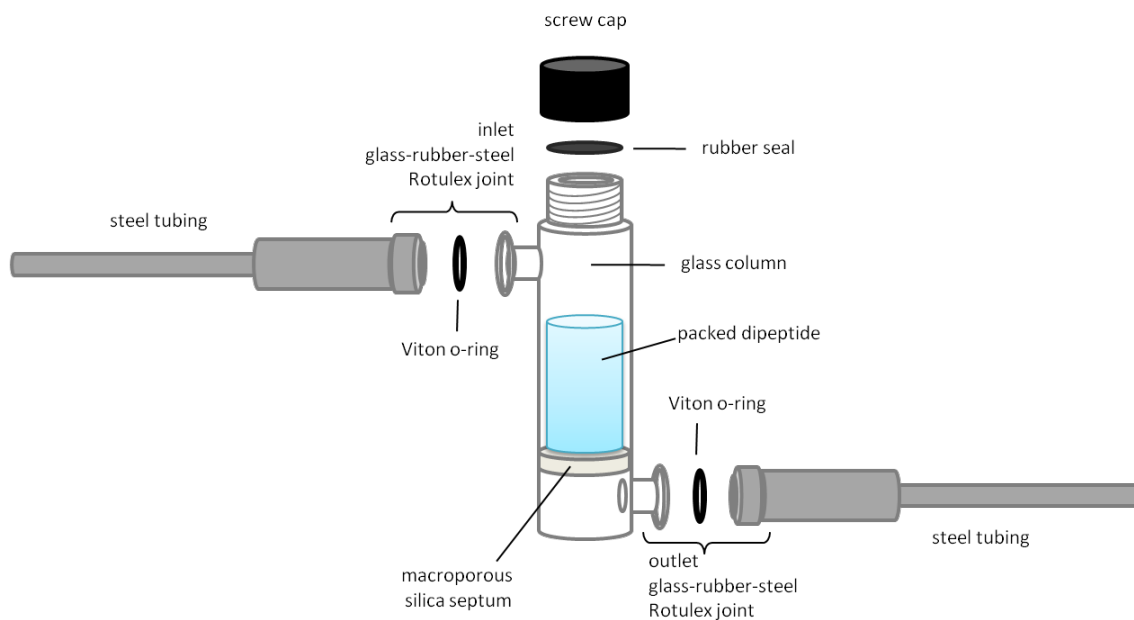
Fig. 19 – Detail of glass column holding packed microporous sorbent

2.2.2.2.   Ideal system behavior

To characterize the behavior of the separation system without the sorbent material, blank experiments were carried out. First, CO_2 and CH_4 are precisely dosed in the system so that an equimolar composition is obtained (Fig. 19, superposed red and blue symbols, negative times). As the binary gas stream is deviated in the experimental cartridge (time = 0 min), the mixture is diluted by helium whose "pulse" is evidenced in the first ten minutes from the start of the experiment (Fig. 19, green triangles). After twenty minutes, the starting gas composition is recovered (CH_4 and CO_2 only), as helium is completely carried away from the system by incoming gas feed.
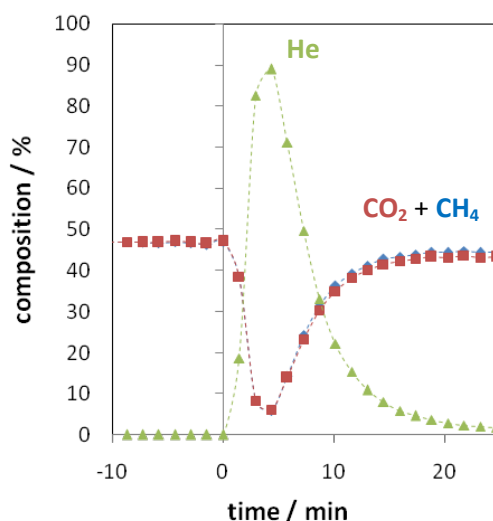
Fig. 20 – "Breakthrough" blank run with helium. He (green triangles), methane (blue diamonds) and carbon dioxide (red squares) percentage composition is plotted against time. At time = 0 min the binary mixture is deviated through the He filled cartridge.
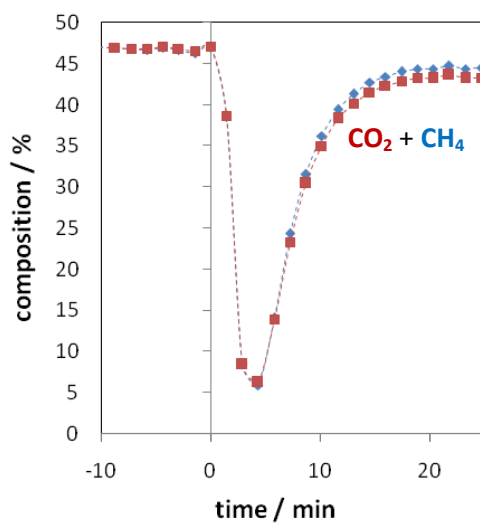
Fig. 21 – "Breakthrough" blank run with helium (enlarged plot)
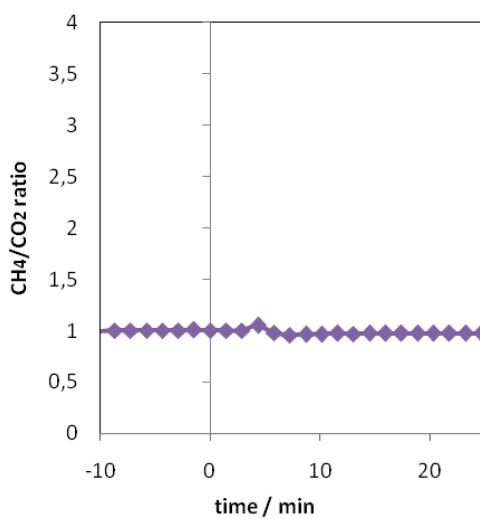
Fig. 22 – "Breakthrough" blank run with helium. Methane/carbon dioxide molar ratio is unchanged.

As expected, since no sorbent is present in the system, the relative amount of methane and carbon dioxide are left unchanged throughout the entire experiment (Fig. 21). A blank run was recorded without helium (Fig. 22 and Fig. 23), confirming the absence of air leaks and the ideal behavior of the separation apparatus.
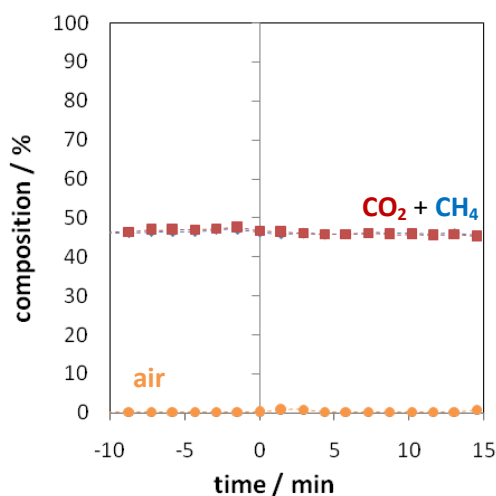
Fig. 23 – "Breakthrough" blank run without helium. Methane (blue diamonds) and carbon dioxide (red squares) percentage composition is plotted against time. At time = 0 min the binary mixture is deviated through the cartridge held under vacuum. Orange circles represent air (always under 1%).
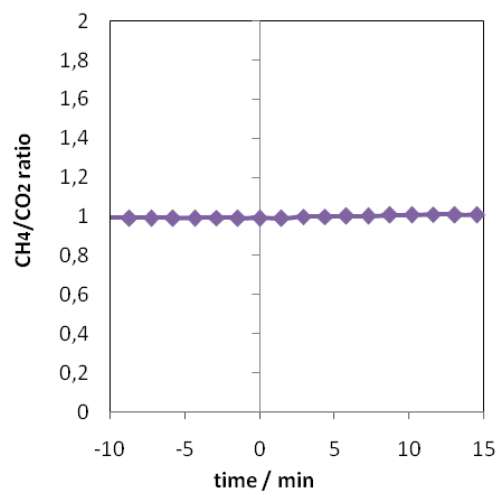
Fig. 24 - "Breakthrough" blank run without helium. Methane/carbon dioxide molar ratio is unchanged.

2.2.2.3.   Methane enrichment using L-isoleucyl-L-valine (IV)

When 2 grams of L-isoleucyl-L-valine are packed in the separation cartridge in presence of helium and the experiment is performed, the plot in Fig. 24 is obtained. As the binary mixture is passed through the dipeptide bed, dilution with helium occurs but a compositional unbalance in the methane/carbon dioxide ratio is evidenced. In fact, the amount of CH_4 (blue

diamonds) in the gas flowing out the sorbent bed is higher than the amount of CO_2 (red squares). As the dipeptide saturates, and adsorbed species are in equilibrium with gas feed, the starting gas composition is recovered again (t > 30 min).

Fig. 25 – "Breakthrough" curve of methane (blue diamonds) /carbon dioxide (red squares) binary mixture passing through an L-isoleucyl-L-valine bed. At time = 0 min the binary mixture is deviated through the cartridge containing the dipeptide under helium atmosphere (green triangles)

Fig. 26 - "Breakthrough" curve of methane (blue diamonds) /carbon dioxide (red squares) binary mixture passing through an L-isoleucyl-L-valine bed. (enlarged plot)

Plotting gas composition (normalized on methane and carbon dioxide only) versus time (Fig. 26), shows that CO_2 is sequestrated by the dipeptide so that the amount of CH_4 left in the stream overcomes the one of CO_2 causing a composition change from starting 50:50 CH_4:CO_2 ratio to a final 70:30 CH_4:CO_2 ratio (2.3 CH_4/CO_2 ratio).

Helium isn't physisorbed on microporous solids at room temperature and thus doesn't interfere with CH_4 and CO_2 adsorption; anyway its presence slows down the adsorption phenomenon due to dilution of incoming gas mixture whose partial pressure will be lower than pure gas, making interaction with the microporous material more gradual and slowing down the saturation transient.
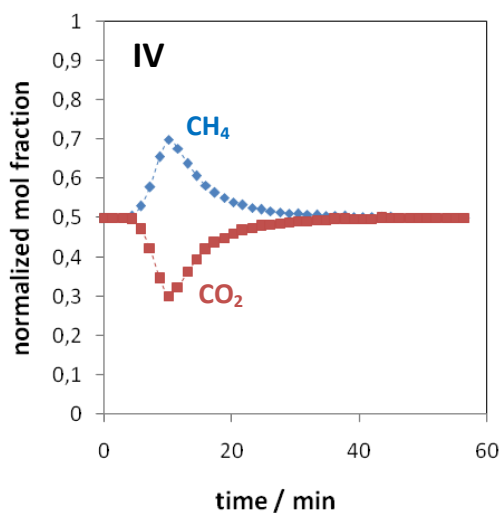
Fig. 27 – "Breakthrough" experiment using L-isoleucyl-L-valine as sorbent material. Gas composition (CH_4, blue diamonds, CO_2, red squares) is represented over time, evidencing methane enrichment with respect to carbon dioxide due to selective CO_2 sequestration.
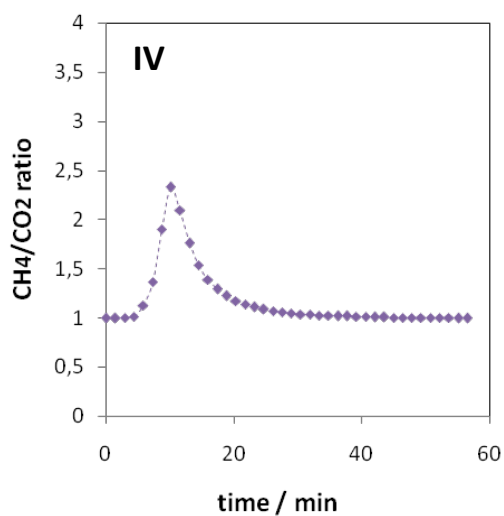
Fig. 28 - "Breakthrough" experiment using L-isoleucyl-L-valine as sorbent material. CH_4/CO_2 ratio is represented over time. The gas flowing out the sorbent is enriched in methane, up to 2.3 times with respect to carbon dioxide.

Anyway, selective sorption can be realized without helium as "protective" gas: in this case, the maximum methane/carbon dioxide ratio corresponds to about 1.7 (Fig. 29).
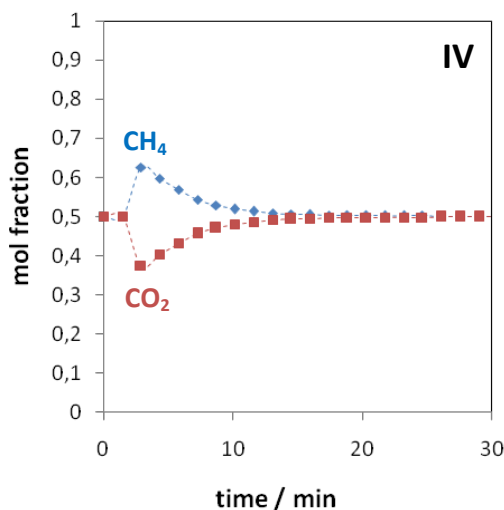
Fig. 29 – "Breakthrough" experiment using L-isoleucyl-L-valine as sorbent material. Gas composition (CH_4, blue diamonds, CO_2, red squares) is represented over time, evidencing methane enrichment. In this case helium was not used as "diluting" gas.
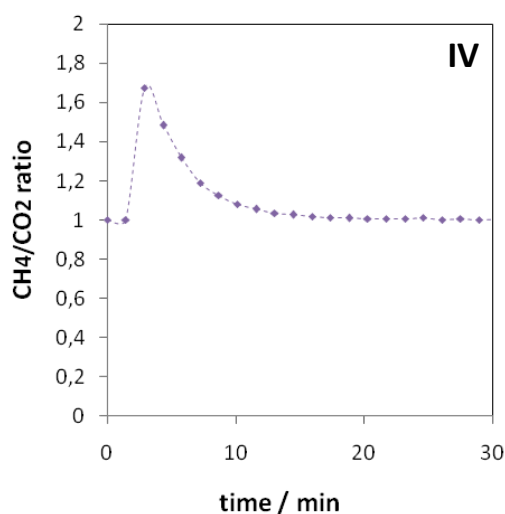
Fig. 30- "Breakthrough" experiment using L-isoleucyl-L-valine as sorbent material. Methane/carbon dioxide ratio is represented over time, evidencing methane enrichment.

2.2.2.4. Release of carbon dioxide-rich gas from IV

Reversible capture of carbon dioxide is a desired feature for energy saving gas purification applications, since irreversible capture of CO_2 would poison the sorbent, making and additional recovery step necessary and energy consuming (e.g. heating of amine solution to release CO_2, in amine scrubbing process). Therefore, the release of CO_2 in mild conditions was investigated. Indeed, the selective sorption of carbon dioxide over methane can be also evidenced in desorption: after performing the "breakthrough" experiment, the cartridge containing the saturated microporous crystals is purged with a stream of pure helium; carbon dioxide and methane contained in the micropores are released in the helium feed which acts as a carrier. Fig. 30 shows the outcome of a representative desorption experiment on IV: in this case, the content of carbon dioxide (red squares) is higher than methane (blue diamonds), in agreement with preferential CO_2 sequestration during the previous adsorption step.
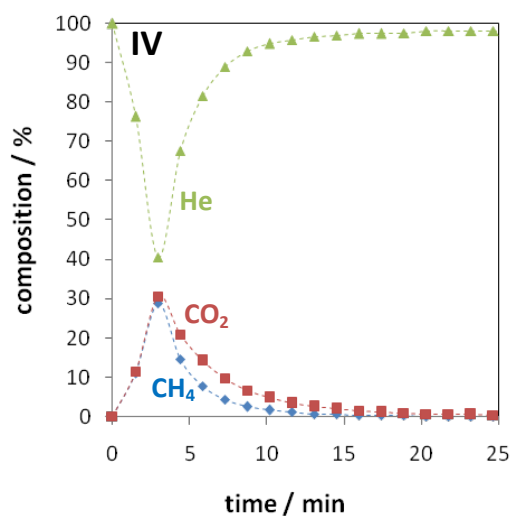
Fig. 31 – He (green triangles), methane (blue diamonds) and carbon dioxide (red squares) amounts in desorption experiments with L-isoleucyl-L-valine.
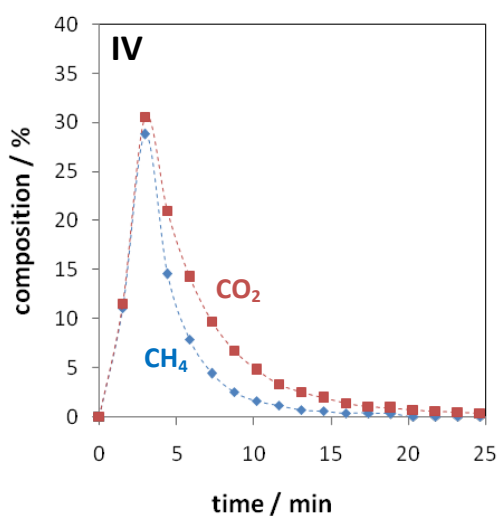
Fig. 32 - Methane (blue diamonds) and carbon dioxide (red squares) amounts in desorption experiments with L-isoleucyl-L-valine (enlarged plot).

The whole adorption/desorption process is sketched in Fig. 32: at the beginning of the experiment the nanoporous material is either held in a "inert" gas atmosphere or in vacuum and its pores are not interested by physisorption and ready to interact with carbon dioxide and methane molecules (Fig. 32, a); then the material is invested by the gas mixture flow and carbon dioxide is selectively physisorbed on the nanopore surface while methane, interacting

less with the sorbent material, is preferentially left in the gas phase (Fig. 32, c); finally, as a helium stream is passed through the dipeptide bed, an excess of carbon dioxide is evidenced (Fig. 32, g), in agreement with its selective interaction with the dipeptide.

Reversibility was maintained along all the experiments performed, and dipeptides tolerated more than fifty cycles of gas exposure followed either by helium purge or vacuum treatment without appreciably losing their sorption capabilities.
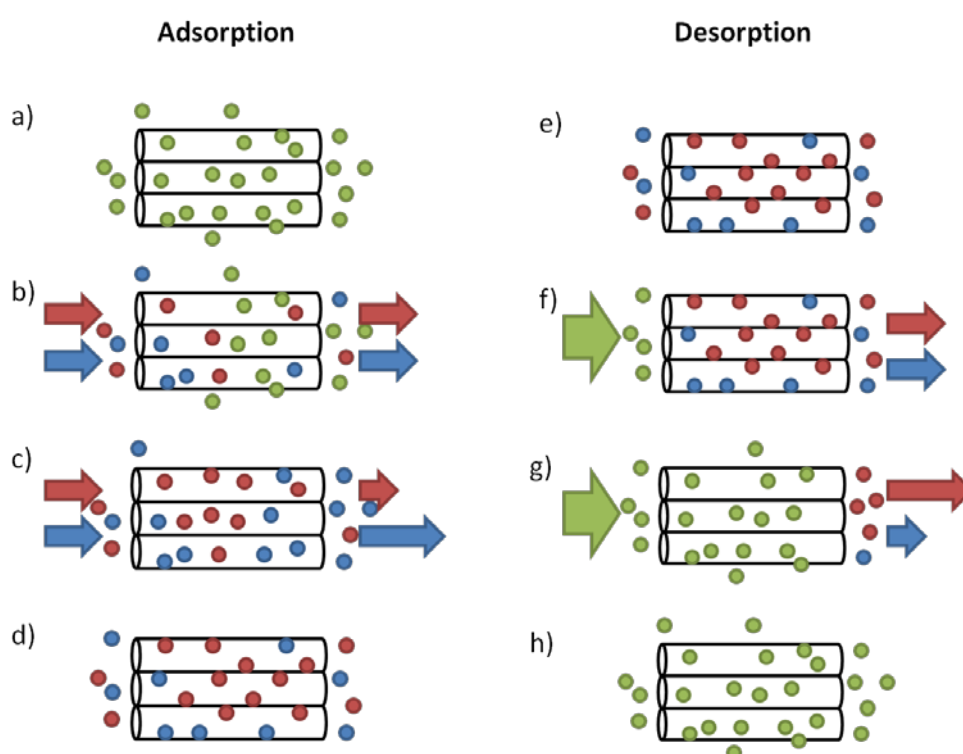
Fig. 33 – Adsorption step: a) dipeptide is held in a He atmosphere, b) equimolar CO_2/CH_4 stream is passed through the dipeptide bed and dilution with helium occurs, c) preferential sorption occurs and outlet gas is enriched in methane, d) at equilibrium with gas feed, CO_2 is selectively bound to nanopores. Desorption step: e) adsorbed phase is in equilibrium with gas feed, f) dipeptide is purged with helium, g) CO_2 enriched gas is desorbed from the dipeptide, h) dipeptide is completely purged.

2.2.2.5.   Comparisons with L-alanyl-L-valine (AV) and L-isoleucyl-L-valine (IV)

Breakthrough experiments were performed on L-alanyl-L-valine (AV), too. Considering AV adsorption isotherms on single gases at room temperature, we can see how, even if AV has a higher final loading for both CH_4 and CO_2 at 1 atm with respect to IV (higher *capacity*), the final

ratio between carbon dioxide and methane equals 2.3, while IV, notwithstanding an overall lower capacity, shows a final ratio of 3.7. From the above considerations, and the value of the isosteric heat of adsorption, we expect that selectivity in AV would be lower accordingly, with respect to IV performance. Indeed, the expectation is fulfilled.
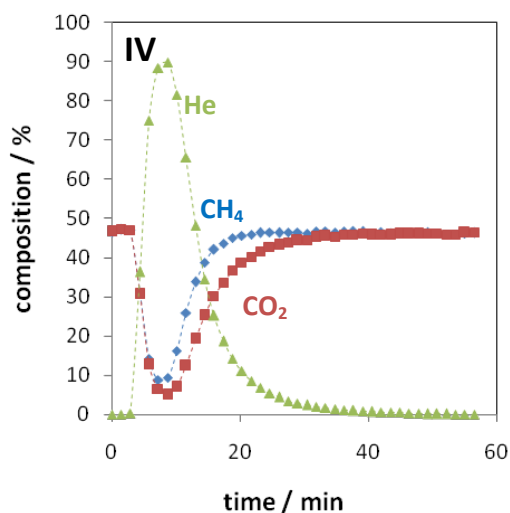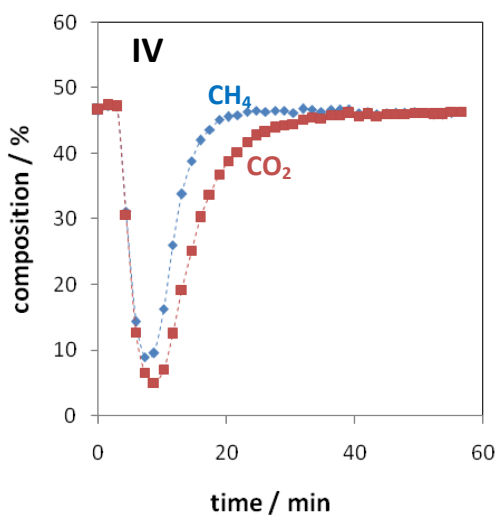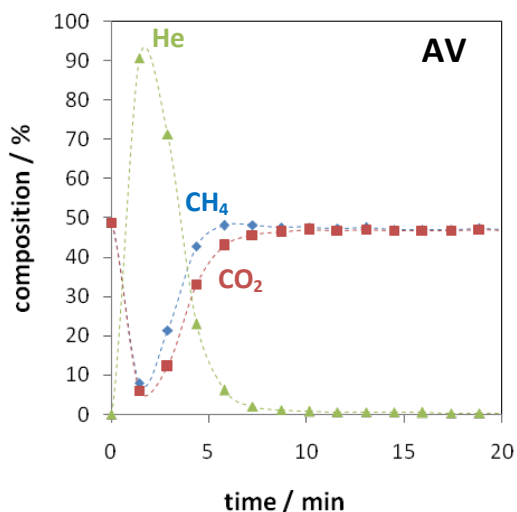

Fig. 34 - "Breakthrough" curve of methane (blue diamonds) /carbon dioxide (red squares) binary mixture passing through an L-alanyl-L-valine bed. Green triangles indicate helium.
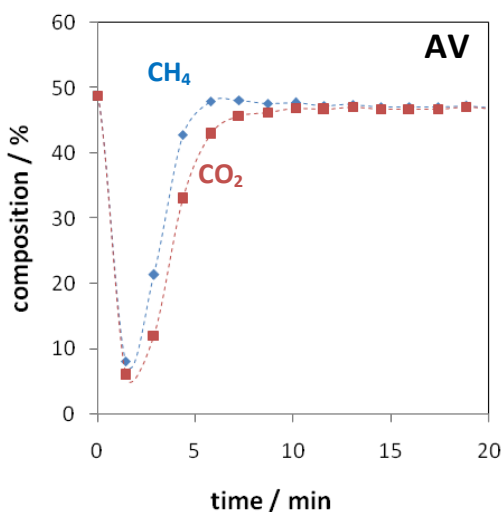
Fig. 35 - "Breakthrough" curve of methane (blue diamonds) /carbon dioxide (red squares) binary mixture passing through an L-alanyl-L-valine bed (enlarged plot)

As Fig. 34 shows, the methane trace is still higher than the one of carbon dioxide, indicating methane enrichment, but the difference between the two curves is lower compared to IV (Fig. 25). Plotting CH_4/CO_2 ratios versus time (Fig. 35) allows for a immediate comparison between AV and IV performances, with AV maximum enrichment attaining the value of 1.8.
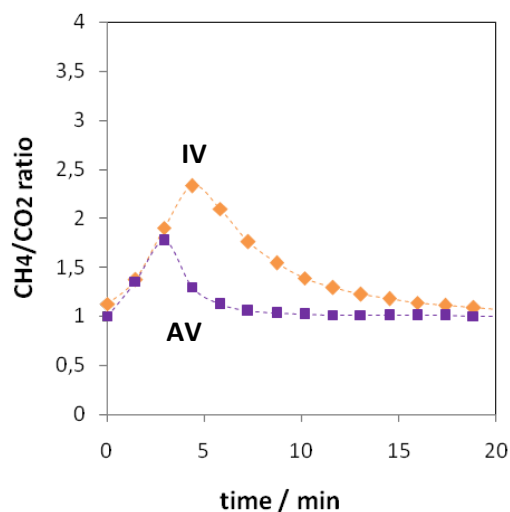
Fig. 36 – Comparison between IV (orange diamonds) and AV (purple squares) performance in methane enrichment.

AV and IV nanochannels differ in pore sizes, while chemical nature of the pore walls (hydrophobic) and geometry of the pore (e.g. helicity and pitch) are comparable: AV pore diameter ranges from 5.0 to 5.4 Å, while IV has sensitively smaller diameter (namely from 3.0 to 3.7 Å). While higher pore diameter (and therefore volume) is correlated to higher loading capacity, higher selectivity is correlated to smaller pore diameter, as suggested from adsorption isotherms and breakthrough experiments reported above. This empirical dependence prompted us to improve methane enrichment using the porous dipeptide with smallest pore diameter available: L-valyl-L-isoleucine.
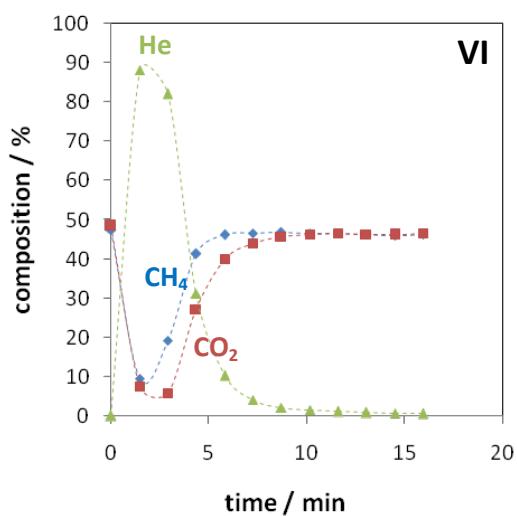
Fig. 37 - "Breakthrough" curve of methane (blue diamonds) /carbon dioxide (red squares) binary mixture passing through an L-valyl-L-isoleucine bed. At time = 0 min the binary mixture is deviated through the cartridge containing the dipeptide under helium atmosphere (green triangles)
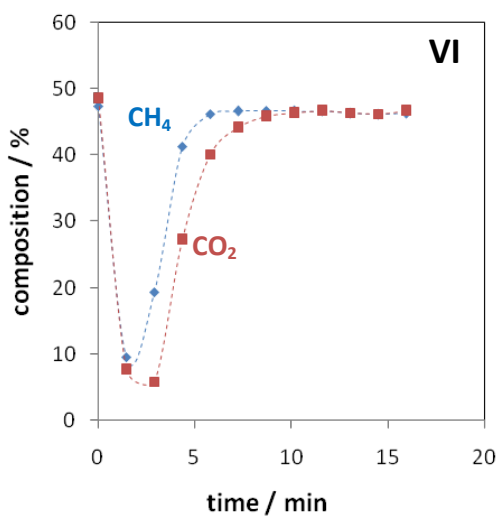
Fig. 38 - "Breakthrough" curve of methane (blue diamonds) /carbon dioxide (red squares) binary mixture passing through an L-valyl-L-isoleucine bed (enlarged plot)

In Fig. 38, VI performance is compared to IV and AV. As expected, methane enrichment using VI reaches the highest values, up to 3.3 CH_4/CO_2 ratio. It is noteworthy that, at present, VI adsorption isotherms for methane and carbon dioxide are unknown: breakthrough

experiments can be thus used as a faster screening technique with respect to adsorption isotherms, to foresee single gas behavior.
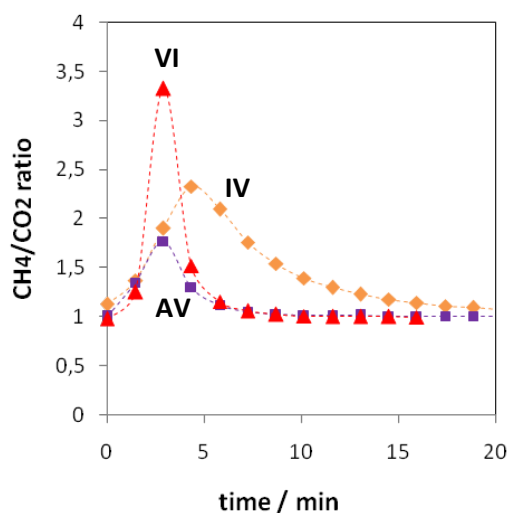
Fig. 39 – Comparison between VI (red triangles), IV (orange diamonds) and AV (purple squares) performance in methane enrichment.

2.2.2.6. Variable composition experiments on VI

Complete CO_2 removal from the binary gas mixture was never obtained since the amount of dipeptide used was low compared to the gas coming in contact with it, causing the rather prompt saturation of the sorbent. From an operational point of view, having longer adsorption beds would afford a higher number of theoretical plates where multiple gas phase / adsorbed phase equilibria would be established. This situation is equivalent to repeating the breakthrough experiment on an array of packed columns placed in series, where the incoming gas mixture is progressively enriched in methane. Single experiments were then performed on the best performing dipeptide (VI) with varying gas composition, ranging from 0 to 100% CO_2 content. To be closer to the operative situation, He was avoided as "diluting" gas.

Results are plotted in Fig. 39 where final CO_2 fraction (at highest methane enrichment) is plotted against starting gas composition (circles). For all compositions examined, selective CO_2 segregation takes place, as all experimental points stay below the unitary slope line, which corresponds to a lack selectivity (e.g. the starting and final compositions are the same for every methane/carbon dioxide ratio).
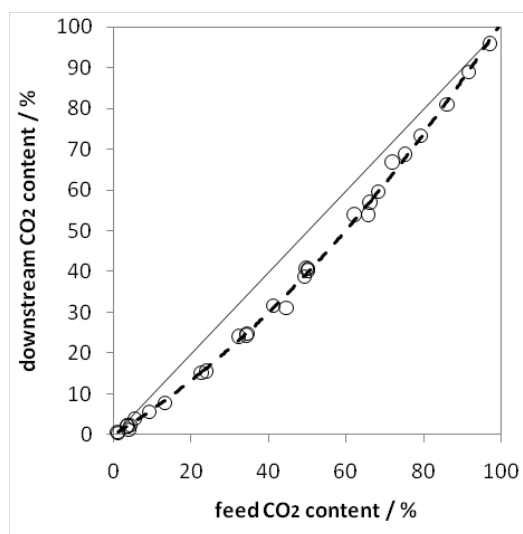
Fig. 40 – VI breakthrough experiments at variable composition. CO$_2$ content in methane-enriched gas is plotted vs. starting CO$_2$ amount in feed stream (circles). Black line represents the *locum* of unaltered composition, namely no selectivity.

The plot in Fig. 39 is reminiscent of the isotherm of adsorption of a binary mixture at a fixed pressure where the equilibrium composition of adsorbed phase is plotted against gas phase composition: in fact, instead of measuring adsorbed phase composition, its complement is measured, namely gas composition before sorbent saturation. It is evident that our measurement isn't an accurate thermodynamic characterization since the experiments are performed dynamically and are influenced by several factors such as system geometry, sorbent amount, gas flow speed, gas interdiffusion, frequency of sampling; anyway, it represents a *proof-of-concept* demonstration that dipeptides are capable of selectively and reversibly bind CO$_2$ at exceptionally mild conditions.

2.3. Conclusions

In conclusion, a new method for characterizing the competitive adsorption of two gases on a microporous material was developed in-house. The method, yet in its early implementations, allows the qualitative estimation of different performances attained by microporous materials and to demonstrate that gas separation can be obtained exploiting the higher affinity of one gas over the other. Our experiments show preferential retention of CO$_2$ over CH$_4$ both during adsorption (excess methane in the downstream mixture) and desorption (excess carbon dioxide during He purge). A qualitative relationship between pore size and separation

performance was evidenced with CH_4/CO_2 selectivity increasing with decreasing pore size (selectivity: VI (3.3)>IV (2.3)>AV (1.8), pore size: AV>IV>VI), which confirm the results of room temperature single gas adsorption.

Chapter 3 – Microstructural Control in Channel Nanovessels

3.1. Polymerizations in confined spaces

Cavities offered by nanoporous materials allow for confined-space polymerizations. In fact, confined reagents (by means of inclusion or adsorption) and products formed thereof experience an exotic environment compared to ordinary reaction conditions (bulk or in solution) since must fulfill severe steric requirements which have influence on reagent pre-organization, selection – or prohibition – of transition states and respect of a geometrical match between the product and the cavity.

In this regard, radical polyadditions are particularly suited reactions to study confined chemistry, since they feature several advantages: the presence of one reactive species (the free radical) which propagates in the cavity, the lack of by-products, the obtaining of a macromolecular product that allows, by means of nuclear magnetic resonance (NMR) techniques, to characterize the reactive history by examining the polymer microstructure, regioregularity and stereoregularity. Moreover, because of their general non-specificity, radical polyadditions can provide a reliable demonstration of reaction control caused by confinement. To avoid chemical free radical initiators, polymerization is initiated by means of a

physical stimulus (β, γ or X-rays) which promote homolytic bond breaking in monomers and free radical generation. Reaction environment is completely unusual: there is no solvent, no organo-metallic catalysts and polymer chains are isolated (one chain per channel), reducing radical transfer and recombination.

Systems where channels polymerizations were first proposed are inclusion compounds (ICs) between an organic *host* and monomer *guests*. In some clathrates it is possible to polymerize guest molecules attaining a solid-state transformation from inclusion compound to nanocomposite. Such kind of polymerizations were performed successfully in the past using, among others, urea, thiourea, perhydrotriphenylene (PHTP), cholic acids (DCA and ACA) and tris(o-phenylenedioxy)cyclotriphosphazene (TPP), and with a variety of monomers[64].

However, since clathrates can be formed only in the presence of a suitable guest, extending the investigation to monomers which do not form inclusion compounds with a given host is precluded. The majority of hosts collapse to a non-porous phase as the guest is removed by evacuation or thermal treatment: this prevents the *a posteriori* introduction of different guests. On the other hand, clathrates have pore geometry which cannot be tailored easily by design, since change in the host molecular structure generally leads to the loss of clathrating capabilities.

To overcome the above-mentioned drawbacks, materials with permanent porosity were investigated as nanovessels. In fact, beside inclusion compounds, channel polymerizations can be obtained in other systems such as mesoporous (e.g. mesoporous silicas) or microporous materials, like inorganic zeolites [65,87] and porous coordination polymers (PCPs)[66]. Such materials have the advantage of retaining porosity even in absence of a guest and offer a wider offer of structures, pore geometry and dimensionality.

In our case, four aliphatic dipeptides with different pore size and helicity were used in combination with three different monomers to study the effect of channel environment upon the final product. AV and IV together with their retro-analogs VA and VI were used to polymerize *trans*-1,3-pentadiene, isoprene and acrylonitrile.

The choice of dienic monomers (*trans*-1,3-pentadiene and isoprene) is dictated by the rich microstructural variability that they can produce in absence of a control mechanism. In fact, 1,4-*trans*, 1,4-*cis*, 1,2-*trans* and 3,4 additions are allowed with increasing complexity provided

by possible regiochemical defects (head-to-head or tail-to-tail) combined with various stereochemical configurations if a stereogenic carbon is present (such as in the case of polypentadiene). Finally, radical transfer to the chain backbone may occur with production of branched and reticulated polymers. This rich picture provides a striking comparison with nanovessel-polymerized macromolecules where only a limited series of allowed microstructures are expected to survive.
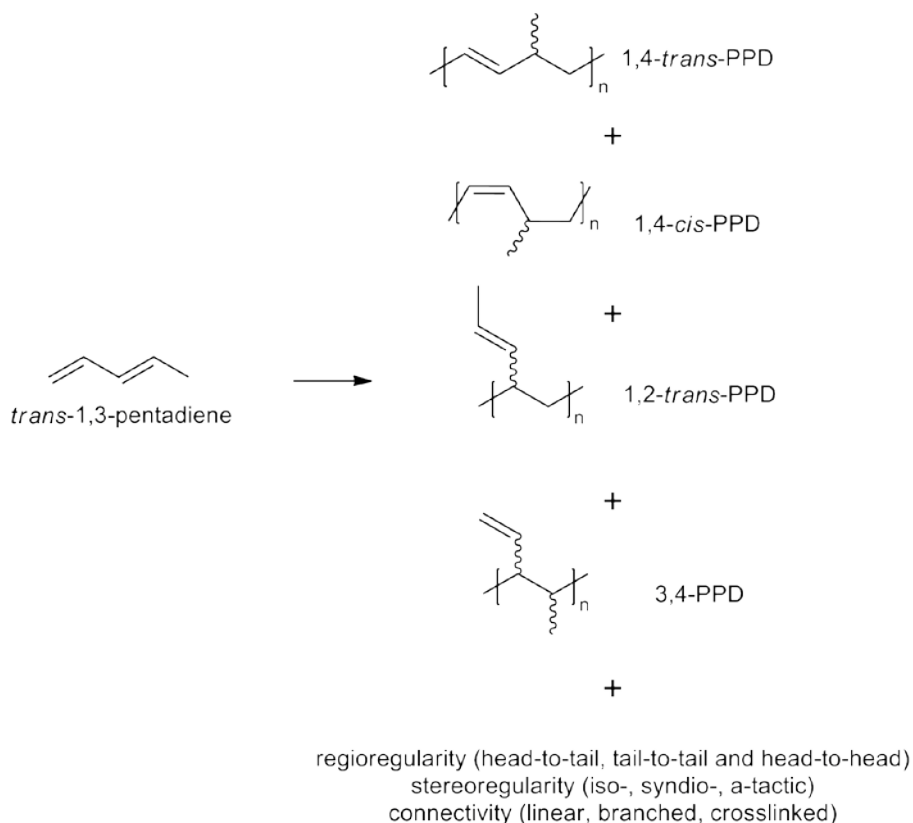
Fig. 41 – Potential microstructures arising from non-controlled radical polymerization of *trans*-1,3-pentadiene

While polypentadiene (PPD) has restricted technological application and its synthesis in the present work is merely justified to benchmark the channel polymerization hypotesis, polyisoprene (PI) has extreme importance since perfectly regular 1,4-*cis* polymer (natural rubber) or the 1,4-*trans* isomer (gutta percha) can only be synthesized enzimatically by certain plants (*Hevea brasiliensis* and *Palaquium gutta* respectively), and improving the currently available synthetic strategies to obtain one of the possible enchainments with high structural regularity is a challenging task.
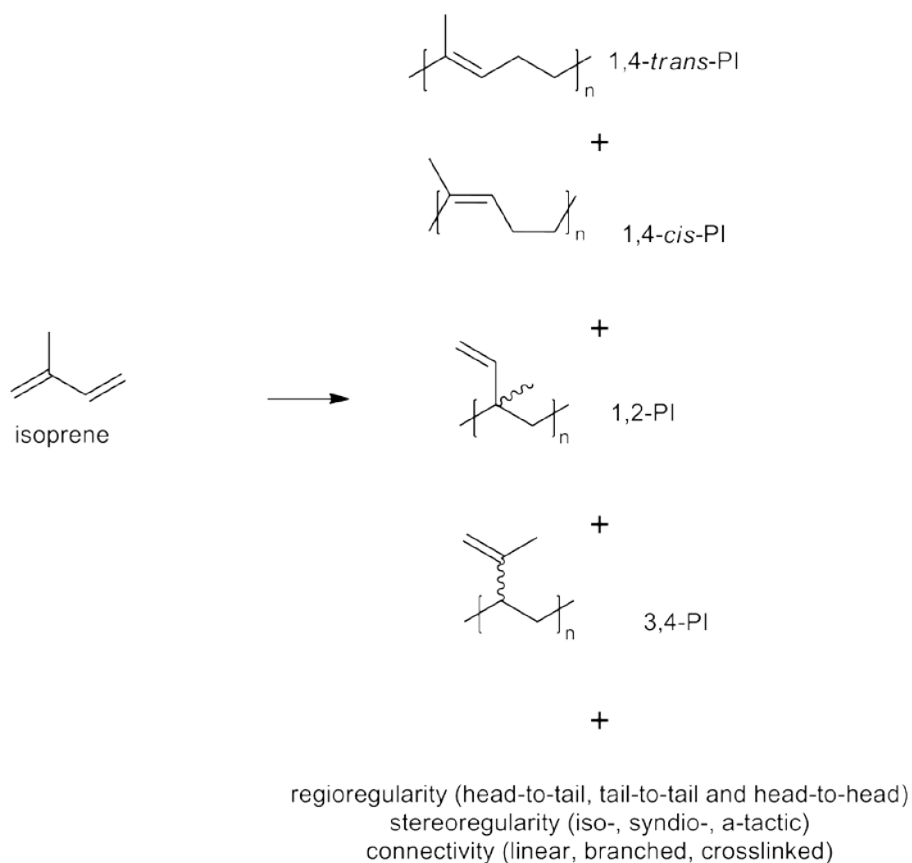
Fig. 42 – Potential microstructures arising from non-controlled radical polymerization of isoprene

Finally, polyolefin polymers such as polyacrilonitrile (PAN) have lower structural variability compared to substituted polydienes. Isotactic, syndiotactic or atactic polymers can be potentially synthesized with atactic configuration being the one attained by radical polymerization in bulk or solution and in absence of a control mechanism. However, highly isotactic PAN could only be obtained in urea/acrylonitrile IC in the past, even though under strict preparation conditions[67] and classical asymmetric catalysts for olefin polymerizations proved mostly ineffective[68].
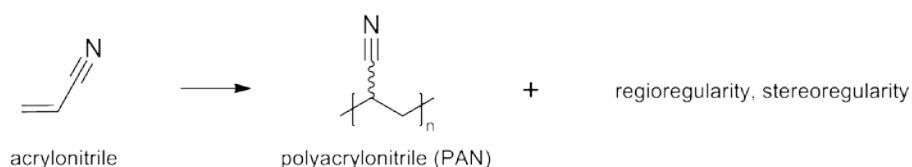
Fig. 43 – Potential structures of polyacrylonitrile

3.2. Nanocomposite preparation

Beside gas molecules (as seen in Chapter 2) also vapour molecules can be adsorbed in dipeptides. For instance, *n*-pentane is readily adsorbed on IV and AV, reaching the virtual complete filling of the pores at its vapor pressure and room temperature. In fact, at 400 mmHg more than one molecule of pentane (whose Van der Waals length equals 9.2 Å) is accommodated in every elementary cell, whose channel length is around 1 nm.
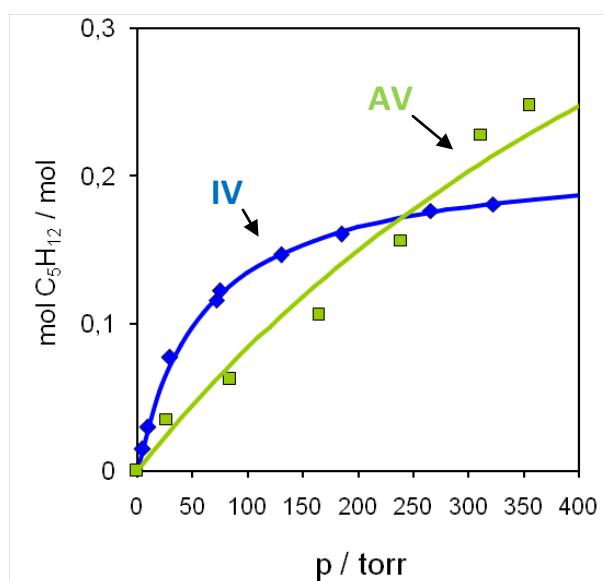
Fig. 44 – Isotherms of adsorption of pentane on IV (blue) and AV (green) at room temperature

Adsorption from the vapor phase is then an elegant and clean way to provide the monomer feed to the microporous dipeptides up to the maximum allowed amount that can be filed in the nanochannels. Alternatively, soaking of porous matrix in liquid monomer would be an option, but careful degassing would be required in order to remove the excess reagent without evacuating the pores at the same time.

In a general synthesis, 500 mg of activated (10^{-2} mmHg at 60°C overnight) nanoporous dipeptide powder (AV, VA, IV or IV, purchased from Bachem, Switzerland) is put in a sealable glass vial which is then connected to the system sketched in Fig. 44 and further evacuated (10^{-2} mmHg) for a few hours. After isolating the vial containing the microporous matrix, liquid monomer (all from Sigma-Aldrich), contained in a second vial, is degassed by means of three

freeze-pump-thaw cycles or until no effervescence is detected. The monomer vapors are then allowed to expand and get in contact with the dipeptide matrix during three days to complete the monomer adsorption.
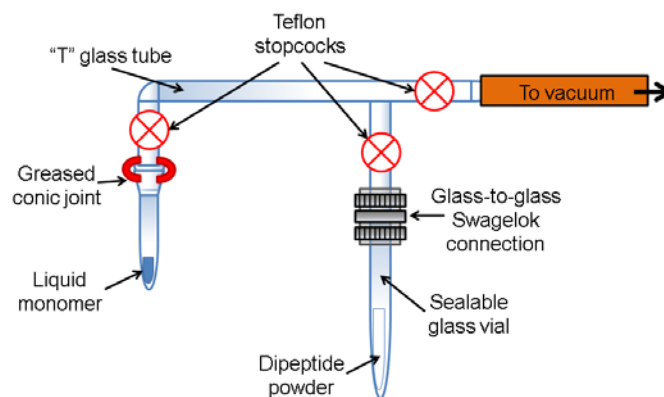
Fig. 45 – Vacuum system used for monomer adsorption and vial sealing

Then, dipeptide⊃monomer adduct is isolated and vacuum-sealed: the glass vial, still connected to the transfer system, is immersed in a liquid nitrogen bath and sealed with the help of a collimated butane flame. The liquid nitrogen bath has the double function of condensing monomer vapors and avoid overheating of the dipeptide during glasswork. The sealed vial is then γ-irradiated (using a ^{60}Co source) up to a dose of 0.8 Mrad (8 kGy) during a period of 24 h, at room temperature. Treatment with highly energetic and penetrating ionizing radiation generates radicals by homolysis of double bonds; free radicals then propagate to neighboring monomers in the nanocavity leading to chain growth. In this regard, polymerization time is critical to make sure that reaction has proceeded to completion; for this reason each sample is allowed to sit for a conservative time (at least two weeks) before further processing and characterization.

3.3. Nanocomposite recovery and characterization

After the polymerization time, the vials are broken using a glass cutter and the product is collected making sure to avoid contamination with glass splinters. The white powder is evacuated overnight at 60 °C to remove any unreacted monomer, prior to characterization.

3.3.1. X-Ray Powder Diffraction (XRPD)

To make sure that monomer adsorption and irradiation is not detrimental to the porous architecture of the dipeptide, the crystalline nature of the supposed dipeptide⊃polymer nanocomposite is verified and compared to the *pristine* dipeptide.

For example, AV dipeptide structure is retained after polymerization as can be clearly seen in Fig. 45. The peak of index (100) highlighted in inset a) is associated to the pore periodicity and is extremely intense in the case of the empty matrix; however, the same peak has a much lower intensity in the case of the nanocomposite because of the reduction in electronic density contrast due to filling of the pores. Beside the change in intensity of peak (100), other minor relative intensity variations can be found at higher 2θ but peak positions are maintained proving that the overall architecture is intact.
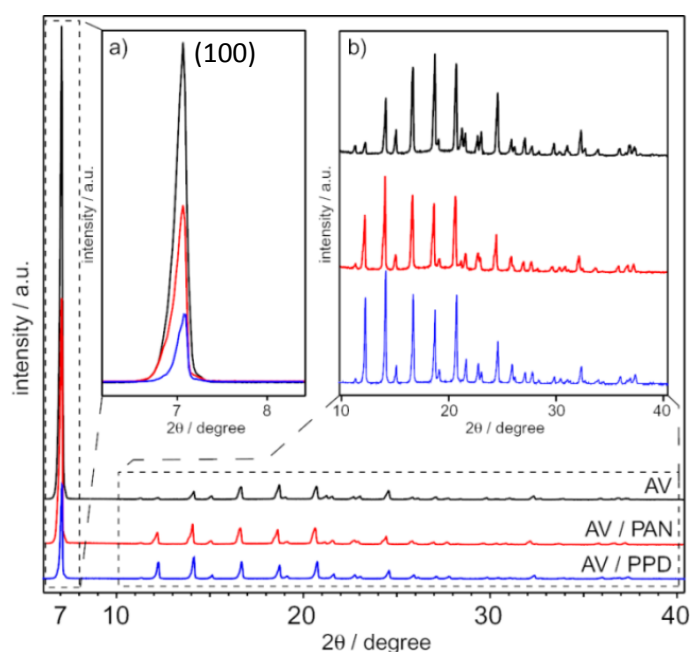
Fig. 46 – Comparison between XRPD of pristine AV (black), AV⊃PAN (red) and AV⊃PPD (blue) nanocomposites
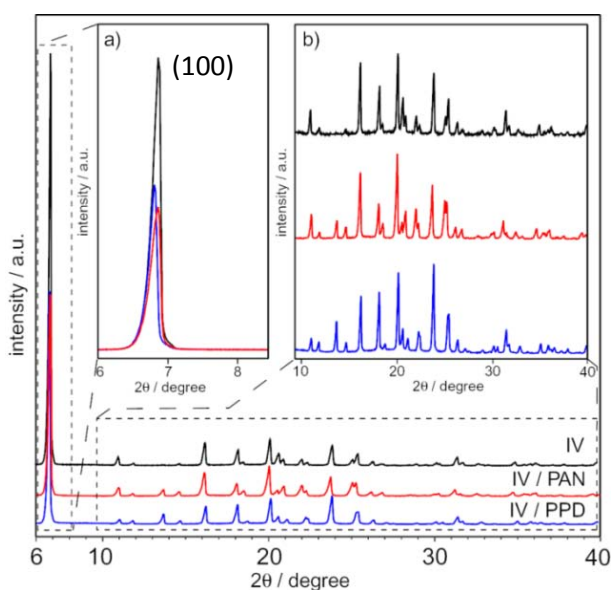
Fig. 47 - Comparison between XRPD of pristine IV (black), IV⊃PAN (red) and IV⊃PPD (blue) nanocomposites
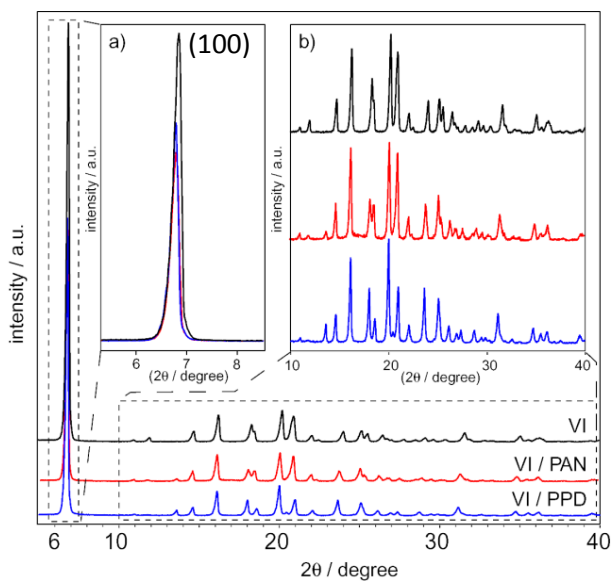
Fig. 48 - Comparison between XRPD of pristine VI (black), VI⊃PAN (red) and VI⊃PPD (blue) nanocomposites

The above considerations hold for IV and VI nanocomposites (Fig. 46 and Fig. 47), indicating the general stability of the dipeptide architecture during the nanocomposite preparation. Occurrence of polymerization outside the porous matrix can be ruled out, since polyacrylonitrile pseudocrystalline diffraction peak, corresponding to an interplane distance of

5.2 Å (2θ = ~17° for Cu Kα radiation), is absent[69]. Similarly, no amorphous diffraction band, ascribable to esternally polymerized pentadiene, is observed.

Quantitative and highly resolved diffractograms have been acquired on AV, IV and VI dipeptides and their nanocomposites with polyacrylonitrile using synchrotron radiation, in order to perform structural refinement (see Appendix C) and highlight any slight structural changes occurring when a guest is present in the nanochannels.
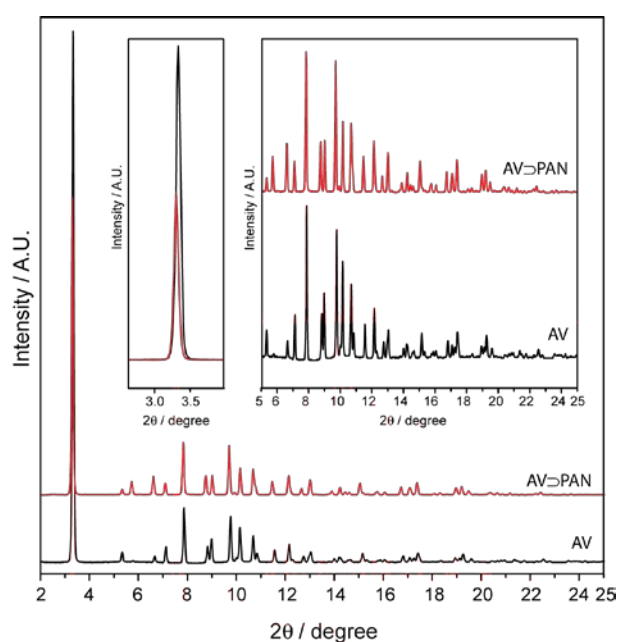
Fig. 49 – Comparison between AV (black) and AV⊃PAN (red) synchrotron radiation diffractograms

Indeed, as shown in Table 3, all the nanocomposites investigated undergo an increase in elementary cell volume associated with enlargement of *a* and *b* equivalent axis which are perpendicular to the nanochannel direction. On the other hand, slight shrinkage of the *c* axis is evidenced. Dipeptide organic zeolites have proven to undergo minor structural rearrangement when a guest is encapsulated; for instance, AV⊃methanol adduct, obtained by soaking of single crystals of AV in methanol solvent, demonstrates the same behavior as dipeptide⊃polymer nanocomposite with linear enlargement perpendicular to the channel leading to the overall cell volume expansion[70].

Table 3 - Room temperature crystal structure data and refined unit cell parameters of dipeptides and dipeptide PAN nanocomposites

Compound	AV	AV PAN	IV	IV PAN	VI	VI PAN
Empirical formula	$C_8H_{16}N_2O_3$	$C_8H_{16}N_2O_3$ $(CH_2CHCN)_n$	$C_{11}H_{22}N_2O_3$	$C_{11}H_{22}N_2O_3$ $(CH_2CHCN)_n$	$C_{11}H_{22}N_2O_3$	$C_{11}H_{22}N_2O_3$ $(CH_2CHCN)_n$
Crystal system	Hexagonal	Hexagonal	Hexagonal	Hexagonal	Hexagonal	Hexagonal
Space group	$P6_1$	$P6_1$	$P6_1$	$P6_1$	$P6_1$	$P6_1$
a / Å	14.4448(5)	14.5697(2)	14.8787(6)	14.9787(2)	14.7892(5)	14.8758(5)
c / Å	10.0058(7)	9.9526(3)	10.3048(5)	10.2927(3)	10,3271(4)	10.2768(3)
Cell volume / Å³	1808.0(2)	1829.43(7)	1975.6(1)	1999.89(7)	1956.2(1)	1969.4(2)

Fig. 50 – Comparison between IV (black) and IV⊃PAN (red) synchrotron radiation diffractograms
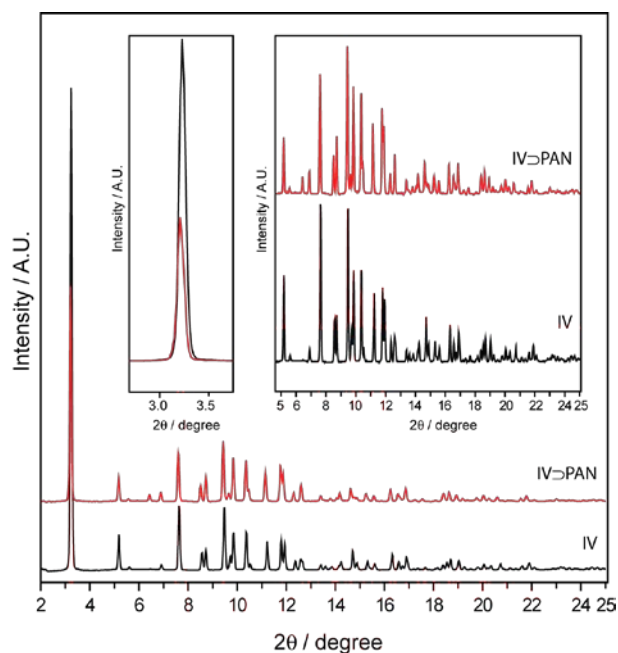
Fig. 51 – Comparison between VI (black) and VI⊃PAN (red) synchrotron radiation diffractograms

3.3.2. Thermogravimetric analysis (TGA)

XRPD characterization has confirmed that polymerization did not lead to collapse of the channels or degradation of the crystalline quality of the host matrix. Moreover, X-ray

diffraction suggested that electron density is present in the nanochannels. It was noticed that after monomer adsorption, polymerization and dipeptide recovery, each sample gained weight with respect to the starting amount loaded in the sealed vial (5%-15% mass increase). However, quantitative assessment of the host/guest ratio requires additional investigation. In this regard, termogravimetry can elucidate the polymer content in the nanocomposites: in fact, dipeptides have characteristic behavior at high temperature and are completely degraded above 300 °C. The mass residue is then a direct measure of the polymer amount. Polydienes are known to be stable up to 350 °C if heated in an inert atmosphere while polyacrylonitrile has a reproducible degradation behavior (Fig. 51): this enable the precise calculation of host/guest adduct composition.
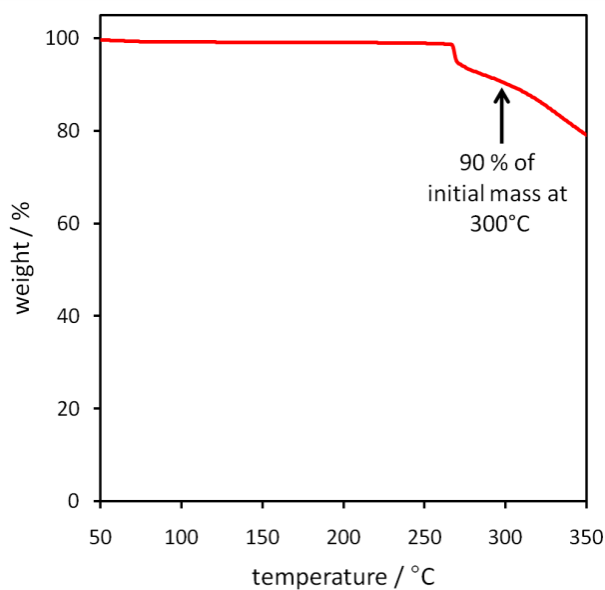
Fig. 52 – Thermal degradation of a bulk-polymerized PAN

For instance, AV dipeptide has a degradation onset at 250°C and is completely removed at 300°C (Fig. 52, black curve). Instead AV⊃PAN and AV⊃PPD nanocomposites leave a residue corresponding to 14.6 % wt PAN and 7.2 % wt PPD content (Fig. 52, red and blue curves respectively).

If the PAN repetition distance is taken into consideration (2.5 Å, typical of vinyl polymers in *trans* conformation) together with the effective nanochannel length of a unit cell of AV[71] it is possible to calculate the theoretical maximum polymer content in a hypothetical 100% filled AV⊃PAN nanocomposite; quite remarkably, the measured 14.6% wt content is close to the theoretical limit of 16.7 % wt, indicating that polyacrylonitrile chains fill the pores of AV almost completely (87% of available space). However, since polymer formation implies creation of new covalent bonds which shorten the distance between monomers, we can affirm that pore occupation prior to polymerization is even higher.
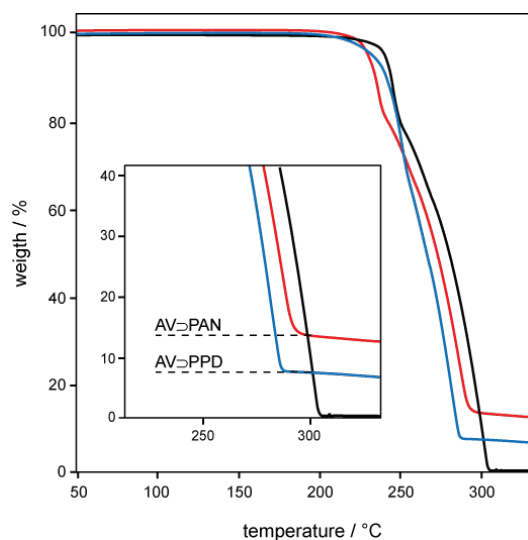
Fig. 53 – Thermogravimetric analysis comparison of AV dipeptide (black), AV⊃PAN (red) and AV⊃ PPD (blue) nanocomposites

If we take into consideration the thermograms of IV, VI and their respective nanocomposites with PAN and PPD a general trend can be observed with PAN content being higher than PPD, as summarized in Table 4. Clearly, polymer content is correlated to the degree of conversion of the monomer, suggesting that vinyl polymerization is more favored than diene polymerization in confined spaces, also because higher relative reactivity of the vinyl radical.

Table 4 – Summary of thermogravimetric analysis and polymer content in nanocomposites

PAN nanocomposites			
Sample	PAN amount / % wt	Theoretical maximum PAN amount / % wt	Pore filling / %
AV⊃PAN	14.6	16.74	87
IV⊃PAN	8.2	15.34	53
VI⊃PAN	11.1	13.89	80
PPD nanocomposites			
Sample	PPD amount / % wt	Theoretical maximum PPD amount / % wt	Pore filling / %
AV⊃PPD	7.2	11.86	61
IV⊃PPD	4.9	10.82	52
VI⊃PPD	3.0	9.74	31
PI nanocomposites			
Sample	PI amount / % wt	Theoretical maximum PI amount / % wt	Pore filling / %
AV⊃PI	10.7	11.86	84
VA⊃PI	10.5	13.42	77

Larger pore size appear to have an influence on polymerization degree, since AV has the highest polymer content in both cases. In fact, larger channel diameter should favor monomer diffusivity and suitable arrangement of transition states, together with higher guest/host stoichiometric ratios[88]. For instance, PPD content decreases with decreasing pore volume in the series AV, IV and VI and the same occurs for PAN. Exception to this trend is represented by the VI⊃PAN system: even if VI pores are smaller than IV's, polymerization proceeds to a relevant extent (80% filling) maybe because of the more regular cylindrical geometry of the VI channel where polyolefin chain can be accommodated in extended conformation. Finally, polyisoprene, whose polymerization was carried out in the larger AV and VA channels to promote higher conversion, produces nanocomposite with pore filling above 70%.

3.3.3. Solid State Nuclear Magnetic Resonance spectroscopy (SS NMR)

Solid State ^{13}C Cross-Polarization Magic Angle Spinning NMR spectroscopy (^{13}C CP MAS NMR) was employed to directly observe the presence of polymerization products in the nanochannels. For instance in the case of AV⊃PAN adduct (Fig. 53, red curve), it is possible to recognize, beside the sharp peaks that can be ascribed to the matrix (black spectrum), several additional signals which belong to polyacrylonitrile. Polymer nitrile carbon is found as a broad peak centered at 121.70 ppm. Instead, polyacrylonitrile backbone methine and methylene carbons, whose isotropical chemical shifts fall at 27.0 ppm and 32.5 ppm respectively[72], appear as a unique coalesced broad peak centered at 31 ppm. Unreacted monomer is also evidenced, whose vinyl signals (=$\underline{C}$H$_2$, 128.80 ppm and =$\underline{C}$H, 108.20 ppm) are clearly recognizable (while monomer nitrile carbon is buried under the more intense polymer signal). At present state, nothing can be said about PAN stereoregularity, since polymer signals are not resolved enough.
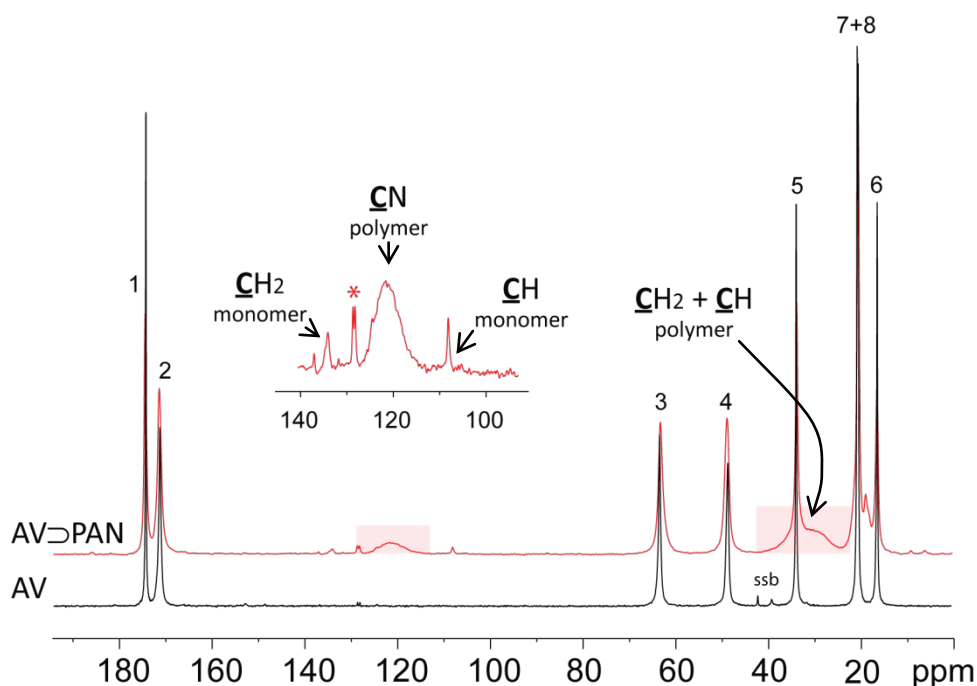
Fig. 54 – Comparison between ^{13}C CP MAS NMR spectra of AV (black) and AV⊃PAN nanocomposite (red)
Experimental conditions:
AV: spinning speed 10 kHz, 2.5 ms contact time
AV⊃PAN: spinning speed 12.5 kHz, 2.0 ms contact time
Asterisk designates a toluene impurity

AV⊃PPD nanocomposite ^{13}C CP MAS NMR spectrum is shown in Fig. 54 (blue curve). In the double bond region, several liquid-like sharp peaks appear: again, they belong to unreacted *trans*-1,3-pentadiene (128.4, 132.7 e 137.4 pmm). Polypentadiene signals are broader peaks centered at 138.9 and 126.9 ppm (olefinic carbons) and at 41.0 and 37.1 ppm (aliphatic methyne and methylene carbons respectively); methyl carbon expected around 20 ppm is buried below the matrix signals. From the preliminary evaluation of the polypentadiene absorption, a regular microstructure can be expected since a complex microstructure would be reflected on the presence of a higher number of NMR signals.
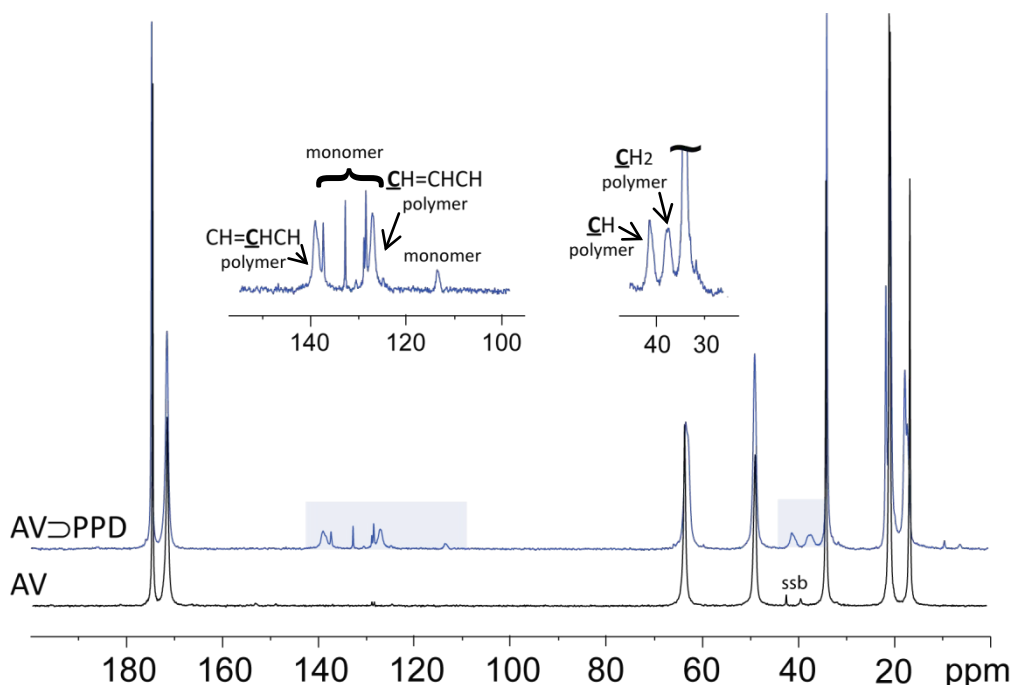
Fig. 55 – Comparison between ^{13}C CP MAS NMR spectra of AV (black) and AV⊃PAN nanocomposite (blue)
Experimental conditions:
AV: spinning speed 10 kHz, 2.5 ms contact time
AV⊃PPD: spinning speed 5 kHz, 2.5 ms contact time
"ssb" indicates spinning sidebands

The presence of acrylonitrile and pentadiene monomers, even after heat treatment and evacuation, is a fingerprint of monomer confinement in the nanopores: polymer chains prevent unreacted monomer from being desorbed because diffusive paths to the pore openings are blocked.

Table 5 – Chemical shift table of ^{13}C NMR signals of AV in the empty host and in nanocomposites

			AV	AV⊃PAN	AV⊃PPD
	#	carbon	δ / ppm	δ / ppm	δ / ppm
AV ^{13}C signals	1	**C**OO$^-$ (V)	174.80	174.70	174.78
	2	**C**=O (A)	171.76	171.66	171.59
	3	α-**C**H (V)	63.32	63.24	62.94
	4	α-**C**H (A)	48.54	48.83	48.78
	5	β-**C**H (V)	33.69	33.76	33.76
	7+8	**C**H$_3$ (V)	20.44 20.23	20.47 (18.84)	21.36 20.38
	6	**C**H$_3$ (A)	16.11	16.379 (18.84)	16.62 17.00

This feature is common to all the examined nanocomposites (see Appendix C). Monomer encapsulation is further confirmed by thermogravimetry, where no weight loss associated to monomer evolution is observed up to the decomposition of the matrix. In fact, *trans*-1,3-pentadiene and acrylonitrile have boiling point at 42°C and 77°C respectively and, if not incarcerated, desorption should occur at slightly higher temperatures. Instead, only as the nanoporous architecture is dismantled, concomitant monomer liberation and matrix vaporization occur. This phenomenon is in agreement with previously reported tunnel systems[7374] where volatile monomer entrapment is achieved by macromolecular "stopcocks".

As powder X-ray diffraction suggested above, slight structural rearrangement happen in the peptide architecture when polymer chains are accommodated in its channels; moreover, the presence of a guest is expected to modify the chemical environment experienced by the host ^{13}C nuclei, and therefore their resonance with respect to the unperturbed empty matrix. Since methyl groups of the dipeptides are known to be exposed towards the center of the channels, these groups may be influenced more strongly by the guest inclusion: indeed, as shown in Fig. 55, the two valine CH$_3$ signals and that of the alanine CH$_3$ of AV⊃PPD adduct (in blue) undergo splitting and downfield shift (up to 0.9 ppm).
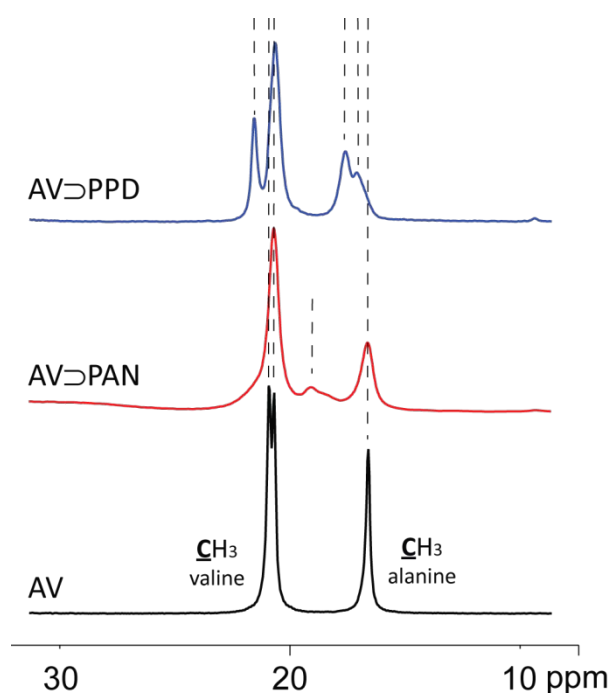
Fig. 56 – SS CP MAS [13]**C NMR comparison between AV and nanocomposites methyl region**
Experimental conditions as above.

AV⊃PAN adduct shows a weak peak at 18.84 ppm which cannot be unambiguously assigned since might be either the alanine or valine CH_3 peak downfield or upfield shifted respectively. Polymer nitrile groups or alkene moieties have characteristic (de)shielding behavior depending on relative orientation of the "shielding cone" with respect to the surrounding nuclei: it is likely that part of the methyl groups of the matrix is influenced by these effects. Signals belonging to ^{13}C nuclei which are placed farther away from the channel axis are least influenced with minor chemical shift differences.

3.3.3.1.   Scanning Electron Microscopy (SEM)

Morphological characterization was carried out on the nanocomposites to investigate any changes between the empty matrix and the crystalline powder after polymerization. No differences could be observed, nor the presence of external polymer particles. AV⊃PAN, for instance, only shows crystalline needle-shaped hexagonal crystals completely similar to the *pristine* material (and Chapter 4).
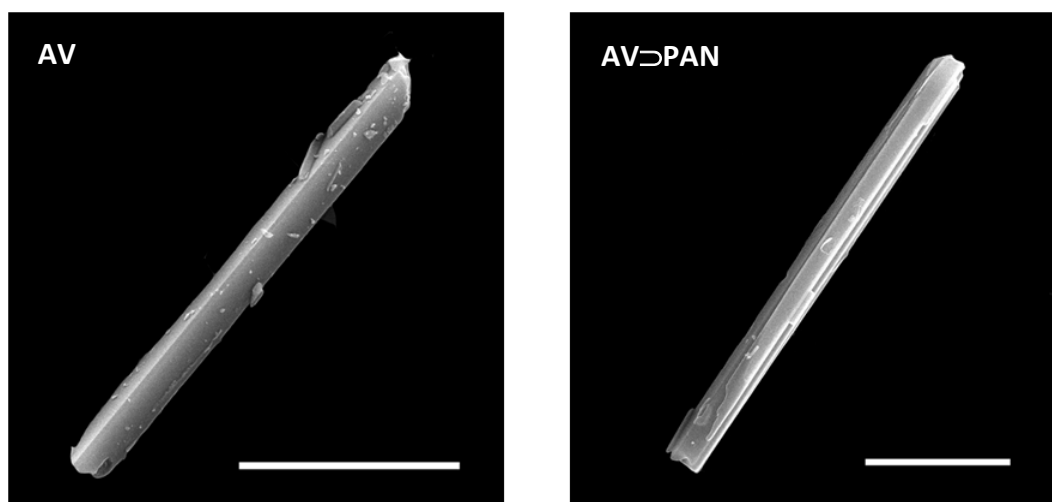
Fig. 57 – SEM images of an AV crystal (left) and of an AV⊃PAN nanocomposite crystal (right). Scale bars equal 20μm

3.4. Polymer recovery and characterization

Aliphatic dipeptides, even if bearing an hydrophobic side chain, are soluble in water. Instead, polyacrylonitrile, polypentadiene and polyisoprene are completely insoluble. It is then possible to dismantle the porous architecture by simply treating the nanocomposites with deionized water in order to recover the insoluble polymer. In the case of PAN nanocomposites, dissolving the dipeptide⊃polymer adduct in water yielded solid polymer particles which were filtered under reduced pressure and washed thoroughly on the filter. After drying by means of mild thermal treatment (40°C) and *in vacuo* overnight, pure polyacrylonitrile powder is obtained (see below). Polyisoprene is recovered in the same way, yielding an elastomeric mass. In the case of polypentadiene, where the liberation of polymer chains isn't obtained by solely water treatment it is necessary to dissolve the polymer using chloroform: an extraction using water/chloroform system is necessary; the organic phase is collected, dried over anhydrous Ca_2SO_4, filtered, concentrated and then polypentadiene is precipitated in excess methanol prior to drying as above. Apparently, chloroform helps the peptide dissolution in water by dissolving the impermeable polymer layer which builds up and surrounds the nanocomposite particles as polypentadiene is freed. The polymer yield is in line with the TGA data, even though part of the product is lost during purification; on average, from 500 mg of starting nanocomposite, from 25 mg to 50 mg polymer could be obtained.

3.4.1. Characterization of *in situ* polymerized polypentadiene (PPD)

3.4.1.1.   NMR spectroscopy

Solution ^{1}H and ^{13}C NMR spectroscopy is a powerful tool to assess polymer microstructure. In particular, ^{13}C NMR can elucidate the polymer nature. In Fig. 57 the carbon NMR spectra of PPD extracted from AV, IV and VI are reported.
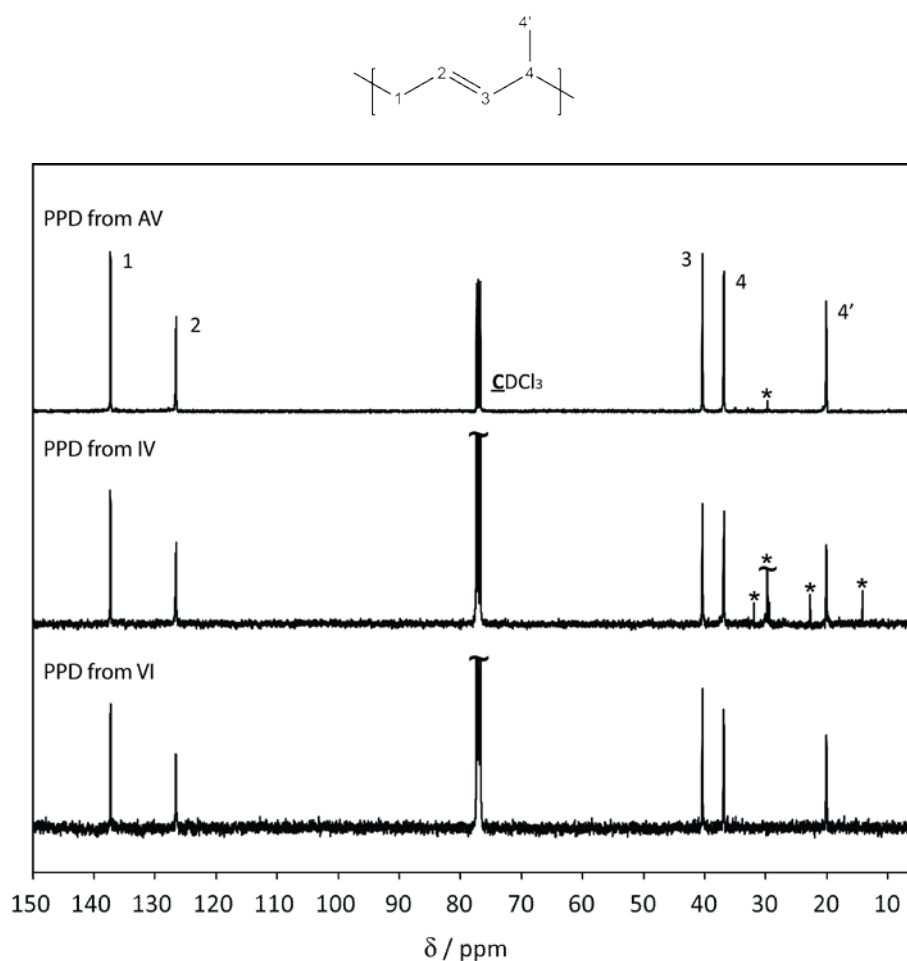
Fig. 58 – ^{13}C NMR spectra (100 MHz, CDCl$_3$) of polypentadiene polymerized in AV (top), IV (center) and VI (bottom). Asterisks denote trace impurities (*n*-hexane and "grease"[75])

Particularly regular structure can be envisaged for such simple spectra where only five main anisochronous signals are found. Channel polymerization is expected to yield 1,4 polymers because of favorable accommodation of linear pentadiene in the narrow channels of

dipeptides thus the five main peaks (e.g. PPD from AV) are compared to the literature reported chemical shifts of 1,4 polypentadiene. Moreover, *trans*-1,3-pentadiene polymerization in clathrates is known to produce linear polymers with a high degree of regularity (even stereochemical). Indeed, the polymer structure corresponds exactly to a regular 1,4-*trans* polymer[76].

Table 6 – ^{13}C NMR chemical shift, assignments and peak integrals of 1,4-*trans*-polypentadienes obtained in AV, IV and VI
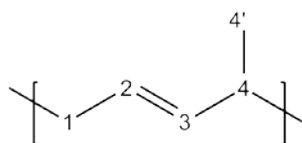
label	^{13}C		PPD from AV			PPD from IV			PPD from VI		
			δ / ppm	Integral		δ / ppm	Integral		δ / ppm	Integral	
C1	$\underline{C}H_2$	*mm (rr)*	40.30		0.25	40.30		0.25	40.30		0.25
		mr + rm	40.33	1.03	0.50	40.33	1.07	0.49	40.33	0.98	0.50
		rr (mm)	40.37		0.25	40.37		0.26	40.36		0.25
C2	$\underline{C}H$	*mm (rr)*	126.50		0.25	126.50		0.26	126.50		0.24
		mr + rm	126.53		0.26	126.53		0.25	126.53		0.25
			126.59	0.96	0.23	126.60	1.05	0.24	126.59	0.93	0.25
		rr (mm)	126.63		0.26	126.63		0.25	126.63		0.26
C3	$\underline{C}H$	*m, r*	137.26	0.99	0.50	137.27	1.02	0.49	137.27	0.81	0.50
			137.30		0.50	137.30		0.51	137.31		0.50
C4	$\underline{C}H$	*m, r*	36.83	1.05	0.49	36.83	1.08	0.50	36.83	0.94	0.50
			36.92		0.51	39.92		0.50	36.92		0.50
C4'	$\underline{C}H_3$	*mm*	19.97		0.25	19.96		0.26	19.96		0.24
		mr + rm	20.04	1.00	0.47	20.03	1.00	0.49	20.03	1.00	0.50
		rr	20.11		0.28	20.11		0.25	20.11		0.26

1,4-*cis* structure, even if linear, yields a bulkier cross-section and its characteristic signals, expected around 30.5 and 33.6 ppm (C4 and C1 respectively) are absent even in the larger AV channels[77]. The lack of head-to-head and tail-to-tail signals, expected around 42.5, 33.0 and

18.5 ppm, is a proof of regioregularity where only head-to-tail sequences are allowed to polymerize[78]. Unlike polypentadiene obtained in PHTP clathrates which exhibit remarkable stereoregularity (it is in fact highly isotactic), dipeptide-polymerized polypentadiene signals have a fine structure which can be interpreted at the triad level: for instance, methyl signal is affected by stereosequences and is split into four peaks belonging to the *mm* (19.97 ppm), *mr* + *rm* (almost superposed and centered at 20.04 ppm) and *rr* (20.11 ppm) triads. Integration and deconvolution into the different peak contributions (see Table 6) leads to the conclusion that each triad has equivalent statistical weight: *mm*, *mr*, *rm* and *rr* sequences are in a substantial 1:1:1:1 internal ratio, namely the polymer is perfectly atactic. This picture is in accordance with polymer macroscopic appearance, since regular isotactic 1,4-*trans*-PPD is a semicrystalline polymer with melting point at about 90°C[79,80], while in our case the atactic polymer appears as a rubber.

Strikingly, PD polymerized in tighter IV and VI channels show the very same microstructure as the AV product: apparently, linear channel geometry generates an atactic 1,4-*trans*-polypentadiene regardless of pore diameter and helicity.
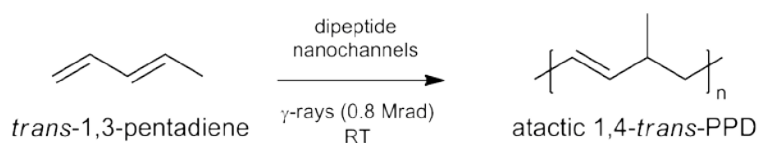
Fig. 59 – Channel polymerization of *trans*-1,3-PD in AV, IV and VI dipeptides affords microstructural selection, producing only atactic 1,4-*trans*-PPD amongall the theoretically predictable pool of structures (see Fig. 40)

3.4.1.2.   Steric-Exclusion Gel Permeation Chromatography (SEC GPC)

NMR spectroscopy on polypentadiene has elucidated its structure and further shows that terminal units are not detectable, indicating polymerization has proceeded up to a relevant number of repeating units. SEC GPC measurement (Fig. 59) shows unimodal molecular weight distribution with polydispersity index ranging from 2 to 4 and molecular weight, expressed in polystyrene equivalents, up to about 70 kDa (see Table 7). It is noteworthy that, since polypentadiene has a more flexible structure with respect to polystyrene reference, the measured molecular weights represent a lower boundary for the real PPD weights.
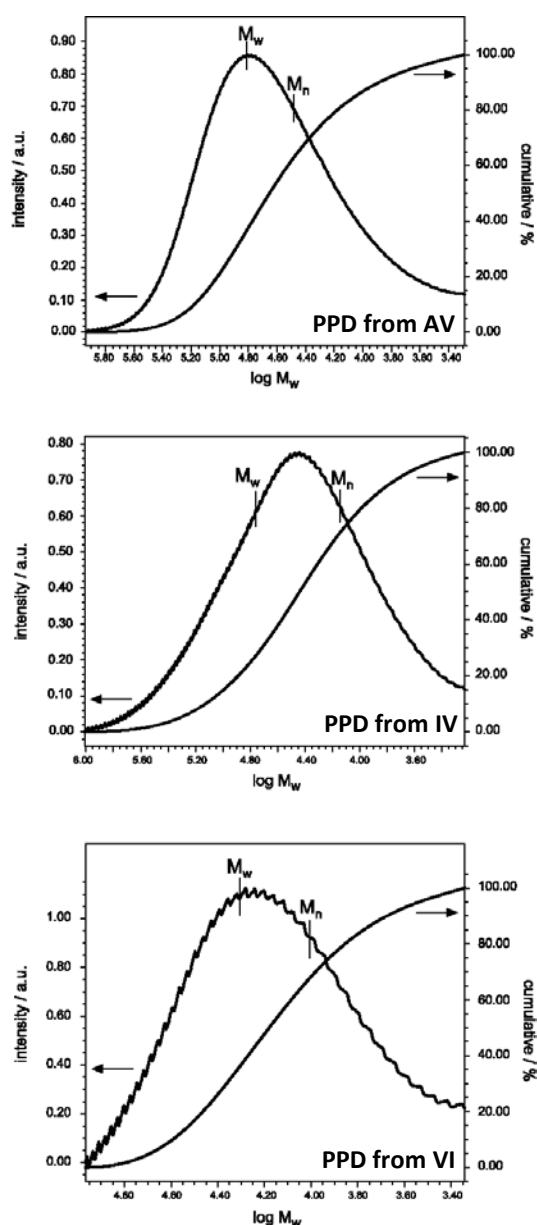
Fig. 60 – Size-Exclusion Gel Permeation Chromatography of 1,4-trans-polypentadiene polymerized in AV (top), IV (middle) and VI (bottom) dipeptides.

Table 7 – Summary of GPC data on various *in situ* polymerized PPD samples.

Nanoporous matrix	AV	IV	VI
M_w / kDa	67.8	55.9	19.1
M_n / kDa	19.3	13.9	10.4
Polydispersity index / $M_w M_n^{-1}$	3.47	4.02	1.83

3.4.2. Characterization of *in situ* polymerized polyacrylonitrile (PAN)

3.4.2.1.   Differential Scanning Calorimetry (DSC)

Polyacrylonitrile has a well known DSC fingerprint, showing glass transition temperature (T_g) between 80°C and 120°C and exhibiting an exothermic transition at 270°C. Native PAN, freed from the nanocomposite matrix by water dissolution, was characterized by DSC in order to evaluate its purity and the lack of dipeptide transitions. In fact, AV, IV and VI have intense endothermic transitions between 200 °C and 270 °C which would reveal even trace impurity (refer to Chapter 5 for details). Even if polymer recovery was particularly mild (merely washing with deionized water at room temperature), all the dipeptide is removed, as shown in Fig. 60, where only the exothermal cyclization-aromatization of nitrile groups is revealed[81]. Raising the heating ramp to 20 K/min^{-1} allows to highlight also the broad T_g of PAN.
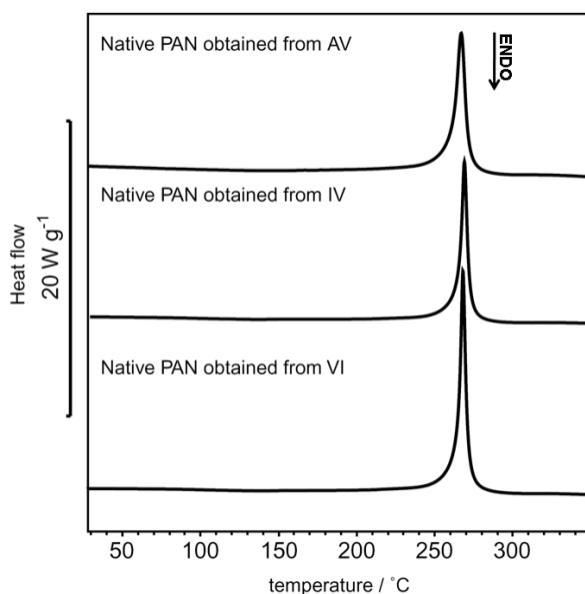
Fig. 61 – PAN cyclization (270 °C) of polymers obtained in AV (top), IV (middle) and VI (bottom).
Heating rate: 10K min^{-1}, N$_2$ flow: 80 ml min^{-1}
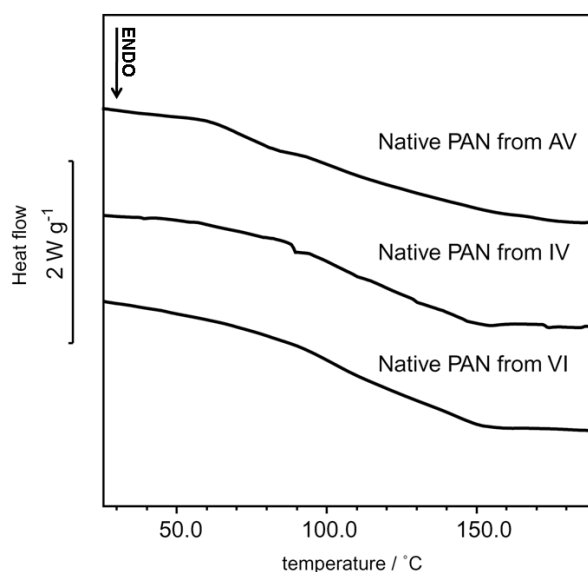
Fig. 62 – Glass transitions (T_g) of PAN obtained from AV (top), IV (middle) and VI (bottom).
Heating rate: 20K min^{-1}, N$_2$ flow: 80 ml min^{-1}

3.4.2.2. X-ray Powder Diffraction of PAN (XRPD)

An additional confirmation of removal of the matrix from the recovered polymer is given by the XRPD diffractograms on PAN from AV powders. Polyacrylonitrile is a pseudocrystalline polymer whose structure has been interpreted as the lateral hexagonal packing of rod-like chain molecules[82,83] and features a strong peak corresponding to interplane distances of 5.2 - 5.3 Å, regardless of polymer stereochemistry or sample preparation. An additional weaker peak belonging to the [101] lattice plane[69] is also found around 3.1 Å, beside a broad amorphous band centered at $2\theta = 25°$.
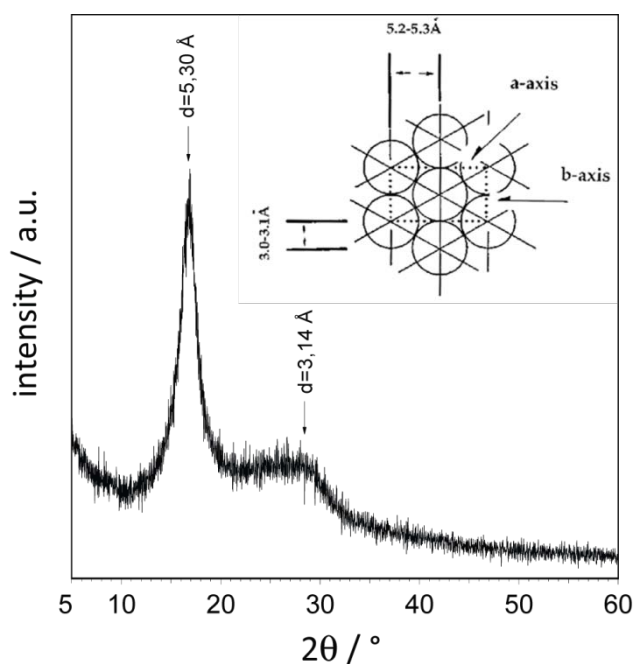
Fig. 63 – XRPD pattern of PAN polymerized in AV. Scheme in the upper-right corner is a representation of supposed hexagonal arrangement of polymer chains developing perpendicular to the page (adapted from Ref. 83)

Complete removal of AV matrix is demonstrated, since no reflections other than those of polyacrylonitrile are observed.

3.4.2.3. Viscosimetric Molecular Weight (Mw$_v$) determination of PAN

Molecular weight of *in situ* polymerized PAN is higher than that of PPD obtained under the same conditions; this result is in agreement with TGA data where conversion of acrylonitrile proved higher than that of pentadiene monomer. Straight nanopores of VI demonstrate to be particularly suited for PAN polymerization since high monomer conversion is accompanied by remarkably high molecular weight (over 200 kDa). On the other hand, acrylonitrile polymerization in AV lead to comparable monomer conversion but lower average chain length.

Table 8 – Viscosimetric molecular weights of *in situ* polymerized PAN samples

Nanoporous matrix	AV	IV	VI
Mw$_v$ / kDa	50 ~ 60	60 ~ 100	160 ~ 270

3.4.2.4. NMR spectroscopy

^{13}C NMR spectrum of PAN obtained in AV is reported in Fig. 63 (top). Three anisochronous signals are found at 27.0, 32.5 and 119.4 ppm corresponding to CH, CH_2 and CN carbons respectively. Inversion of the usual methine and methylene order depends on the diamagnetic shielding effect imparted by side nitrile group on the backbone CH carbon.
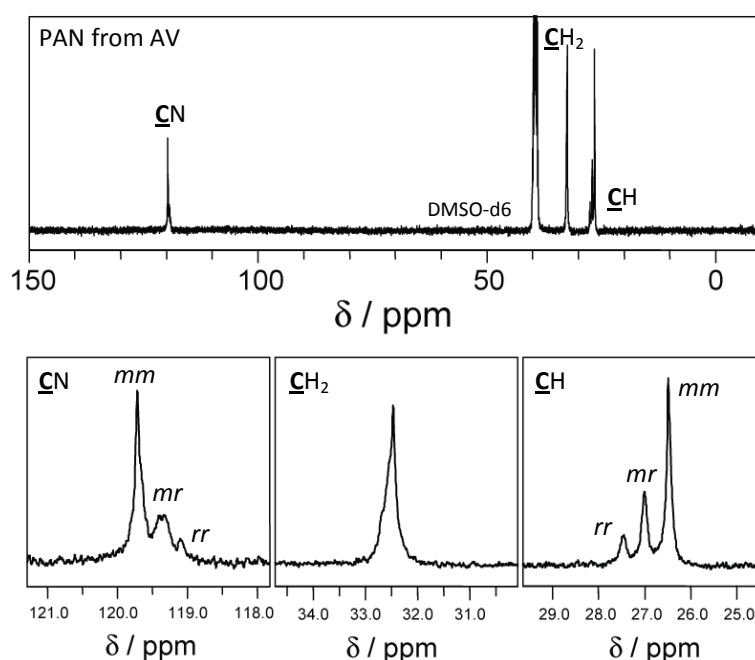
Fig. 64 – ^{13}C NMR (100 MHz, DMSO-d$_6$) spectrum of PAN polymerized in AV nanochannels. Whole spectrum (top) and expansions of nitrile, methylene and methine signals (bottom).

Similarly, nitrile signal is sensitive to the triads sequences and is split into three contributions corresponding to isotactic (119.72 ppm), syndiotactic (119.10 ppm) and heterotactic (119.37 ppm) situations. The shape of methylene carbon is asymmetric, suggesting unresolved splitting. It is evident that polymerization in AV nanochannels yields a substantially isotactic polymer and quantification of the relative abundance of each triad sequence, performed by signal deconvolution of the methine absorption, states that the probability of finding isotactic triads (*mm*) along the chain is P_{mm} = 59% (P_m > 70%). Since *mr* probability roughly doubles the probability of *rr* triads (P_{rr} = 12%, P_{mr} = 29%) the statistical microstructural picture corresponds, to a first approximation, to a situation where stereoregular isotactic blocks are interrupted by an *rr* sequence. Isolated *rr* triads can be produced in presence of a self-correction mechanism

thanks to which, after a heterotactic diad insertion, the absolute configuration is recovered by means of a second *r* diad (Fig. 64). Every isolated *rr* sequence is associated to two *mr* (*rm*) equivalent sequences which produce an NMR signal having twice the intensity.
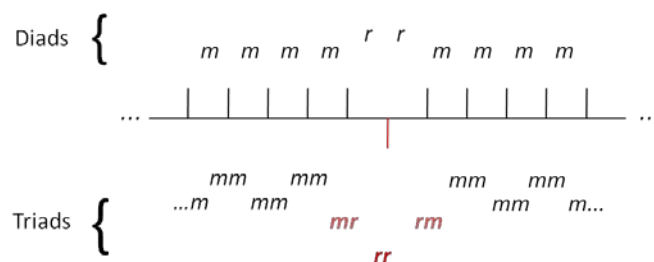
Fig. 65 – Proposed steresequence for AV polymerized PAN

Confinement affects stereoregularity as occurs in the case of γ-ray initiated urea IC acrylonitrile polymerization, where highly isotactic PAN was obtained below room temperature. In general, radical polymerization of acrylonitrile yields atactic products independent of polymerization temperature and solvents[84] since no control is present. In the same way, ^{60}Co γ-irradiation of acrylonitrile liquid monomer is reported to produce random tacticity[85]. Random tacticity is observed also in confined spaces where the vessel dimension is large compared to the monomer size (like for mesoporous silica[86]) while as soon as the reaction pore size approaches the sub-nanometer domain, deviation from the atacticity is evidenced. For instance, PAN polymerized under comparable conditions in two zeolites having different inter-cage pore size (Na–Y and Na–β, 7.4 and 5.5 Å respectively) show slight isotacticity which is inversely proportional to pore diameter[87]. Another striking case is the couple of cyclotriphosphazene-based organic zeolites tris(*o*-phenylenedioxy)cyclotriphosphazene (TPP) and tris(2,3-naphthylenedioxy)-cyclotriphosphazene which are provided with 5 and 10 Å diameters respectively: highly isotactic PAN is formed in the smaller channel[85], while the bigger results in non-specific polymerization[88]. A 5 Å channel diameter seems most suitable for the obtaining of isotactic PAN, as reported for TPP and urea clathrates and as confirmed in our case, in AV dipeptide. However, if the polymerization of acrylonitrile is carried out in the smaller channels of IV and VI, the atactic polymer is obtained (Fig. 65), indicating that the relationship between pore size and polymer microstructure is not straightforward. In fact, further reduction in the

channel dimension with respect to AV dipeptide has detrimental effect on the stereoregularity of the product: apparently, only an optimal channel size is able to produce isotactic polyacrylonitrile.
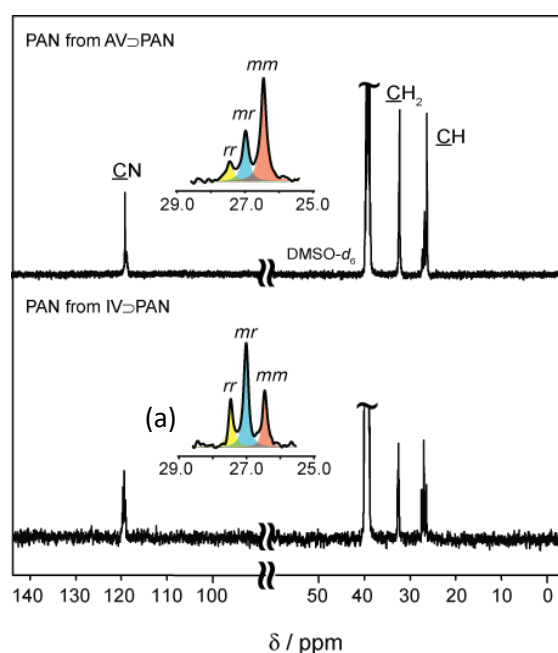
Fig. 66 – ¹³C NMR spectra (100 MHz, DMSO-d₆) of PAN polymerized in AV (top) and IV (bottom) nanochannels. Expansion of the methine carbon of IV polymerized PAN (a) shows atactic structure with *mm*, *mr* and *rr* triads in a 1:2:1 ratio.

3.4.2.5. Comparison of channel morphologies and further investigations

The highest isotactic polyacrylonitrile reported in the literature has been obtained by means of canal polymerization in urea inclusion compound and urea IC hexagonal substructure can be considered as an optimal nanovessel to attain stereochemical control. For this reason we compared our systems to urea, in search of structural analogies that could explain our results. In Fig. 66 - Van der Waals empty volumes of AV, IV and VI, compared with the one of urea inclusion compound substructure.Fig. 66 the Van der Waals volumes of AV, IV and VI channels (one repetition length) is compared with the channel volume of urea in its hexagonal substructure when forming inclusion compounds (urea/dibromodecane IC[89]).
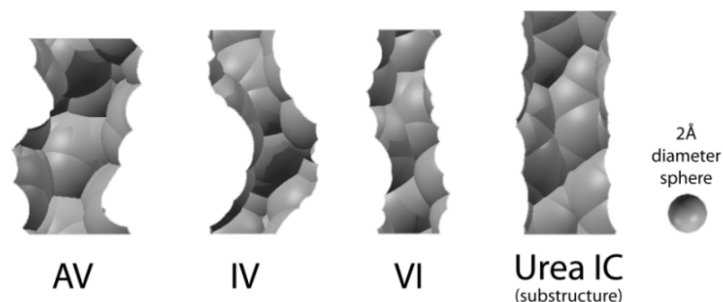
Fig. 67 - Van der Waals empty volumes of AV, IV and VI, compared with the one of urea inclusion compound substructure.

The volumes represent the geometrical *locus* of points described by a rigid sphere having 1 Å radius tangent to the structure atoms, modeled as rigid spheres of appropriate Van der Waals diameter (1.55 Å, 1.52 Å, 1.70 Å and 1.2 Å for N, O, C and H, respectively[90]). Close similarity between AV and urea pore diameter is evident, with AV having a more pronounced twist around the channel six-fold screw axis. IV and VI, on the other hand, have markedly smaller accessible pores. Fig. 67 reports the channel cross sections taken by slicing the pore volumes at 1/60 intervals along the *c* axis. While IV and VI sections don't have any specific dominating axis, AV and urea appear to possess pores with elliptical cross section that undergoes a 60° turn in 1/6 of *c* axis. Indeed, AV and urea areas seem nearly superposable in both shape and size. If cross-section areas (in Å^2) are plotted against absolute displacement along the channel axis, Fig. 68 is obtained, where AV and Urea IC have an almost commensurate modulation and similar areas, unlike IV and VI channels.
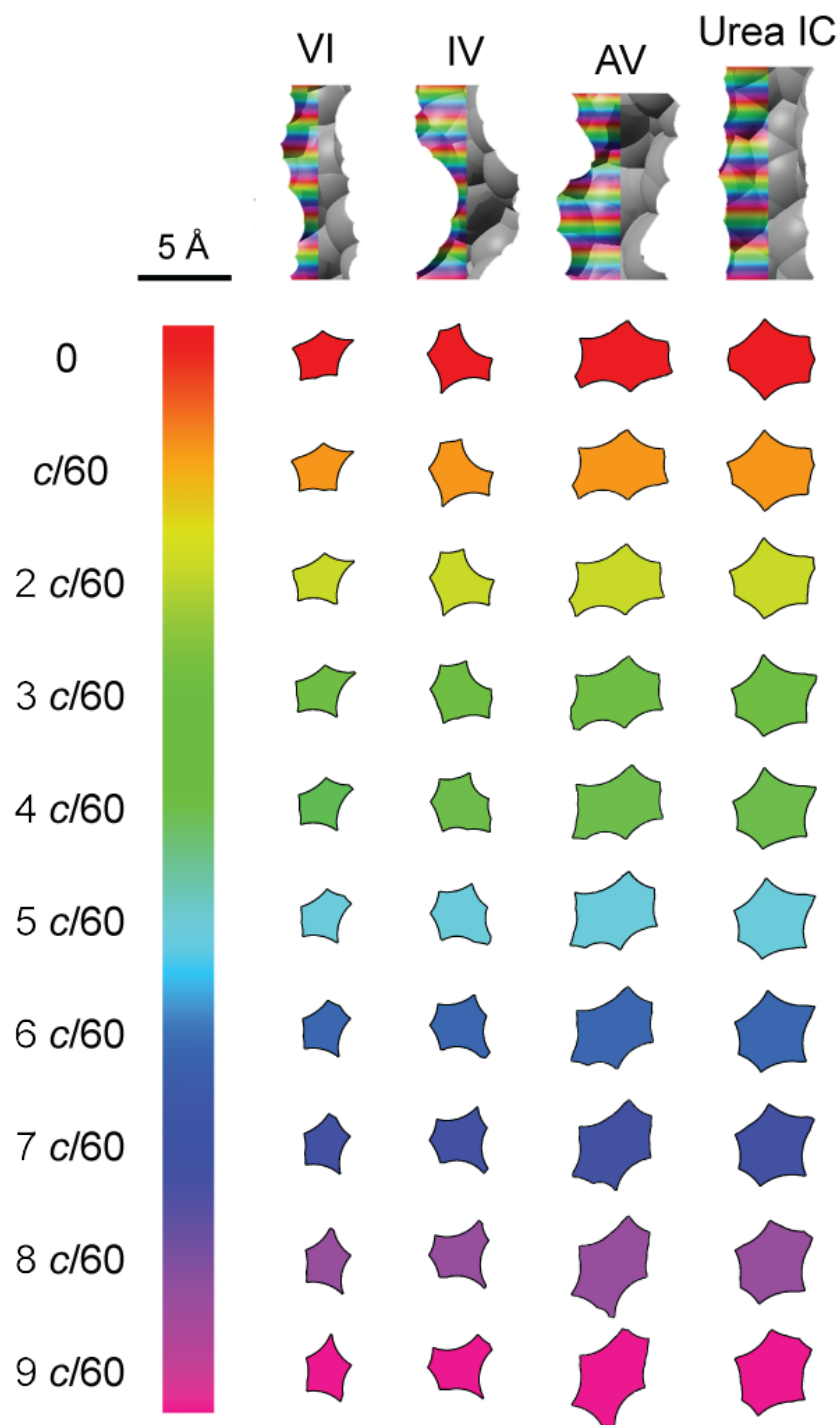
Fig. 68 – AV, IV, VI and Urea IC substructure nanochannel sections sampled at *c*/60 intervals from origin to *c*/6. The sections profile repeats along the remainder of the unit cell because of 6-fold symmetry.
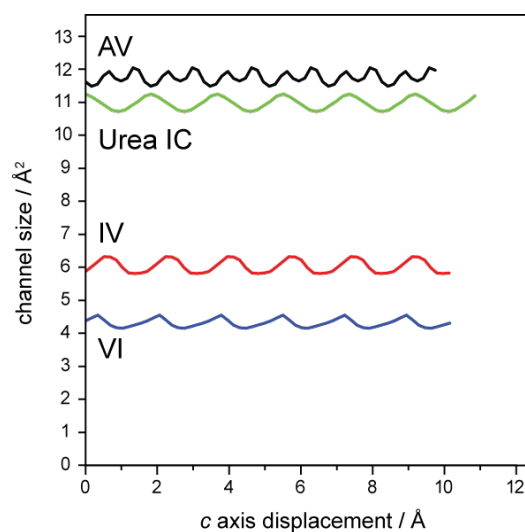
Fig. 69 – Profiles of dipeptides and urea IC substructure sectional areas along *c* axis.

This surprising structural analogy between AV dipeptide and urea IC substructure partly explains why polyacrylonitrile polymerized in AV has an isotactic structure. When stereoregular polymers are formed in nanochannels, structural commensurability between monomer unit repetition length and crystal structure of the nanovessel is invoked to justify stereoregularity: the availability of regularly spaced channel enlargements in correspondence of polymer side groups (*e.g.* the nitrile moiety in polyacrylonitrile) is considered a requirement for stereochemical control. Anyway, even if IV and VI channels appear to have channel modulation similar to urea, smaller pores might introduce chain distortions which prevent the formation of a stereoregular product.

VA is comparable in size with the channels of AV (5.1 Å vs. 5.4 Å, Fig. 69), but helicity is higher, with effects on the channel cross section shape, which is circular rather than elliptical. Acrylonitrile was polymerized in VA according to the usual procedure and the stereochemical regularity of the polymer was examined by ^{13}C NMR. Quite surprisingly, VA polymerized PAN has atactic structure (see Appendix C), similarly to the polymer obtained from IV and VI. It is reasonable to assume that channel size, commensurate modulation with polymer and cross section shape are all concomitant factors in promoting the isotactic product.
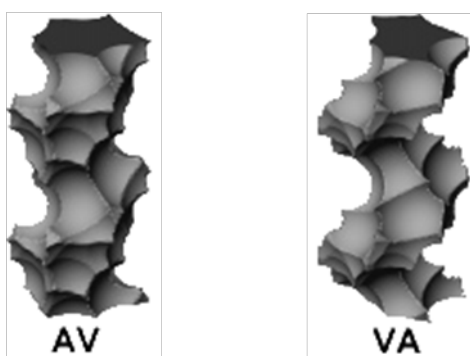
Fig. 70 – AV Van der Waals accessible channel compared to VA.

3.4.3. Characterization of *in situ* polymerized polyisoprene (PI)

3.4.3.1. ^{13}C NMR characterization of polyisoprene

Since *trans*-1,3-pentadiene polymerization produced an 1,4-*trans* polymer devoid of head-to-head or tail-to-tail regiochemical defects, polymerization of isoprene was undertaken with the aim of synthesizing regioregular 1,4-*trans*-polyisoprene, which is produced in high regularity by biosynthesis in plants, using enzymatic paths[91,92]. The ^{13}C NMR spectrum of PI obtained in AV nanochannels is reported in Fig. 70. Two alkene signals are found at 134.9 ppm and 124.2 ppm, while five peaks are found in the aliphatic region, belonging to methylene and methyl carbons.
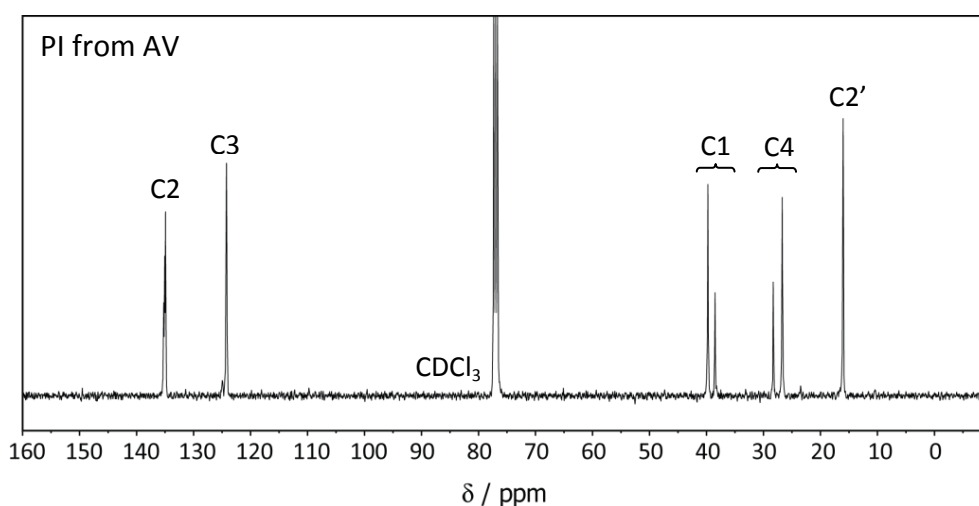
Fig. 71 – ^{13}C NMR (100 MHz, CDCl₃) spectrum of polyisoprene obtained in AV

The two signals in the alkene region assures that we are in presence of a polymer with regular enchainment: only 1,4 connectivity is formed, since 3,4 and 1,2 additions would produce peaks around 110-120 ppm and 140-150 ppm[93] which instead are absent. Informations about the *cis-* or *trans-* stereoisomerism of the polymer double bond is drawn from the methyl resonance at 16.03 ppm which clearly belongs to 1,4-*trans* enchainment [94]. A completely regular polyisoprene is expected to feature only five signals, corresponding to the five carbons of isoprene repeating unit; if peaks are in higher number, they must arise from a more complex microstructure. Given 1,4-*trans* connectivity, additional degrees of freedom may come from regiodefects (namely head-to-head, hh, and tail-to-tail, tt) which cause splitting in sequence-sensitive signals. Indeed, peak intensities of the two signals around 40 ppm and those around 27 ppm (methylenes) sum to one, if integrals are normalized on the methyl carbon. As previously reported for isoprene polymerization in perhydrotriphenylene (PHTP) host-guest systems[95], 1,4-trans-polyisoprene methylene carbons are sensitive to regiodefects at the diad level: in fact, peaks at 39.75 ppm and 38.50 ppm (C1) correspond to ht and hh sequences respectively, while those at 28.39 ppm and 26.72 ppm (C4) belong to tt and ht sequences (Fig. 72). Integrals of the ht in C1 and C4 signals have the same intensity (0.65-0.67 if normalized on CH_3); likewise, tt and hh absorptions integrate to 0.34 as required to ensure chain continuity. Moreover, the signal at 135 ppm (C2) shows fine structure that was interpreted at the triad level[95], with four peaks arising from ht,ht (134.93 ppm), ht,hh (135.06 ppm), tt,ht (135.10 ppm) and tt,hh (135.24 ppm) sequences (Fig. 71 and Fig. 73).
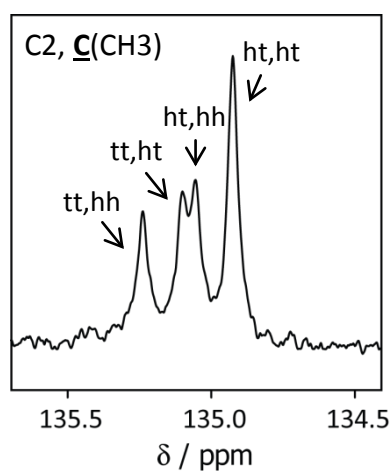
Fig. 72 – Expansion of the C2 signal of AV polymerized PI, evidencing fine structure sensitive to triad regio-sequences.

Table 9 – ^{13}C NMR assignments of 1,4-*trans*-polyisoprene obtained in AV

label	^{13}C	sequence	δ / ppm	Integral	
			PI from AV		
C1	**C**H$_2$	ht	39.75	0.91	0.67
		hh	38.50		0.33
C2	**C**(CH$_3$)=	tt,hh	135.24	1.00	0.21
		tt,ht	135.10		0.19
		ht,hh	135.06		0.20
		ht,ht	134.93		0.39
C3	=**C**H	/	124.21	0.95	
C4	**C**H$_2$	tt	28.29	0.94	0.34
		ht	26.72		0.66
C2'	**C**H$_3$	/	16.03	1.00	

The probability of encountering a regioregular sequence (ht or th) is the integral of the respective carbon signal and in case of PI polymerized in AV dipeptide, is P_{ht} = 66-67%. Head-to-head or tail-to-tail defect corresponds to half the intensity of each methylene hh or tt signal, since each defect generates two isochronous carbons (Fig. 72): hh and tt probabilities are therefore P_{hh} = P_{tt} = 16-17%. Furthermore, the distribution of connectivity defects can be evaluated from the C2 signal fine splitting. The internal ratio among defective triads (Table 9) is 1:1:1, indicating that tt,hh tt,ht and ht,hh situations have the same probability to occur. Such a situation is verified for the case of isolated hh,tt (or tt,hh) defects, corresponding to the antiparallel addition of a single monomer unit along the chain (Fig. 74). In the heptad sequence shown in Fig. 74, the probability of having a ht diads is exactly P_{ht} = 2/3 (~66.7%), while P_{hh} and P_{tt} correspond to 1/6 (~16.7%). Triad probabilities, on the other hand, are $P_{ht,ht}$= 2/5 (40%) and 1/5 (20%) for defectual sequences. These calculated probabilities are close to the experimental

ones of 1,4-*trans*-polyisoprene from AV nanochannels and suggest a microstructure which presents, on average, six direct monomer addition every inverted one.
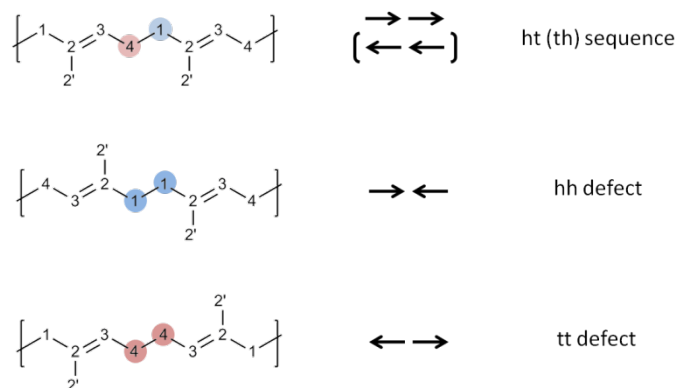
Fig. 73 – Regiochemical sequences in 1,4-*trans*-polyisoprene (diad level).
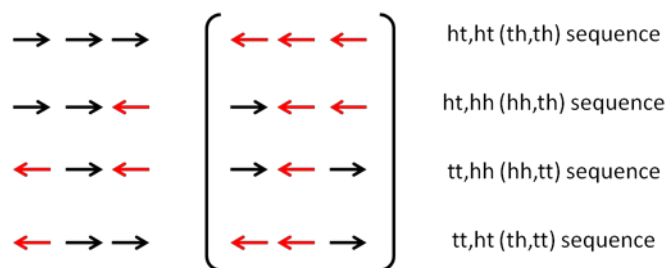
Fig. 74 – Regiochemical sequences in 1,4-*trans*-polyisoprene (triad level). Specular situations generate equivalent[13]C NMR signals.
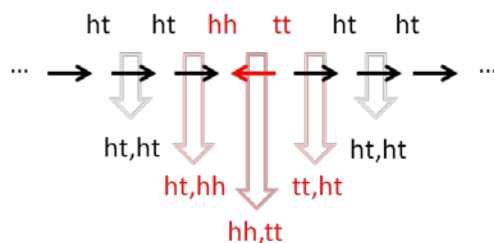
Fig. 75 – Diad and triad sequences generated from an isolated antiparallel enchainment.

Microstructure is a slightly different in 1,4-*trans*-polyisoprene prepared in VA nanochannels: C2 signal splitting still shows four peaks assigned to triad sequences but the relative intensity of ht,hh and tt,ht sequences ($P_{ht,hh} = P_{tt,ht} = 14\%$) is decreased with respect to hh,tt sequences ($P_{hh,tt} = 20\%$) while regioregular enchainment appears to be more abundant ($P_{ht,ht} = 52\%$). Relative increase in the ht,ht sequence means that the polymer is more regular than polyisoprene from AV. On the other hand, the decrease of ht,hh and tt,ht triads suggests that a certain number of enchainment occur in an alternated fashion (Fig. 76).
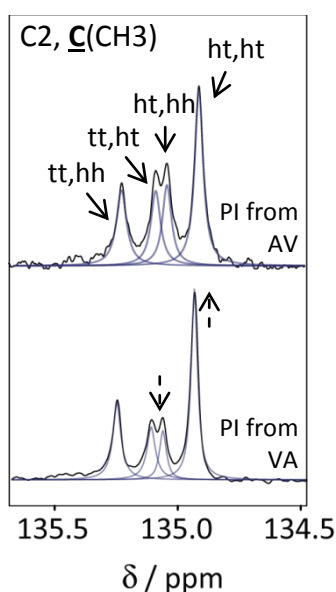
Fig. 76 – Comparison of ^{13}C NMR C2 signals in PI polymerized in AV (top) and VA (bottom).
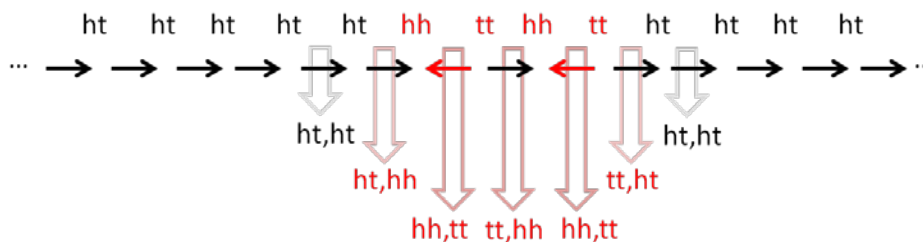
Fig. 77 – Diad and triad -sequences arising from alternated direct and inverse additions.
Compared to the isolated case (Fig. 74), ht,hh and tt,ht sequences have lower statistical weight with respect to hh,tt (tt,hh) triads.

3.5. Conclusions

In this chapter, nanoporous dipeptides were employed successfully as selective nanovessels in radical polyaddition reactions. Dipeptides (AV, IV and retroanalogues) proved structurally stable during nanocomposite preparation which consisted in potentially damaging *stimuli* (exposition to hydrocarbon vapors, γ-ray irradiation, *in situ* polymerization), demonstrating the remarkable strength of the nanoporous architecture, despite being generated by an organic molecular crystal. The confined environment of the nanochannels is suitable for the promotion of microstructural control over the produced polymers: propagating free radicals are compelled to react in compliance with the available pore space, producing polymers that can be generally obtained by catalytic strategies or by enzymes in nature.

Acrylonitrile polymerization proceeded successfully in AV, VA, IV and VI, yielding isotactic polyacrylonitrile in one case (AV, where a polymer with *mm* triad content of 59% was produced) and atactic polymers in the other. This result is relevant because highly isotactic polyacrylonitrile can't be obtained by conventional Ziegler-Natta catalysis. Pore geometry demonstrated crucial in producing a stereoregular product since minor changes in the channel morphology is detrimental towards the favorable host-guest tuning demonstrated by AV nanochannel (combination of pore size and pore shape). In addition, polymerization of conjugated dienes was investigated because of their ability to generate a large number of mixed microstructures during uncontrolled radical polymerization and to provide nanospace information encoded in the final polymer structure. *trans*-1,3-pentadiene was polymerized in AV, IV and VI dipeptides producing in all cases atactic 1,4-*trans*-polypentadiene without regiochemical defects. Similarly, isoprene polymerization in AV and VA nanochannels produced 1,4-*trans*-polyisoprene with regiochemical defects (head-to-head and tail-to-tail). In both cases linear polymer structure was selected, demonstrating that polymerization occurred *in situ*.

As shown with acrylonitrile polymerization, subtle modifications of the channel space (caused by change in dipeptide "sequence") are capable of influencing greatly the final polymer stereochemistry: this evidence is reminiscent of the specificity of enzyme proteins, where mutations (namely punctual changes of the protein's amino acid sequence) can cause a discrete, non-continuous change in the enzyme activity due to modification of the geometry of the active site. On the other hand, it is known that enzymes can also tolerate mutations without losing their activity, as in the case of diene polymerizations that yield polymers with

similar structure regardless of dipeptide "sequence". This analogy can be further investigated with the involvement of other vinyl or diene monomers (change of "substrate") and/or new porogenic dipeptides (like L-valyl-L-valine, L-isoleucyl-L-alanine, L-alanyl-L-isoleucine together with porous dipeptides of the phenylalanyl-phenylalanine class, see Chapter 1).

Finally, as polymer recovery consists in simply dissolving the matrix in water and since the dipeptide isn't damaged during the whole process, the nanoporous matrix can be recovered easily and regenerated by mere recrystallization. Such versatility, combined with the intrinsically biodegradability of peptide materials, make nanoporous dipeptides ideal candidates for green chemistry applications.

Chapter 4 – From dipeptides to carbon fibrils

4.1. Beyond microstructure: manipulation of polymer morphology and anisotropy

In Chapter 3 it was demonstrated how nanoporous dipeptides are effective in hosting vinyl or dienic monomers that are then able to polymerize, generating polymers having microstructures otherwise impossible to obtain with plain radical polymerizations. *In situ* polymerization forms nanocomposites consisting in the nanoporous dipeptide matrix containing isolated polymer chains in its channels. The macromolecules are accommodated in parallel fashion, in elongated conformations. Such pre-organization of the polymer guest was exploited with the aim of obtaining microscopic polymer objects which retain both morphological and molecular anisotropy.

Polymeric microparticles have attracted great interest for many technological applications. Water dispersions of spherical particles are commonly used for the protection of metal, wood and leather from water and microorganism, as binders for pigments, fillers and fibers and to

finish the surfaces of metal, wood or paper[96]. More advanced applications, such as analysis, photonics, diagnostics and tissue engineering, require the precise control of the microparticles' morphology since it is critical to the final technological function. Control over particle shape and size, monodispersity, surface chemistry and porosity are thus becoming increasingly stringent[97]. For instance, in drug delivery applications, particle shape is expected to affect the carrier's performance greatly, by influencing the degradation, transport, targeting and internalization behavior of each individual micrometric object[98], but the lack of preparation methods that can provide varied shapes has brought scientists to focus mainly on spherical particles[99].

One of the viable methods to fabricate non-spherical polymer objects is the one of shape-replica. In this approach, a porous template having a well defined shape is used as a scaffold for *in situ* polymerization of an imbibed monomer. After polymerization and scaffold degradation, the polymer holds the shape of the starting porous object. This strategy has been used in the past by our group to produce polystyrene and polymethylmethacrylate micro-objects with controlled and well defined shapes, starting from mesoporous silica solids of revolution[100]. This approach has been employed in the present case, with the aim of obtaining fibrillar object reminiscent of dipeptide crystal shape.

4.1.1. Polyacrylonitrile fibrils by matrix dissolution

In the previous chapter dipeptide⊃PAN nanocomposites were treated with distilled water to dismantle the dipeptide matrix and free the native polymer. Analytical characterizations (XRPD, DSC, NMR) demonstrated that the obtained insoluble product was pure polyacrylonitrile.

In order to witness the generation of the free polymer and its morphology, the phenomenon was examined *in situ* using an optical microscope. First, the dissolution of dipeptide crystals was observed for reference: a drop of a suspension of AV dipeptide in non-solvent (ethanol or dimethyl sulphoxide) was put on a microscope slide and covered with a cover slip. Then, after choosing and focusing on a crystalline specimen (dipeptide crystals are transparent hexagonal needles) a drop of distilled water is added beside the cover slip and let diffuse and mix with the non-solvent (Fig. 77).
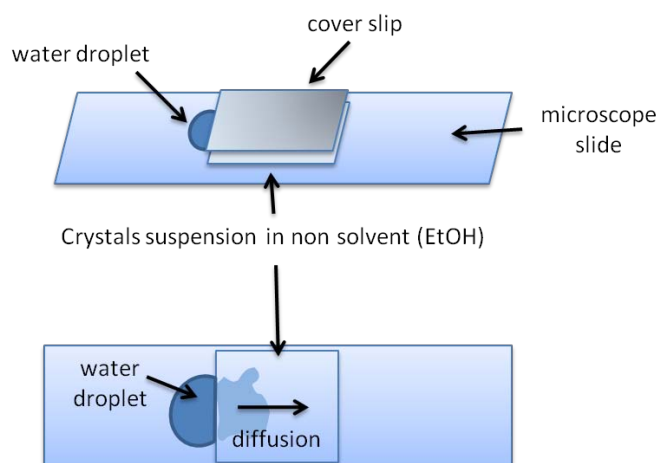
Fig. 78 – Geometry for *in situ* observation of dipeptide dissolution

In this way, dipeptide crystals come gradually in contact with water and, if turbulent flows are avoided by gentle water addition, sitting crystals are progressively eroded by the incoming solvent. For instance in Fig. 78 from a) to d) (left column) it is possible to see the dissolution of a group of AV crystals by water. Instead, as shown in Fig. 78 (a' to d'), when a group of AV⊃PAN nanocomposite crystals are dissolved, insoluble native PAN fibrils appear. Molecular anisotropy of PAN chains is suggested by longitudinal wrinkles on the fibril surfaces: in fact, nanochannels, and therefore polymer chains, develop parallel to the main axis of the crystals. Polyacrylonitrile fibrils tend to bend due to capillary forces arising at the boundary between solution and fibrils themselves; polymeric objects are not stiff and, as they are recovered by means of filtration, form agglomerates of tiny polymeric ribbons. Fig. 79 shows some representative scanning electron micrographs of PAN fibrils recovered from AV⊃PAN nanocomposite. The removal of the dipeptide scaffold leads to the coalescence of the polymer chains which aren't isolated from each other anymore. Macromolecular chains coagulate and collapse together, determining the corrugation of the polymeric fibrils during this abrupt phenomenon (Fig. 79-c,e). In fact, polyacrylonitrile molecules in the nanocomposite have an interchain distance imposed by the dipeptide crystal structure (14.5 Å) which is reduced to the Van der Waals close contact (about 6 Å) after matrix removal. Chain separation is therefore more than halved during the process. Instead, no appreciable longitudinal contraction is observed.
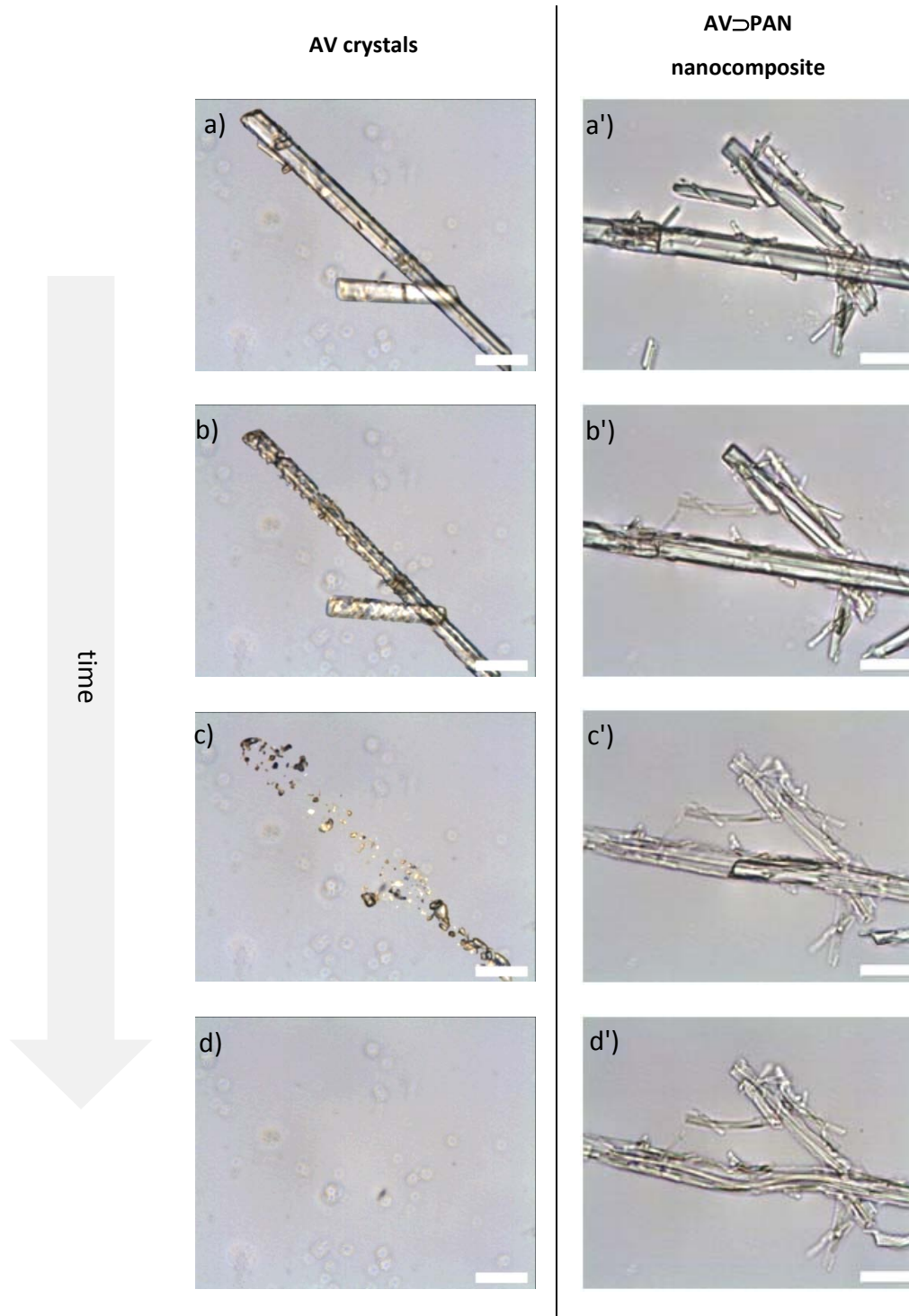
Fig. 79 – Timelapse (total time: 2 min) optical micrographs if dissolution of a group of AV (from a to d, left) and AV⊃PAN nanocomposite crystals (from a' to d', right). Scale bars equal 20 μm
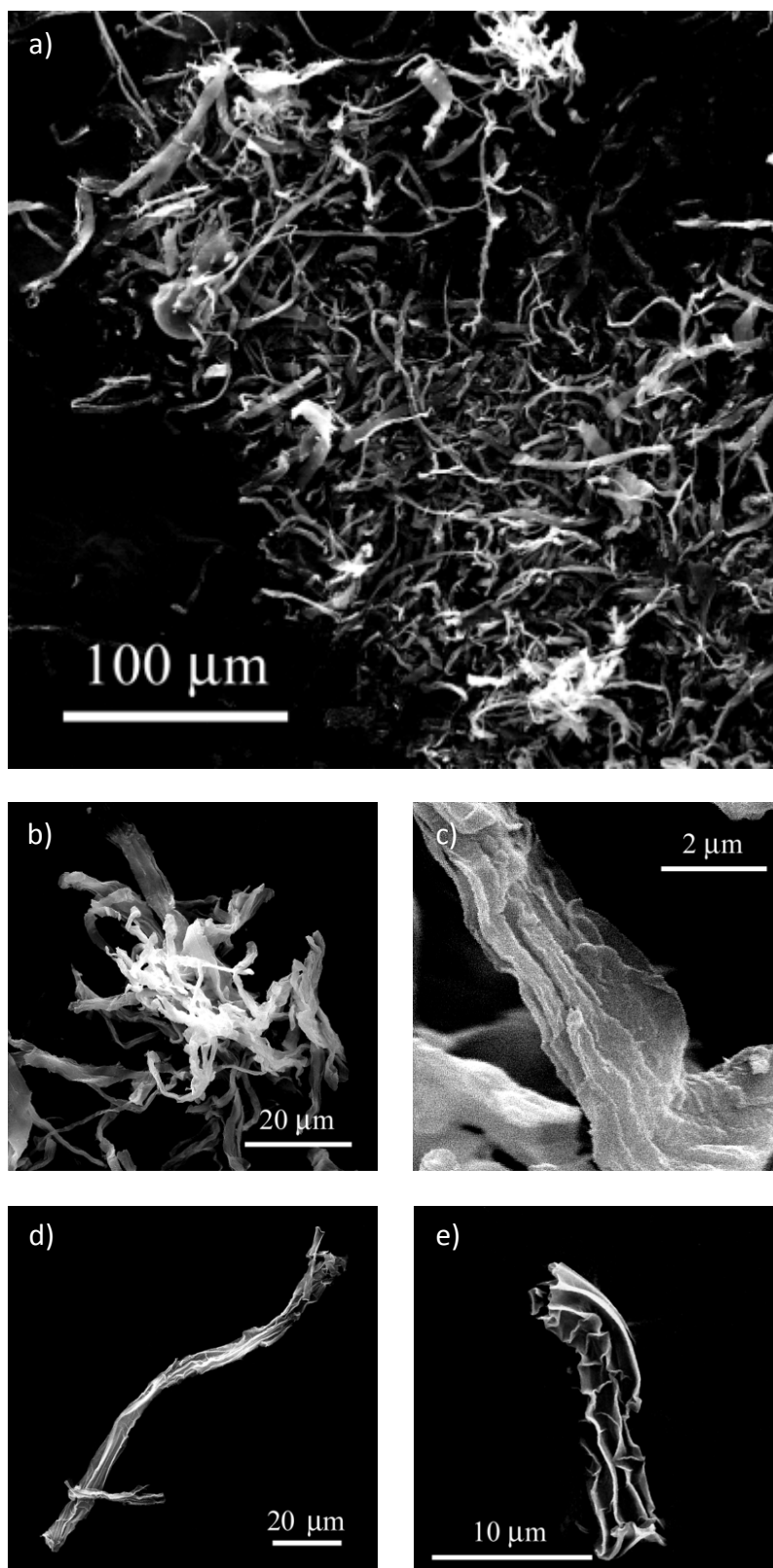
Fig. 80 – SEM images of native PAN fibrils obtained from AV⊃PAN nanocomposite dissolution

Size distribution of the polymer fibrils depends on size distribution of starting nanocomposites: granulometric selection of AV crystals prior to polymerization could offer a way to produce polymeric microfibers with controlled length.
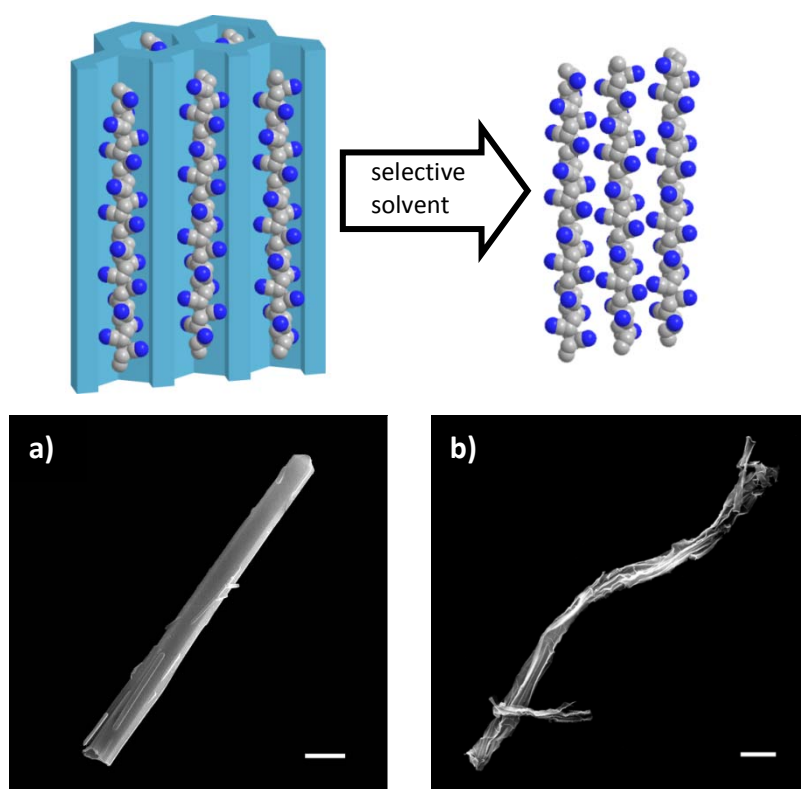
Fig. 81 – Schematic representation of the transformation from nanocomposite a) to free polymer b). Coalescence between polymer chains cause the bending and the appearance of wrinkles on the polymer fibril surface

4.1.2. Ladder PAN polymer rods by matrix sublimation

TGA analysis on AV⊃PAN (Chapter 3) reveals that matrix can also be removed by selective sublimation/degradation. In fact, if the nanocomposite is treated *in vacuo* for 2 hours at 300°C, the macromolecular guest is freed without the need of solvents. SEM micrographs (Fig. 81-b) show that, unlike matrix dissolution, polymeric material appears stiffer since nanocomposite crystals are converted into straight rods rather than bent ribbons.

The apparent macroscopic volume of the treated sample isn't changed during heating, but mass changes accordingly, becoming rougly one tenth and a change in color can be evidenced, too. In fact, around 250°C during heating, the nanocomposite turns yellow and becomes

progressively darker as temperature is increased, assuming a dark orange colour after 2 hours at 300°C. Development of coloration is associated to the well known thermal cyclization/aromatization of polyacrylonitrile, occurring at about 270°C, which produces a ladder polymer by means of nitrile groups polymerization[101,102]. DSC check demonstrates the complete removal of the matrix.
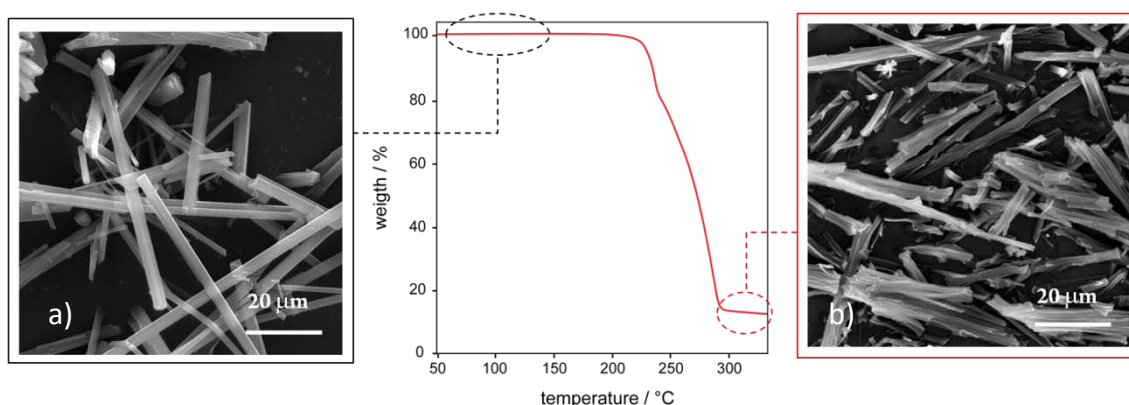
Fig. 82 – TGA profile of AV⊃PAN nanocomposite and SEM images of the pristine (a) and thermally treated (b, 300°C *in vacuo*, for 2 hours) sample.

The sublimation method avoids phase boundaries and capillary forces that cause the polymer particle to bend and deform, producing more faithful replicas of the crystalline precursor. On the other hand, ladder polyacrylonitrile is intrinsically more rigid than the original polymer, preventing the polymeric rods from entangling. Brittleness of the ladder PAN objects is suggested by SEM images where fractured particles can be occasionally recognized (Fig. 81-b, lower left corner).

In this way, a nanochemical manipulation is realized, since PAN chains are assisted by the sacrificial nanoporous matrix and kept in elongated fashion during intramolecular cyclization.

4.1.3. Carbon fibrils by ladder PAN pyrolysis

Further heat treatment of the ladder PAN up to 1100°C (argon atmosphere, heating rate: 2°C/min, final temperature held for 3 hours), cause the transformation of the stabilized PAN rods into carbon fibrils. In fact, PAN is a widely used precursor for carbon fiber production

because of its high carbon yield, convenient processability and good mechanical properties of the final fibers[103]. Graphitic structures develop as polymer chains transform into ladder polymer first and then condensate laterally with the elimination of nitrogen and hydrogen by means of volatile species (*e.g.* H_2, NH_3, N_2 and HCN)[104].

In Fig. 83 the obtained carbon fibrils are compared to both nanocomposite crystals and ladder polymer sticks. SEM imaging does not require metallization of the sample since carbon fibrils are electrically conductive. Moreover, the carbonized sample shows a translucent appearance under the electron beam (Fig. 83-I) which suggest low density of the obtained structures.

Energy Dispersive X-ray (EDX) spectroscopy microanalysis (Fig. 82) on the pyrolized fibrils demonstrate that thermal treatment leads to a carbon material (96% at.) containing only 4% at. oxygen, associated to spontaneous oxidation of graphitic structures in atmosphere, while nitrogen is absent, meaning that extensive aromatization has occurred even at relatively low temperatures.
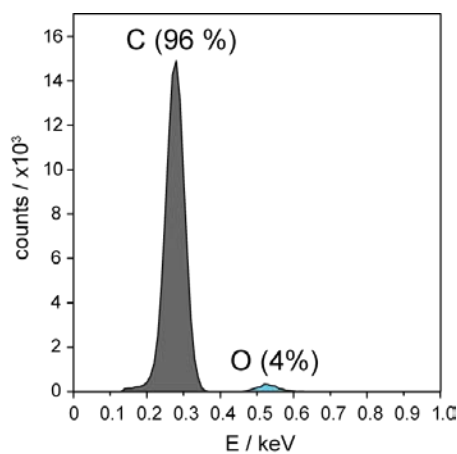
Fig. 83 – EDX spectrum of carbonized PAN fibrils (microanalysis).

AV⊃PAN nanocomposite	Ladder PAN freed by matrix sublimation	Carbonized fibrils
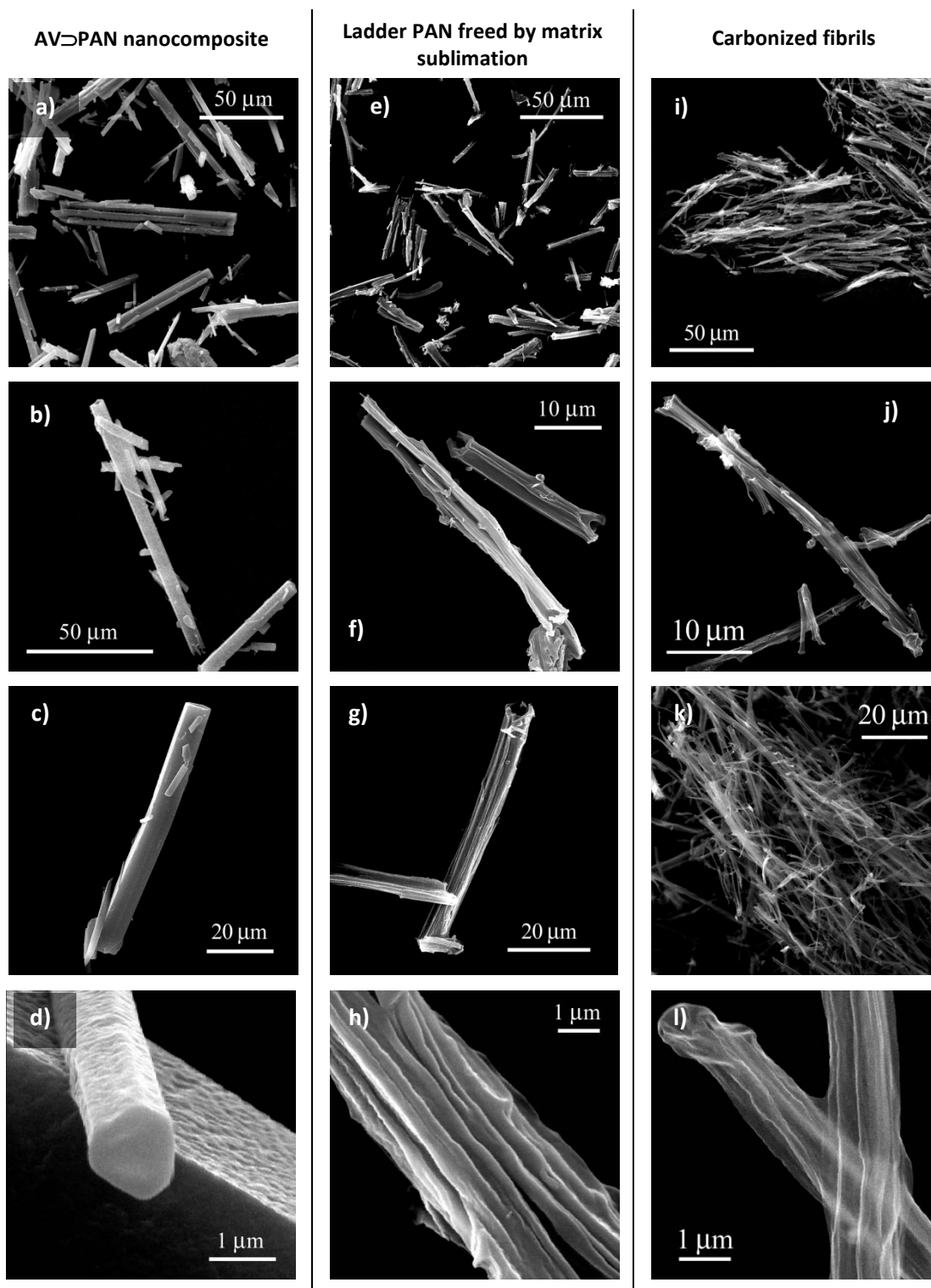
Fig. 84 – SEM micrographs of AV⊃PAN nanocomposite crystals (a to d, left), ladder PAN (e to h, center) and carbonized fibrils

4.1.4. Statistical evaluation of microparticles size

Statistical analysis was performed to rationalize the morphological changes happening in the transformation from dipeptide to carbon fibrils. SEM micrographs were recorded for each sample and micrometer sized objects were measured in length and thickness. As expected, no changes are evident in the passage from porous AV to the nanocomposite with polyacrylonitrile. In fact, unit cell enlargement (see Chapter 3), which should be reflected in an increase in crystal thickness, is too small to be appreciated by SEM (Fig. 84, a and b). Instead, thickness decreases steadily from nanocomposite to ladder polymer to carbonized fibrils with average values going from 3.1±1.9 μm (AV and AV⊃PAN) to 1.6±0.9 μm (carbon fibrils).
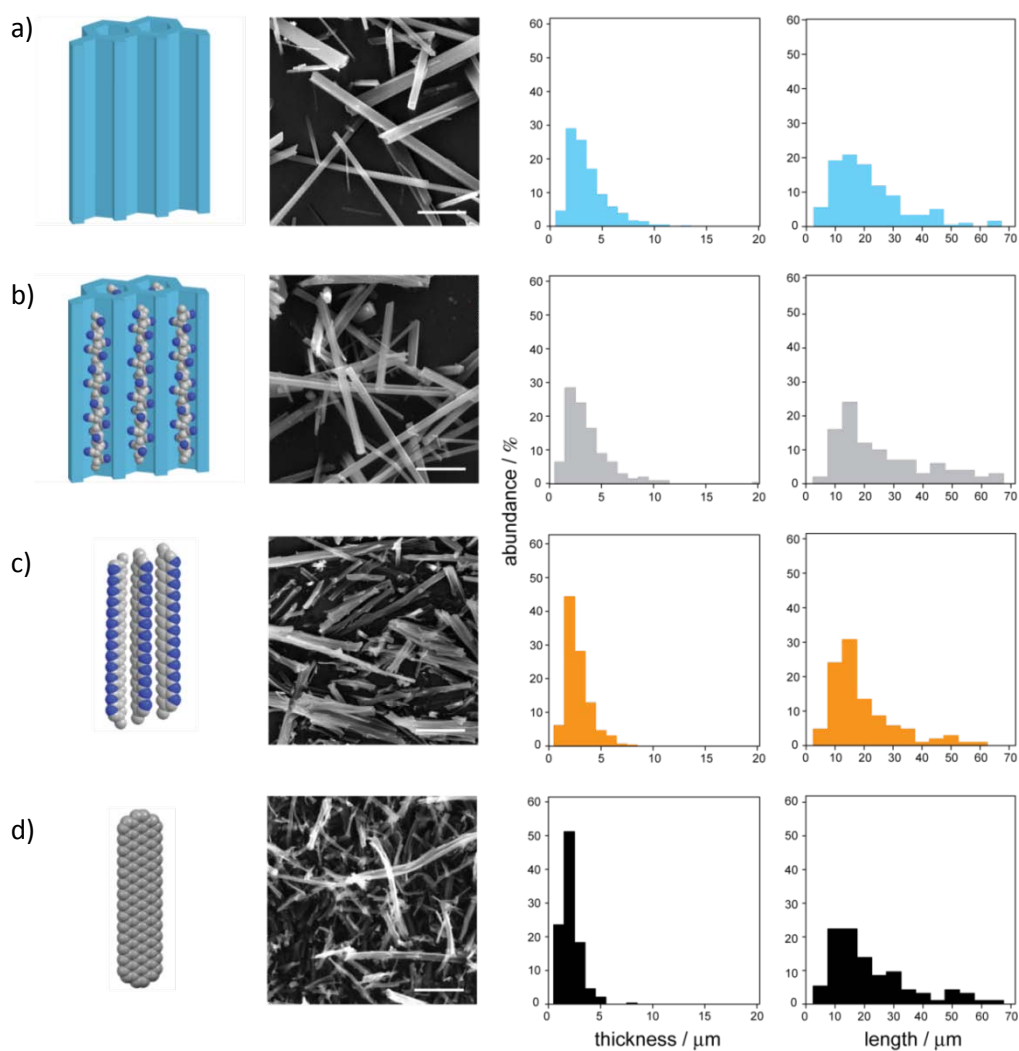
Fig. 85 – Statistical analysis of the size of AV (a), AV⊃PAN (b), ladder polymer (c) and graphitized fibrils (d).

Since pore wall removal (AV⊃PAN to ladder PAN) and lateral condensation (ladder PAN to carbon fibrils) affect the polymer backbone interchain distance, rather than their length, no effect is expected on the distribution of length of the micrometric objects: indeed, length distributions are left substantially unchanged.

4.1.5. Molecular anisotropy in carbon fibrils

The mechanical properties of a carbon fiber depend on the extension and orientation of the graphitic structures with respect to the stress experienced by the fiber itself. It is desirable that graphite sheets develop parallel to the fiber axis rather than perpendicular. In fact, PAN fibers are stretched and kept under a load during heat treatment to favor the correct growth and final orientation of graphite domains. Manipulation of polyacrylonitrile chains by means of nanochannels can be an alternative way of obtaining such anisotropy, where chains are placed in an exactly parallel fashion by bottom-up incarceration rather than macroscopic drawing.
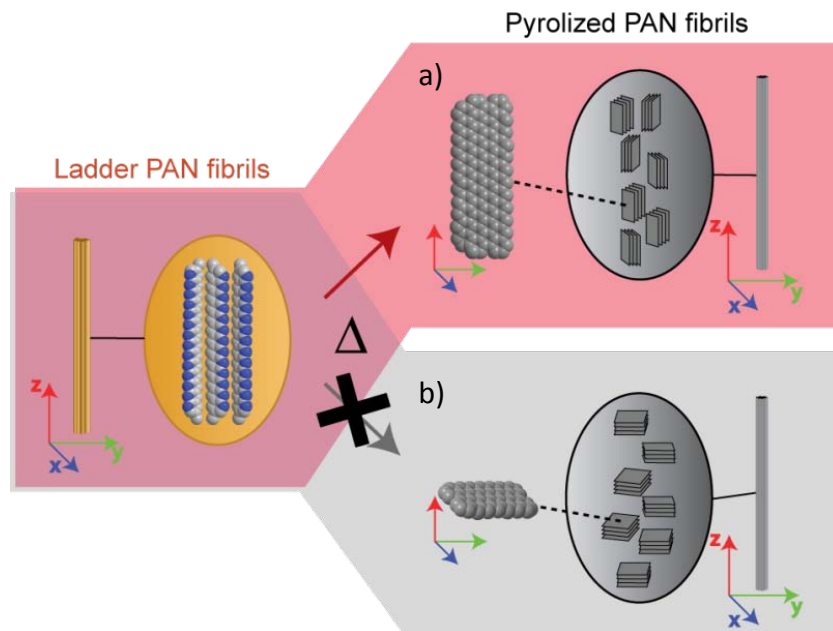
Fig. 86 – Ladder PAN to graphitic material transformation scheme. Precursor polymer chains, aligned by dipeptide porous architecture, generate graphite sheets by lateral condensation at high temperature. Therefore, graphitic planes are expected to develop parallel to the fibril axis *z* (a), with statistical orientations in x and y. Instead, perpendicular orientation of graphite planes with respect to *z* should be forbidden (b)

Fig. 85 shows the foreseen mechanism of graphitization for ladder PAN. Since polymer chains inherit alignment from dipeptide matrix whose channels run along the longer dimension of the crystals, growth of the graphite domains should follow the path pictured in Fig. 85-a with graphite planes developing parallel to the main axis of the fibrils, rather than perpendicular to it. This hypothesis was investigated by polarized micro-Raman (μRaman) spectroscopy on the carbonized fibrils.

Raman spectra of polycrystalline graphite in the range investigated (1000 to 2000 cm^{-1}) consist in two main bands located at 1575 cm^{-1} and 1355 cm^{-1} and referenced as G and D bands respectively[105]. While the G band is the characteristic and sole feature of highly ordered monocrystalline graphite (assigned to the E_{2g} species of the infinite crystal), the D band is associated to graphite crystal boundaries and its appearance depends on the reduction in size of crystallites that makes the A_{1g} mode Raman active[105]. It is well known that the Raman response of crystalline graphite is dependent on polarization of the incident beam with respect to graphite planes: in fact Raman scattering can be up to four time higher when polarization is parallel compared to perpendicular orientation[106]. This relationship can be used to probe the orientation of graphite domains in carbon materials as was done recently with graphitic foams[107].

Fig. 86 shows the comparison between μRaman spectra recorded on the same carbon fibril with different experimental geometries. It can be seen that when laser beam has linear polarization parallel to the fibril axis (Fig. 86-a) the Raman response is up to 40% more intense than in perpendicular arrangement (Fig. 86-b), giving confirmation of orientational anisotropy of the graphitic crystallites in the carbonized sample.

Finally, internal ratios of the G and D bands can be correlated to the graphite crystal size in the direction of graphitic planes (L_a) through the generalized Tuinstra-Koenig equation[108]: the calculated L_a value corresponds to 5.0 nm and is obviously independent from the geometry of the Raman experiment.
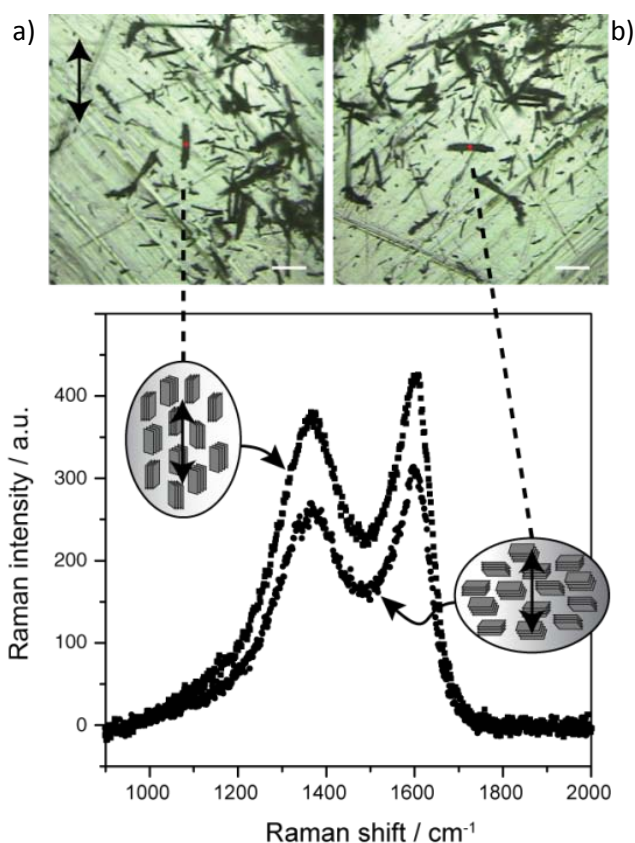
Fig. 87 — Polarized Raman spectra of carbonized AV PAN. Observed intensity of the main Raman-active bands is up to 40% higher for incident laser polarization parallel to the carbonized fibril's axis than for perpendicular configuration. Microscope images of the examined fibril are reported for completeness: the red spots indicate the point of laser incidence in both parallel (a) and perpendicular (b) configurations. Scale bars equal 20 μm.

Table 10 – Polarized μRaman spectroscopy summary table

	X(Z,Z+Y)-X configuration (parallel)	X(Y,Z+Y)-X configuration (perpendicular)
Integrated intensity / a.u.	143.0	100.0
G band intensity / a.u.	24.7	17.9
D band intensity / a.u.	66.6	48.0
L_a / nm	5.0	5.0

4.2. Conclusions

In this chapter, AV dipeptide was used to manipulate guest polymer molecules on both the nano- and microscales. AV dipeptide is able to host acrylonitrile monomers which can be polymerized to produce a macromolecular guest (Chapter 3). In the AV⊃PAN nanocomposite, polymer chains are individually isolated in nanochannels and peptide matrix imparts anisotropic arrangement to the guest molecules thanks to its crystalline order.

Removal of the dipeptide by a selective solvent attained microscopic polyacrylonitrile objects having characteristic aspect ratio (fibrils), inherited from the dipeptide needle-shaped crystallites. Furthermore, removal of AV by selective matrix sublimation and subsequent pyrolysis of polyacrylonitrile guest, lead to the formation of carbon micro-fibrils. Thus, microscale manipulation of polymeric material was obtained by AV crystals, which act as sacrificial microscopic "molds".

Moreover, nanoscale anisotropy of the polymer chains arrangement was revealed by the surface texture of polymer fibrils (wrinkles) and their differential shrinking in the lateral dimension with respect to the *pristine* nanocomposite. Alignment of polyacrylonitrile chains was transferred to the pyrolyzed fibrils where graphite nanocrystals possess preferential alignment parallel to the fibril axis.

In conclusion, dipeptide crystal shape and molecular anisotropy of nanocavities can be imprinted to macromolecular guests: this result might disclose new strategies for the bottom-up fabrication of functional polymers with anisotropic properties (mechanical, electric, optical or thermotropic).

Chapter 5 – Dipeptide thermal cyclizations

5.1. Thermal properties of ʟ-isoleucyl-ʟ-valine dipeptide

Aliphatic dipeptide ʟ-isoleucyl-ʟ-valine (IV), as the other nanoporous dipeptides of the VA series, shows remarkable thermal stability. As reported in the literature, amino acids and short peptides are characterized by zwitterionic molecular structures in the solid state where COO^- and NH_3^+ moieties participate in charge-assisted hydrogen bond networks that confer stability to the material. In fact, solid peptides and amino acids tend to decompose prior to melting as a consequence of the intermolecular interactions of their crystalline phases[109]. Thermal properties of materials for practical use deserve deep characterization in order to assess their viability in various environments and their durability. In this regard, investigation on the thermal stability of IV disclosed unexpected behavior which could be generalized to other dipeptides of the series.

5.1.1. DSC characterization

DSC thermogram of IV ($10°C$ min^{-1} heating rate, N_2 atmosphere) is reported in Fig. 87: notwithstanding its relatively low molecular weight and organic nature, no thermal

transformation occurs up to 200°C. Above 200°C, three endothermic phenomena are videnced: the first transition produces a sharp peak at 201°C with enthalpy of 57.3 kJ mol^{-1}, while at higher temperatures a broad phenomenon having onset at 250°C is superposed to sharp peak at 315°C. Visual inspection in a melting point apparatus evidences that the transformation at 200°C is not associated to the melting of IV, while those at higher temperature are accompanied by melting/sublimation and darkening of the analyte. Instead, the appearance of the solid compound doesn't change across the first endothermal phenomenon.
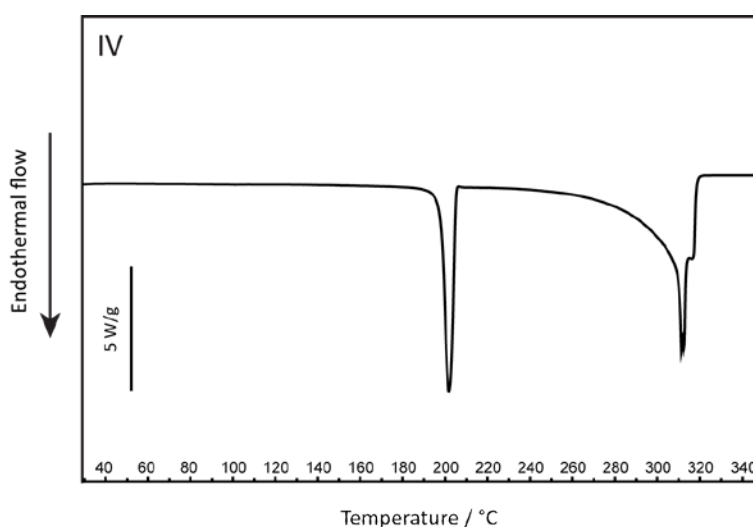
Fig. 88 – DSC thermogram of IV dipeptide

Melting is ruled out also because no crystallization exotherm is evidenced upon cooling from above 200°C (Fig. 88). Moreover, if IV dipeptide is thermally treated above 200°C in an oven (210°C for 1h under N_2 atmosphere) and DSC is performed, the thermogram appears similar to the untreated dipeptide but the first transition disappears (Fig. 89).

Chemical transformation of IV dipeptide upon heating is suggested also by change in solubility of the thermally treated compound: *pristine* IV is water soluble while it becomes hydrophobic after treatment but still being soluble in polar solvent such as dimethyl sulphoxide and methanol. Dipeptides owe their water solubility to the possibility of interacting with water through hydrogen bonds: change in such ability can be associated to a change of molecular structure involving the C and N termini of the dipeptide.
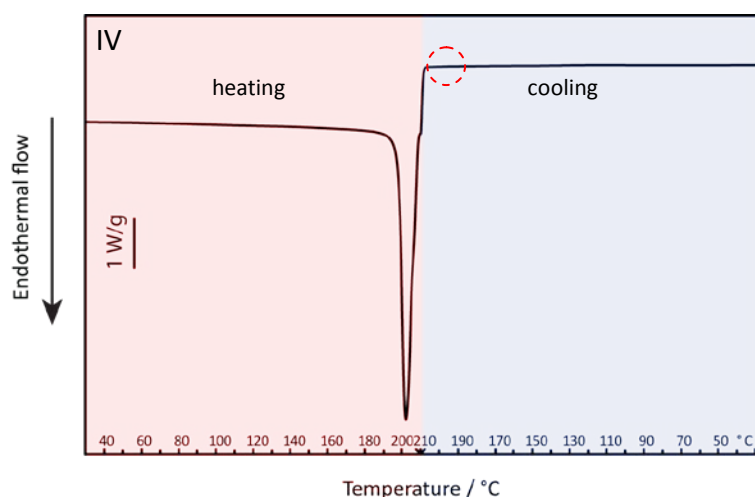
Fig. 89 – Irreversibility of the first transitino of IV. IV is heated up to 210°C and then cooled to room temperature (10°C min^{-1}). Lack of exotherm during cooling ramp rules out melting of dipeptide at 200°C.
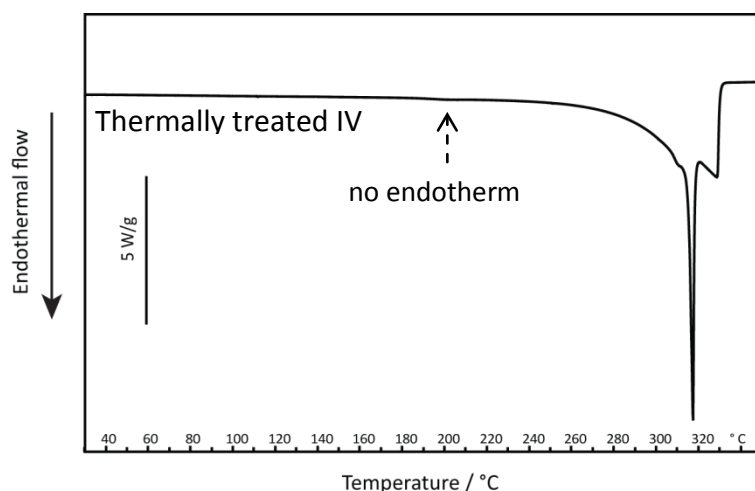
Fig. 90 – DSC thermogram of IV treated at 210°C in N$_2$ atmosphere for 1 hour. Endothermal transition at 200°C is absent.

5.1.2. TGA-mass spectroscopy (TGA-MS) characterization

TGA analysis on IV dipeptide shows that a sharp weight loss happens, accounting for about 8.6% wt decrease around 200°C. Weight loss occurs in a small temperature range (20°C) and has midpoint at 203°C. Quantitative weight loss at higher temperature is associated with complete degradation/volatilization of the dipeptide. Mass spectroscopy shows that water is evolved at the same time as the first transition (Fig. 91, 18 and 17 Da corresponding to H$_2$O and OH$^-$ fragments), while decarboxylation is excluded (no change in the baseline of the 44 Da channel). Moisture or water adsorbed in the nanochannels would be released well below

200°C, so water produced at higher temperature is likely to arise from a chemical reaction occurring in the compound. This result together with irreversibility of the phenomenon is a hint of chemical transformation involving condensation. Indeed, if a water molecule (18.02 Da) was lost for each dipeptide molecule (230.31 Da) a 7.8% weight loss, close to the experimental value, would be produced.
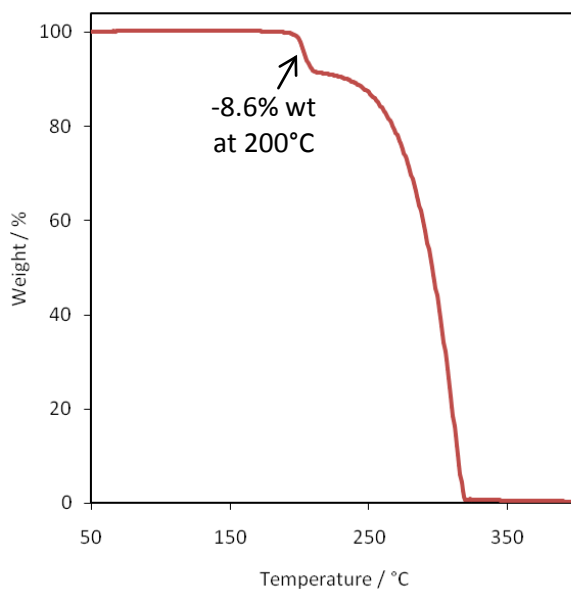
Fig. 91 – TGA thermogram of IV dipeptide
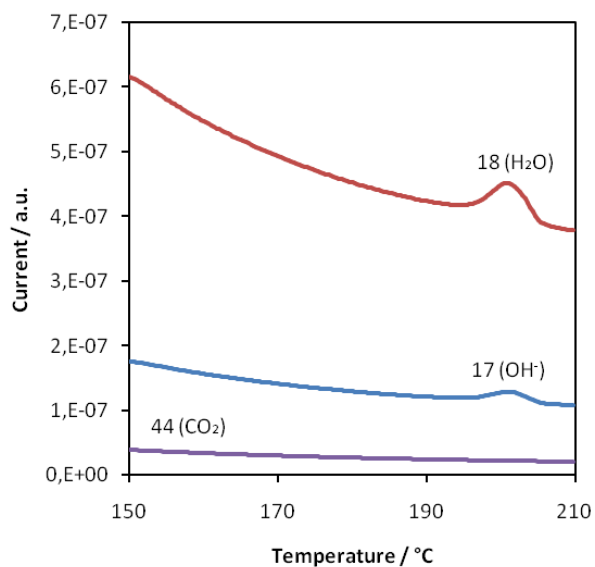
Fig. 92 – Evolution of H$_2$O and OH$^-$ fragments concomitant with thermal transformation at 200°C for IV (channels corresponding to 17, 18 and 44 Da depicted vs. temperature)

5.1.3. Infra-red (IR) spectroscopy

Occurrence of a condensation reaction in the compound at high temperature was investigated through IR spectroscopy. In fact, attenuated total reflection (ATR) infra-red spectroscopy on powders of the thermally treated dipeptide shows a simplification of the spectrum in the region between 1500 and 1650 cm^{-1} with respect to *pristine* IV; in this region, IV features five peaks, assigned to amide I band (C=O stretching, 1657 cm^{-1}), amide II band (N-H bending, 1555 cm^{-1}), carboxylate asymmetrical stretch (1580 cm^{-1}) and ammonium asymmetric and symmetric bending (1617 cm^{-1} and 1491 cm^{-1} respectively)[110]. In thermally treated IV only a strong peak at 1656 cm^{-1} (amide I band) survives. This picture is coherent with a inter- or intramolecular condensation reaction where dipeptide terminal groups react with each other and causing the disappearance of the signals associated to the ammonium and carboxylate groups and the survival of a single amide band. Such a hypothesis is also supported by the disappearance of the NH$_3^+$ stretching broad band between 2500 and 3000 cm^{-1}. It is noteworthy that no amide II band is present in the transformed compound, indicating that the newly formed amide functionality is in a *s*-cis conformation. This is a clear hint of intramolecular peptide bond formation that generates a cyclic dipeptide with blocked amide bond conformation.
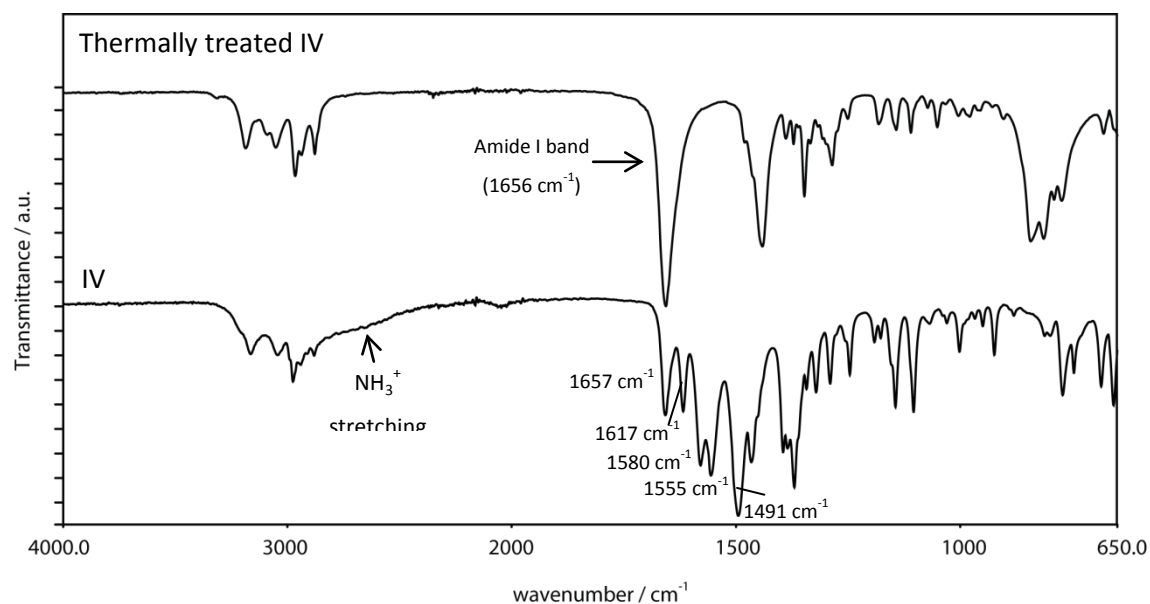
Fig. 93 – IR ATR spectra of IV (bottom) and thermally treated IV (top)

5.1.4. NMR spectroscopy

5.1.4.1.   Solid State NMR

[1]H CRAMPS[111] (Combined Rotation And Multiple Pulse Spectroscopy) 1D NMR technique was employed to characterize both IV dipeptide powders and the thermally treated compound. CRAMPS techniques allow for unprecedented high resolution in the dimension of protons, giving insights on the molecular structure of organic solids and has been used in the past to characterize peptides with success[112]. In Fig. 93 (bottom) the spectrum of IV reported where six main signals are recognized: amide (9.6-9.9 ppm) and ammonium (8.34 ppm) protons, two distinct Hα protons belonging to isoleucine and valine amino acid backbone (5.04 and 4.08 ppm) and aliphatic protons (Hβ 2.14 ppm and superposed methylene and methyl proton overlapped bands centered at 0.78 ppm). Thermally treated compound shows three main features in comparison to the *pristine* peptide:

1) the disappearance of the ammonium signal (coherently with IR evidence);
2) substantially unchanged aliphatic side chains (methine, methylene and methyl protons) region;
3) the disappearance of the two Hα backbone signals, substituted by an upfield shifted singlet (3.67 ppm).
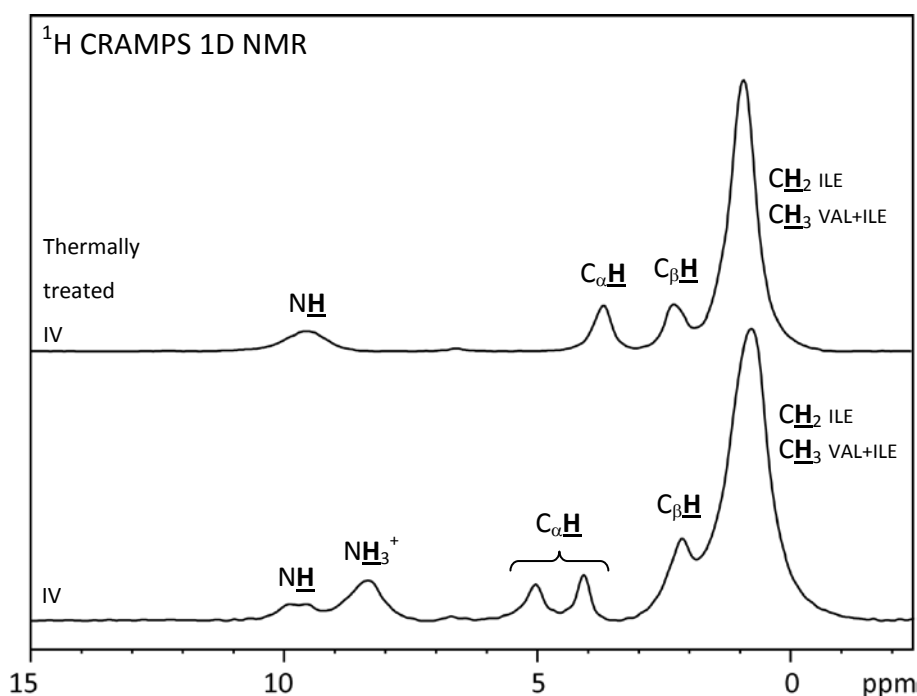
Fig. 94 – ^{1}H CRAMPS 1D NMR spectra of IV (bottom) and thermally treated IV (top). Ammonium protons disappear and the spectrum is simplified in the Hα methine proton region.

In particular, last evidence is in accordance with cyclic dipeptide formation since the two anisochronous CαH protons in the linear dipeptide, which experience different inductive effects (NH_3^+ + amide C=O and amide NH + COO^-), become similar in chemical environment after cyclization (both experience amide C=O and amide NH), producing a signal at 3.67 ppm, presumably arising from the superposition of signals at very close chemical shifts. Survival of a single amide proton signal and the fact that aliphatic protons are not involved in the transformation are additional indications of the cyclization hypothesis.

5.1.4.2. Liquid ^{1}H NMR spectroscopy

Higher resolution proton spectra were recorder using liquid NMR spectroscopy. Methanol was found as common solvent to both IV and thermally treated compound and spectra were recorded on saturated solutions at 45°C to increase the solubility of both analytes (20 mg/ml and 1.5 mg/ml respectively). Ammonium and amide protons are not distinguishable from baseline noise due to well known effects (hydrogen bonding, exchange with solvent, quadrupolar effects) [113]. However, SS NMR picture is herein confirmed as what regards Hα and

the side chain aliphatic protons with Hβ, isoleucine CH$_2$ and methyl groups resolved to a higher extent. Hα protons chemical shifts, which were not resolved in the solid state, reveal to be split into two doublets (3.89 ppm and 3.82 ppm, assigned to valine and isoleucine respectively), whose chemical shift are differentiated by the different substituent effect of the respective alkyl chains.
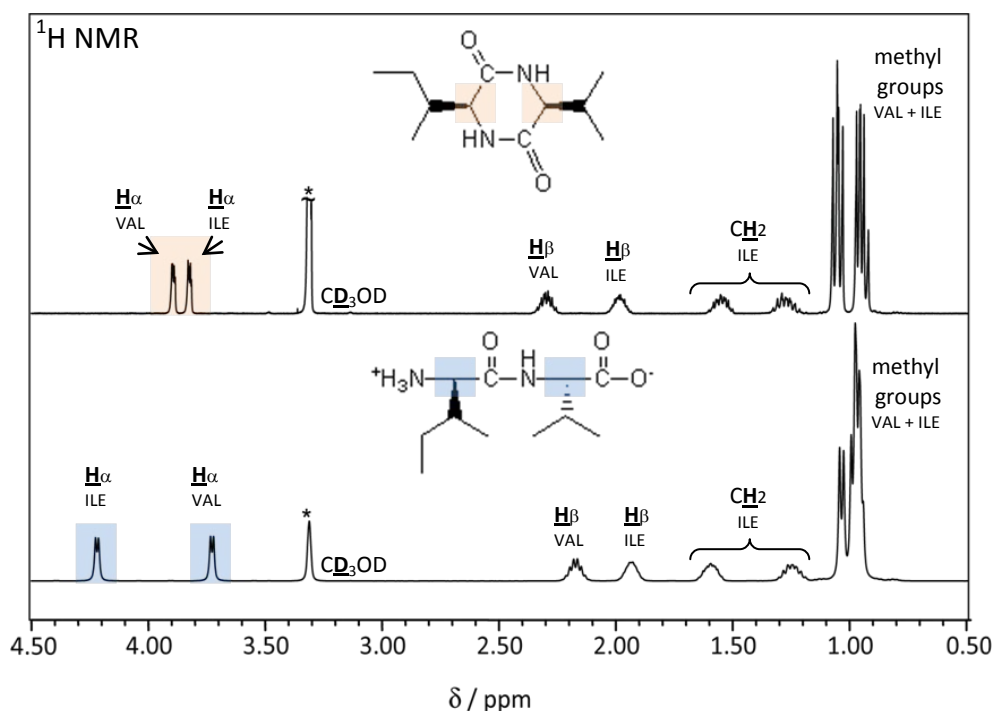
Fig. 95 – ^{1}H NMR (400MHz, CD$_3$OD, 45°C) spectra of IV (bottom) and thermally treated IV (top)

5.2. Comparison with a synthesized cyclic L-isoleucyl-L-valine

In order to confirm that the thermally treated IV is actually the cyclic compound, cyclization of IV was carried out according to a method found in the literature[114] and compound properties were compared with those of the thermally treated IV.

5.2.1. Solution synthesis of cyclic IV

Cyclization of linear unprotected dipeptides is reported to occur in molten phenol at 150°C in good yield[114]. 250 mg of L-isoleucyl-L-valine (IV) were put in a two-necked flask with about 8 grams of phenol. The flask was then purged with nitrogen for several minutes before heating, in order to remove air and prevent darkening of the reaction mixture at higher temperatures.

The mixture was magnetically stirred while the temperature was raised to 140 - 150°C for 3 hours in an oil bath, under nitrogen. As phenol melted, IV dissolved readily yielding a transparent solution. After the reaction time the mixture was allowed to cool down to a white solid which was broken with a glass stick prior to phenol sublimation at 30-40 °C *in vacuo* for 24 h. The white crude was then titrated with chloroform (10 ml) in order to remove any traces of phenol (detected through DSC analysis). The suspension was then filtered over paper using a buchner funnel and water pump, washed again with chloroform (3 x 5 ml) and dried on the filter. The recovered solid weighted 110 mg (48% yield).
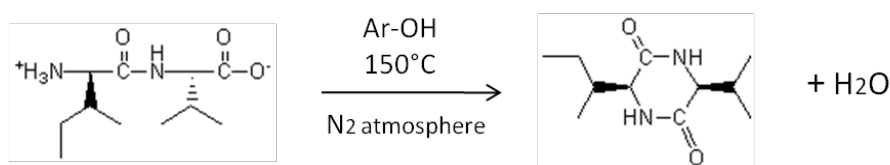
Fig. 96 – Cyclization of unprotected dipeptide in molten phenol

5.2.2. ¹H NMR characterization of cyclic IV

^{1}H NMR spectrum of cyclic IV obtained by solution chemistry was compared with the thermally treated IV. As shown in Fig. 96, the thermally treated IV compound is undoubtedly the cyclic adduct as the identity between the spectra demonstrates. Then, cyclization occurs by means of heating and displacing of water both in a high boiling point solvent and in the solid. Cleaniness and completeness of the solid state reaction is remarkable: no by-products are detected and dipeptides are quantitatively converted into the cyclic adducts, since characterizations of the thermally treated compound, which was examined without any purifications, demonstrate high purity in all cases.
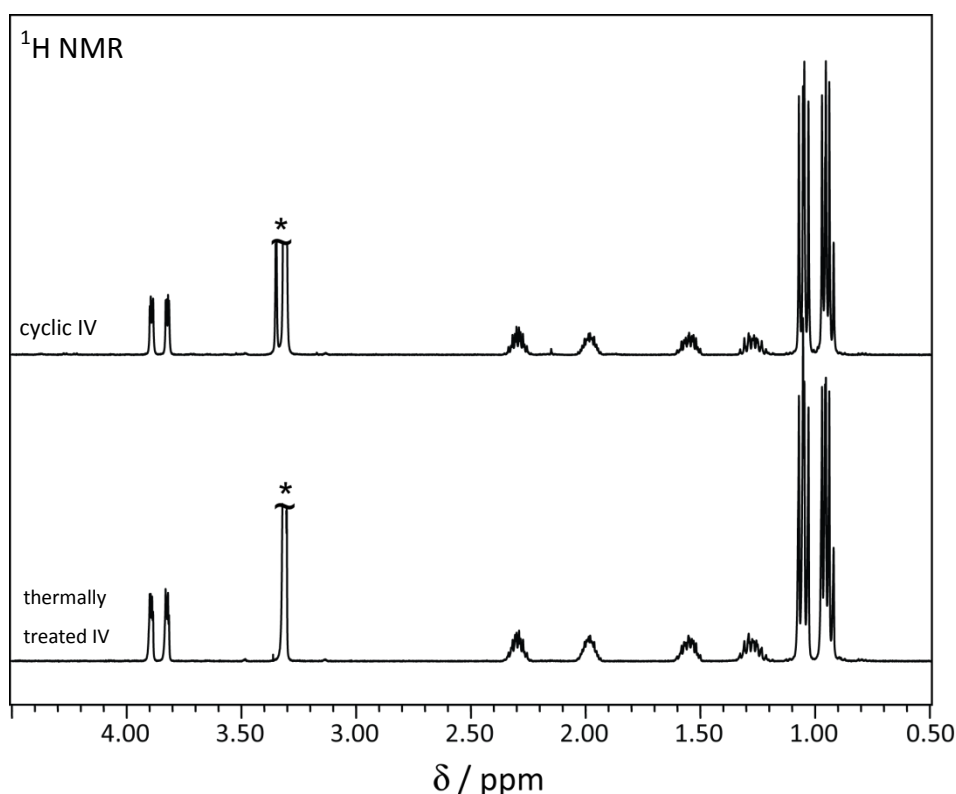
Fig. 97 – ^{1}H NMR spectra of cyclic IV from dehydration in phenol (top) and of thermally treated IV (bottom).

5.3. Crystal-to-crystal transformation

The outcome of the thermal cyclization of IV on its crystal structure was investigated to ascertain if amorphization takes place during thermal treatment or a crystalline material is generated. And if, in the latter case, the transformation occurs in a crystal-to-crystal fashion or via phase change prior to cyclization. The appearance of the solid state NMR spectra of "thermal" cyclic IV suggests that we are in presence of a crystalline solid because of the good resolution attained. On the other hand, phase change prior to cyclization is unlikely: as stated above, IV doesn't melt upon heating around 200°C while TGA curve shows that massive weight loss happens after the discrete step associated to water liberation (namely sublimation at higher temperature involves the cyclic compound and not the linear dipeptide). For this reason, variable temperature X-ray diffraction and optical microscopy were employed to give additional evidence of the hypothesized crystal-to-crystal transformation.

5.3.1. Variable-temperature synchrotron X-ray powder diffraction

Variable temperature X-ray diffractograms were recorded on IV sample, continuously heated *in situ* (heating rate: 2°C min^{-1} from 80 to 240°C) during acquisition.

The series of diffractograms is reported in Fig. 97. Up to 190°C no structural change occurs in the dipeptide which retains its hexagonal nanoporous architecture. At 200°C, cyclization takes place and the diffractogram evidences the comparison of a new phase at the expense of the hexagonal IV. Above 210°C the starting phase is fully consumed and only the new phase is detected, demonstrating complete conversion. Thermal cyclic IV is then a crystalline compound which is stable above 200°C and whose structure is preserved also upon cooling the sample at room temperature.
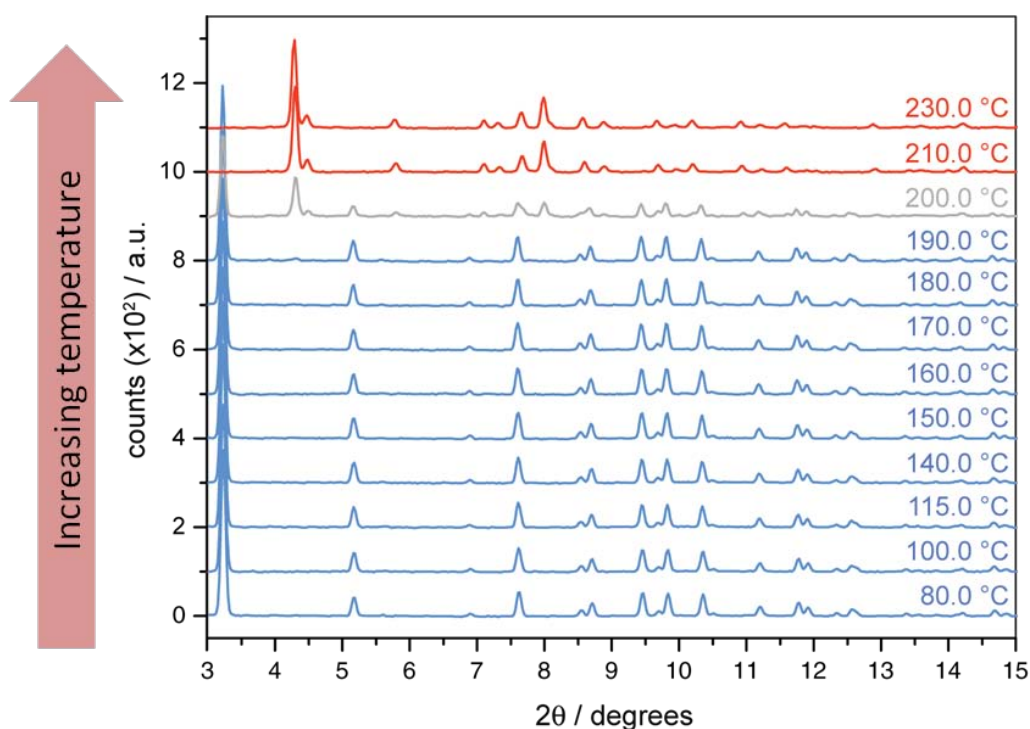
Fig. 98 – Variable temperature synchrotron X-ray diffraction on IV dipeptide. - Cyclization is associated with change in crystal structure.

5.3.2. Polymorphism of cyclic IV

In the attempt to resolve the crystal structure of the cyclic dipeptide, dissolution and recrystallization from a solvent (acetone) was carried out in order to grow single crystals of cyclic IV suitable for single crystal X-ray diffraction. X-ray diffraction was performed on

powders of the recrystallized cyclic dipeptide for screening and the obtained diffractogram was compared to the one of the thermally cyclized dipeptide. However, as Fig. 99 shows, thermal cyclic IV and the recrystallized compound have different powder patterns, indicating the presence of different polymorphs, whose structure depends on the preparation conditions.
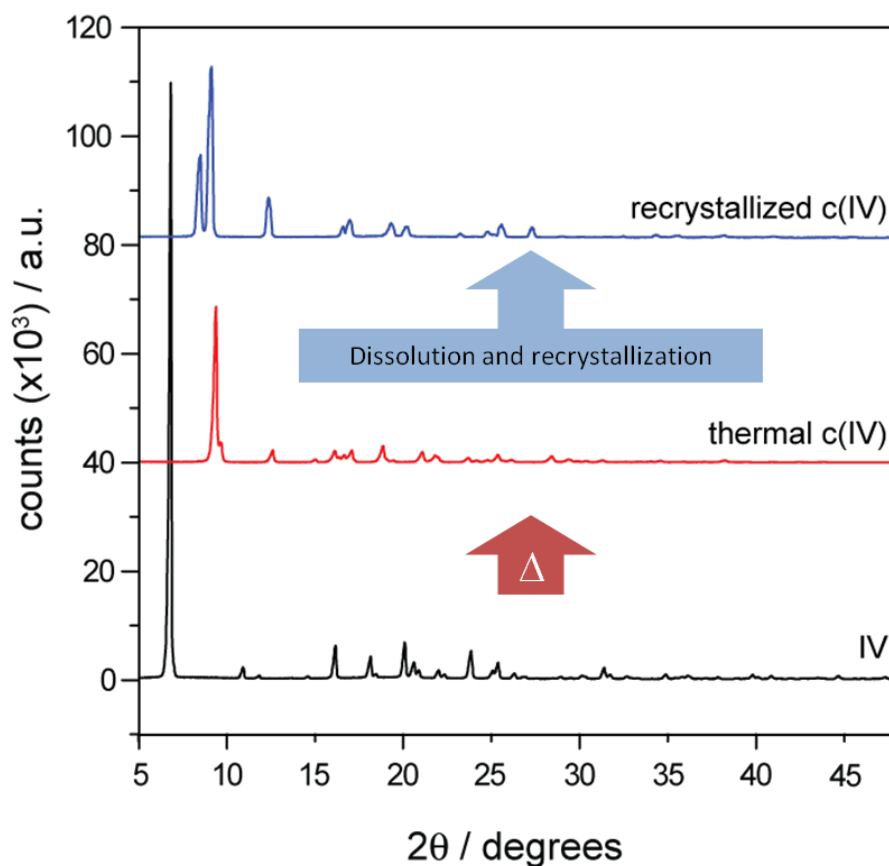
Fig. 99 – Comparison between IV, thermal cyclic IV and recrystallized cyclic IV diffractograms. Recrystallization of cyclic IV from (DMSO/H$_2$O system) affords a different polymorph. (diffractograms were recorded in Bragg-Brentano geometry)

5.3.3. Effect of thermal treatment on IV crystals

Since recrystallization affords a different polymorph with respect to the thermal cyclic IV, the only possibility of having single crystals of the unknown thermal structure is the treatment of IV single crystals, hoping that transformation occurs in a single crystal-to-single crystal fashion. Then, single crystals of linear IV were grown according to the literature reported method[115]. A few crystals were then collected and put in a DSC aluminum open pan and precisely treated in

the DSC furnace up to 205°C (10°C min^{-1} heating) under N_2 atmosphere. Occurrence of the cyclization was monitored by the DSC thermogram. However, the single crystals loose transparency upon heating, suggesting the transformation from monocrystals to polycrystalline species (Fig. 99).
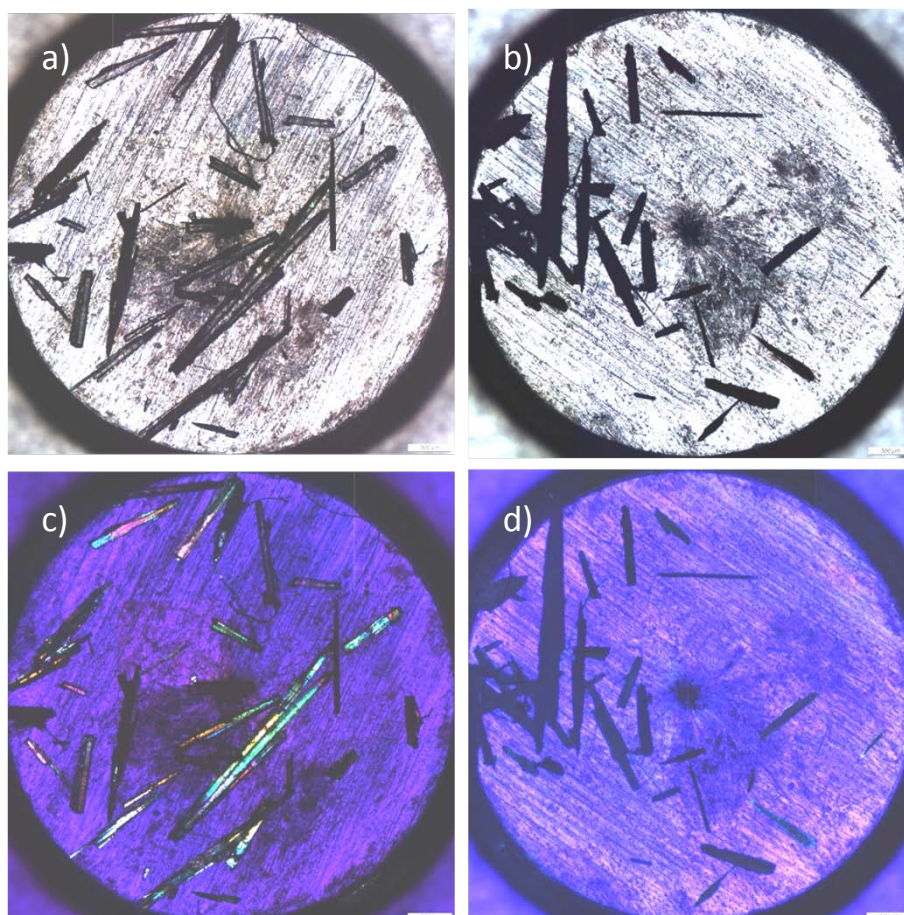
Fig. 100 – Optical micrographs of IV crystals in DSC pan taken prior (a, c) and after heat treatment (b, d), under non-polarized (top) and polarized light (bottom). Scale bars equal 500 μm

Single crystals of IV were treated according to other methods too, using different heating programs combining fast (up to 50°C/min) and slow (5°C/min) heating and cooling ramps but in all cases monocrystals lost transparency.

5.4. Structural determination using powder pattern

Since having single crystals of thermal cyclic IV was impossible, the only way of solving the crystal structure of the "thermal" polymorph was by means of computer-assisted structural determination starting from the quantitative synchrotron radiation powder patterns.

Experimental diffractogram was first indexed using DICVOL04 (FullProf suite), and suggested cells were manually inspected using CHECKCELL to select the best matching space group. The selected cell parameters and space group (P_{212121}) were in substantial agreement with those of other cyclic dipeptide structures where orthorhombic system was preferred, with four molecules per unit cell.

The structure was solved using EXPO 2009[116] software, by means of Simulated Annealing (SA) technique and using the previously found unit cell parameters and space groups as input, together with the modeled atomic positions of the cyclic dipeptide. In this regard, it was reported in the literature that L-L cyclic dipeptides adopt a boat conformation of the six-membered ring with side groups protruding in the same hemi-space[117]. Moreover, a survey of published structures of cyclic dipeptides having similar molecular structure to cyclic IV, *e.g.* cyclo(L-isoleucyl-L-isoleucine[118], revealed that in most cases the six-membered ring is almost flat, with dihedral angles close to 0°. In SA runs, a molecular mechanics (MM2 force field) relaxed model of cyclic IV in flat conformation was employed. A best-fit preliminary structure was produced and cell parameters, isotropic thermal factors and atomic positions were subsequently refined using the Rietveld method with GSAS[119]+EXPGUI[120] softwares (Fig. 100).
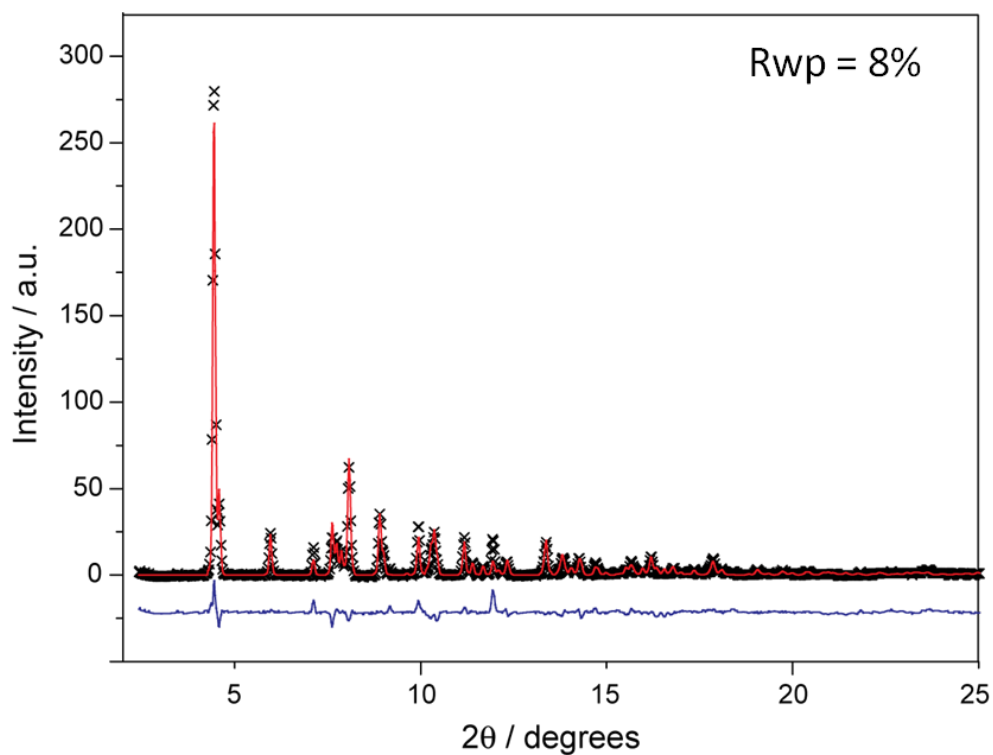
Fig. 101 – Synchrotron radiation X-ray diffraction pattern (black crosses), simulated diffractogram (in red) and difference plot (in blue)
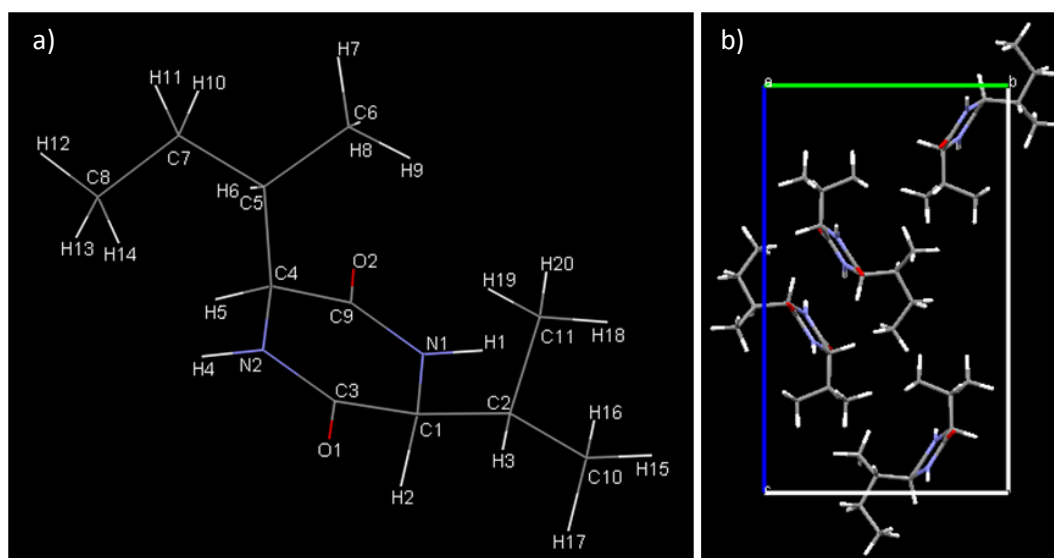
Fig. 102 – Molecular conformation of cyclic IV (a) and crystalline packing viewed along *a* axis (b)

Table 11 – Crystallographic data of the proposed structure of thermal cyclic IV

Name	cyclo(L-isoleucyl-L-valine)
Formula	$C_{11} H_{20} N_2 O_2$
Crystal system	Orthorhombic
Space group	$P\ 2_1\ 2_1\ 2_1$
$\alpha = \beta = \gamma$ / °	90°
a / Å	6.1917(7)
b / Å	10.9422(8)
c / Å	18.1871(2)
Cell volume / Å³	1232.19
Z	4
Rwp	0.0803
N° of reflections	1053
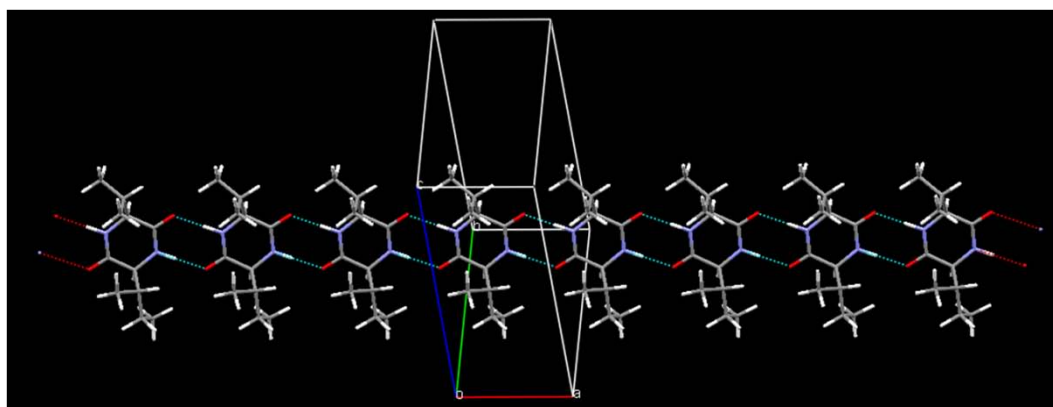
Fig. 103 – H-bonded tape formed by cyclic IV, developing parallel to *a* axis

The proposed structure is depicted in Fig. 101 and features four cyclic IV molecules per unit cell. The most relevant characteristic of the molecular arrangement in the crystal structure is represented by complementary *cis* amide hydrogen bonding between a cyclic dipeptide and two neighboring molecules which affords a hydrogen bonded "tape" (or "ribbon"). This robust motif dominates the intermolecular interactions and is ubiquitous in the crystal structures of cyclic dipeptides[121,122,123]. Each tape is packed laterally by means of Van der Waals interactions with the neighboring ribbons, and hydrophobic side chains interpenetrate to pack the space efficiently (Fig. 103).

The solved solution displays relatively high isotropic thermal factors for carbons (U_{iso} up to 0. 25); in fact, a certain degree of disorder can be expected in the thermally generated cyclic structure which is produced during a non-equilibrium process (solid-state reaction and rearrangement) rather than an equilibrium process (*e.g.* slow crystallization). Moreover, some bond angles appear distorted with respect to the canonical values (for instance, C9-C4-H5 angle equals 97.39°) and the conformation of the six-membered ring, even if still close to planarity, adopts a chair conformation after refinement of atomic positions, which is unusual for cyclic dipeptides, as stated above. Similarly, while hydrogen bond lengths (O1···H1 = 1.90 Å and H4···O2 = 1.93 Å) are realistic, O···H-N angles (about 140°) are low with respect to ordinary values[124].

From the above consideration, it is clear how the proposed structure is not a definitive solution to the structure of thermal cyclic IV, but can be considered a good starting point for a further investigation employing higher quality diffractograms.
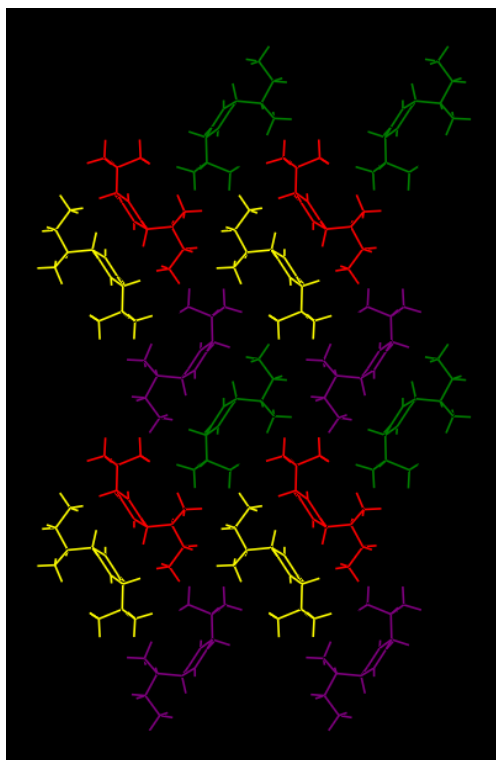
Fig. 104 – Each H-bonded ribbon (seen along tape direction and depicted in different color to highlight translational symmetry) is interpenetrated with neighboring ones by means of Van der Waals contacts of aliphatic side chains.

5.5. Generality of thermal cyclization of nanoporous dipeptides

DSC thermograms of other aliphatic dipeptides are shown in Fig. 104 – DSC thermograms of IV, VI, AV, VA and VV dipeptides. All dipeptides show analogous behavior, with three endothermal transitionsFig. 104 and compared to IV curve. All thermograms show analogous behavior, with transformations taking place at different temperatures. The first transition appears anticipated in IV while it happens at 210°C, 230°C, 240°C and 245°C in VI, VA, VV and AV respectively. Enthalpies of transformations have close molar values (from 48 to 59 kJ mol^{-1}) indicating analogous chemical behavior. Moreover, the first transformation appears to be irreversible as for IV (Fig. 88) for all other four dipeptides.

It is then natural to expect that thermal cyclization occurs in the solid state independently from aliphatic side chain length. Interestingly, a relationship between the temperature of the

(supposed) cyclization and the length of the side chains seems fulfilled with higher molecular weight dipeptides (IV and VI) undergoing cyclization at lower temperature (with respect to AV and VA). In this regard, higher molecular weight dipeptides should have even lower cyclization temperature; indeed, Görbitz reports that during the crystallization of linear L-isoleucyl-L-isoleucine by rapid water evaporation, the cyclic compound also formed (at 60°C only)[125].
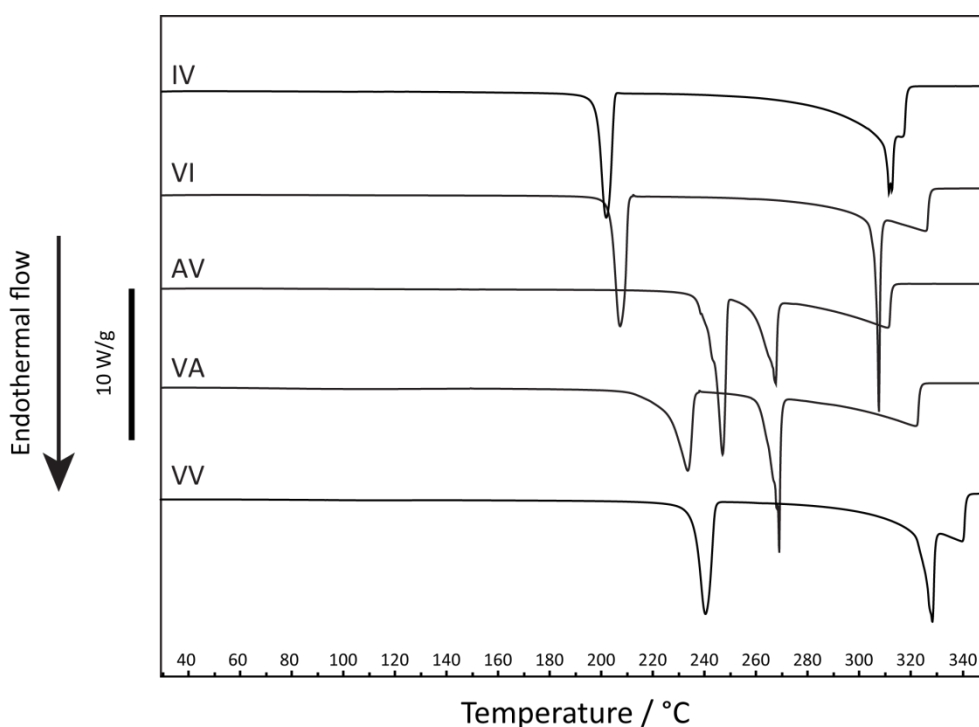
Fig. 105 – DSC thermograms of IV, VI, AV, VA and VV dipeptides. All dipeptides show analogous behavior, with three endothermal transitions.

Obviously, cyclization of a dipeptide and its retro analogue affords the same cyclic compound; therefore, the DSC trace of both IV and VI (or AV and VA), above the temperature of the first transition, should show the same fingerprint. IV and VI show a sharp peak between 310-320 °C followed by evaporation (whose endpoint is dependent of the amount of sample). On the other hand, AV and VA show melting at the exactly same temperature (263°C) with characteristic asymmetrical peak shape and similar profile during quantitative evaporation above 300°C.

5.5.1. Cyclization of VI

VI dipeptide was thermally treated in a buchi oven at 260°C for 1 hour under N_2 atmosphere, and the obtained solid became hydrophobic and showed the same DMSO and methanol solubility as the thermally cyclized IV. ^{1}H NMR proves unambiguously that cyclization takes place since the spectrum is exactly superposable to the one of cyclic IV (Fig. 105)
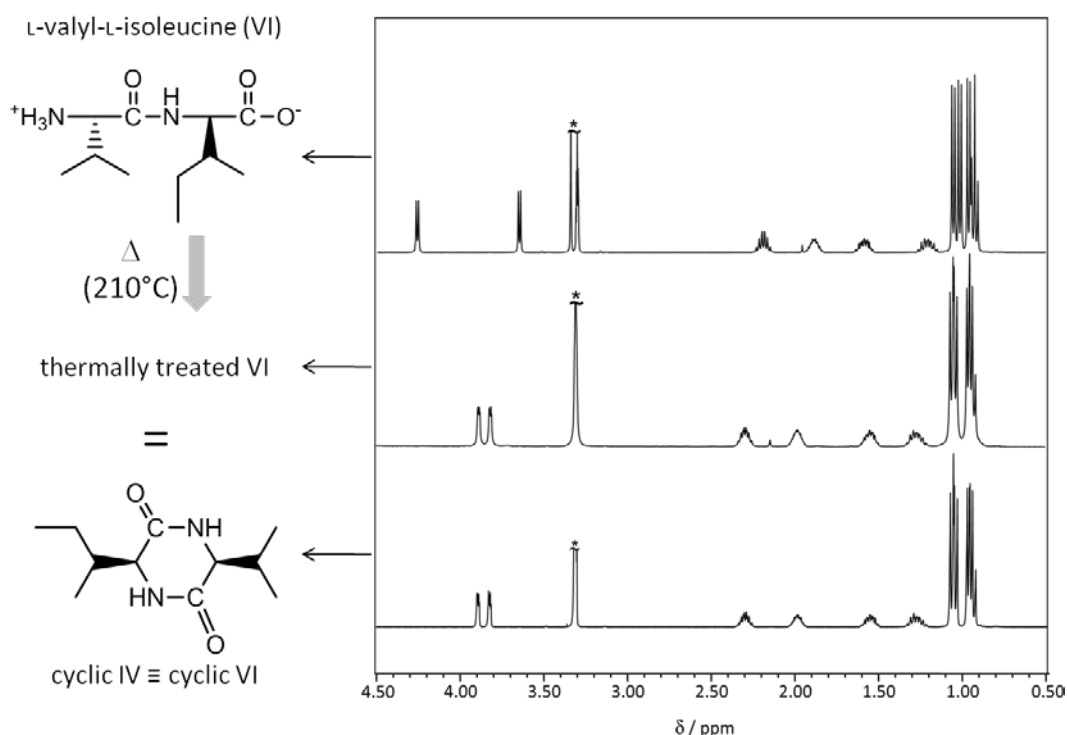
Fig. 106 – ^{1}H NMR spectra of VI (top), thermally treated VI (middle) and cyclic IV (bottom).

5.5.2. Cyclization of VV

VV was treated at 260°C for 1 hour under N_2 atmosphere. The proton NMR spectrum of the thermally treated compound was compared to the spectrum of *pristine* VV (Fig. 106). Also in this case, heating causes intramolecular condensation to occur. The proton NMR spectrum of the treated sample is simplified due to C_2 symmetry, since Hα, Hβ and methyl protons, belonging to two distinct valine unit, become equivalent upon formation of a cyclic structure. For instance, the methyl protons in the linear dipeptides generate four distinct doublets, while only two doublets are present in the case of the cyclic adduct.

117
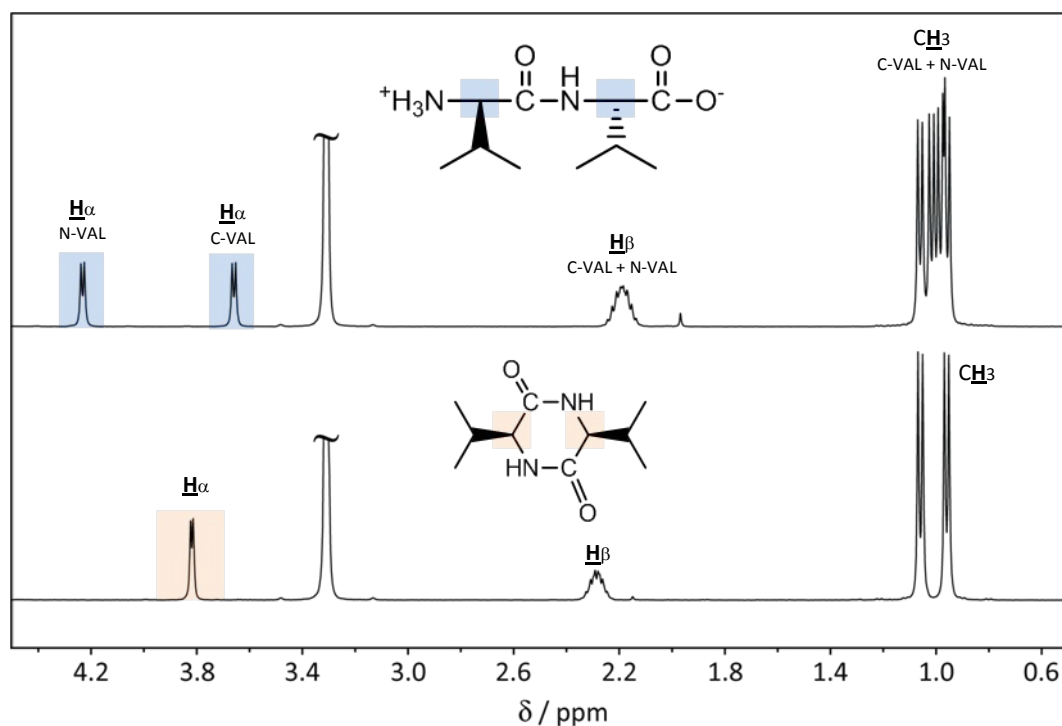
Fig. 107 - ^{1}H NMR spectra of linear VV dipeptide (top) and thermally treated compound (cyclic VV)

5.6. Conclusions

The thermal properties of L-isoleucyl-L-valine (IV) dipeptide were characterized in depth with the discovery of an unexpected solid-state intramolecular condensation reaction yielding the cyclic dipeptide in a clean and quantitative way. It was found that thermal cyclization occurs in a crystal-to-crystal fashion and a crystal structure of the thermal cyclic IV was proposed. Cyclic isoleucyl-valine was produced starting from both L-isoleucyl-L-valine and its retroanalogue L-valyl-L-isoleucine and solid state transformation was demonstrated for L-valyl-L-valine dipeptide too. These evidence together with the DSC fingerprints of other microporous dipeptides (AV and VA), suggest the generality of the phenomenon.

The non-specific formation of cyclic adducts (substituted diketopiperazines) upon thermal degradation of peptides and amino acids was known in the literature since a long time, but this is the first time that the solid state thermal conversion of linear dipeptides into their cyclic counterparts was recognized, with reaction occurring at characteristic temperatures.

Lately, cyclic dipeptides have attracted interest for their potential bioactivity because of their robust scaffold and constrained three dimensional geometry of the amino acid side chains which can efficiently interact with molecular receptors in a specific way. Moreover, they have

been used as tectons for the construction of supramolecular soft materials (*e.g.* organogels), due to the self-complementary H-bond donor and acceptor moieties on the molecule's six-membered ring. Synthetic strategies for diketopiperazine preparation generally rely on classical multi-step solution-based chemistry with the involvement of protective and activating groups to promote the dipeptide ring closure. The discovery of such spontaneous and clean conversion reaction might thus lead to a more general protocol for substituted diketopiperazine synthesis.

Chapter 6 – Conclusions and outlook

The present PhD thesis had the objective of investigating hydrophobic dipeptides and to propose them as novel - and viable - microporous materials. By taking advantage of the tunable pore size of the dipeptide channels, it was possible to characterize their discrimination properties both in the interaction with gas molecules and in chemical reactions taking place in their linear cavities. As the porous architectures provide channel environments having homogeneous chemical properties (dipeptide channels are decorated with aliphatic groups), the host-guest interactions were governed genuinely by geometrical factors, such as nanotube diameter and shape.

In this regard, the interaction with gas molecules was investigated by our group in the past, with the assessment of the sorption properties of L-alanyl-L-valine (AV), L-isoleucyl-L-valine (IV) and their retro-analogues (VA and VI) towards methane, carbon dioxide and hydrogen, highlighting how larger accessible pore volume increased the final loading capacity while smaller pore diameter enhanced host-guest stabilization (higher heat of adsorption). Moreover, dipeptides demonstrated high affinity towards CO_2. Those results prompted a step ahead on the direction of investigating selective gas-dipeptide interactions, with the design and realization of a new experiment to characterize competitive gas sorption on nanoporous

dipeptides. AV, IV and VI dipeptides have been tested and their selective and reversible physisorption of carbon dioxide over methane was demonstrated in gas breakthrough experiments at room temperature and near ambient pressure. Pore size influenced the carbon dioxide capture performances, with the smallest pore channel of VI being the most effective, followed by IV and AV, in the same order of increasing pore diameter (Chapter 2).

One-dimensional nanocavities of dipeptides proved capable to incorporate monomer molecules which were subsequently polymerized *in situ* by radical polyaddition, generating dipeptide⊃polymer nanocomposites. Linear topology of the channels was transferred to the synthesized polydienes (1,4-*trans*-polypentadiene and 1,4-*trans*-polyisoprene), regardless of pore geometry, in all dipeptides investigated. In addition, polymerization of acrylonitrile in VA, IV and VI yielded atactic polyacrylonitrile (PAN); instead, highly isotactic polyacrylonitrile was obtained in AV nanochannels. This result demonstrates that even a subtle change in channel geometry can generate a polyolefin with markedly different stereochemistry. Understanding the mechanistic reasons for such a different behavior is not straightforward; however, comparison between AV channel shape and the one of another nanochannel known to generate isotactic PAN (urea inclusion compound) highlighted close similarities involving nanotube size, cross section modulation, helicity and shape (Chapter 3).

So, dipeptides could be used to manipulate matter at the sub-nanometer scale: different gas molecules interact selectively with the nanopores while reacting monomers are compelled to comply with channel geometry which, in some cases, imparts even stereochemical order to the polymer. In addition, molecular anisotropy and microscale control can be imprinted to the polymeric material generated *in situ*. In fact, the nanocomposite crystals aspect ratio (needles) is inherited by the generated polymeric micro-fibrils as the dipeptide architecture is removed; moreover, polymer chains in the fibrils are uniaxially aligned, keeping memory of nanochannel anisotropy. Such concepts were demonstrated in Chapter 4, where PAN microfibrils were generated from AV⊃PAN nanocomposite and thermally converted to carbon fibrils having anisotropic properties.

Finally, thermal properties of IV were characterized in depth, with the discovery of an unexpected crystal-to-crystal irreversible transformation caused by dipeptide intramolecular cyclization, occurring at a characteristic temperature (~200°C). Such unreported transformation appears to be common to all other hydrophobic dipeptides investigated (AV,

VA, VV and VI). These results contribute to the better understanding of these novel materials, which are still scarcely characterized, and suggest a general method for the synthesis of cyclic dipeptides (Chapter 5).

The promising results obtained in the present work prompt future research in every aspect investigated so far. For instance, competitive CO_2/CH_4 gas sorption can be studied on the other dipeptides of the VA class (namely VA, VV, IA and AI). Taking advantage of the modular experimental setup developed in-house for the purpose, different gas mixtures can be tested to select the best performing dipeptide in each potential industrial application (*e.g.* CO_2/N_2 and CO_2/H_2 separations). Incidentally, the development of the separation system allowed the build-up of the necessary know-how to improve the technique in the future, with the intervention on experimental parameters such as gas flow, gas pressure, temperature, adsorbent bed geometry *et cetera*.

Dipeptide materials demonstrated all their versatility as nanovessels: investigation can be extended to other diene and vinyl monomers, provided the necessary steric requirements for inclusion/adsorption. Polymer can be recovered with ease and dissolved dipeptide can be recrystallized, regenerating the microporous architecture which can be recycled. Moreover, polymerizations can be potentially obtained without recurring to γ-ray irradiation: polymerization in presence of a radical initiator can be a valid alternative, though in the present work ionizing radiation was considered more convenient. In addition, the possibility of imparting anisotropy to guest molecules both within the nanocomposite and in the final polymeric fibrils is tantalizing if functional polymers could be obtained *in situ* (*e.g.* conductive polymers).

However, large scale use of dipeptides is precluded at the moment due to their large unitary cost on the market as fine chemicals. On the other hand, industrial scale up is feasible as other examples demonstrate: for instance, the sweetener aspartame is a dipeptide produced industrially at commercially viable costs. Moreover, dipeptides can be potentially synthesized from biomasses by fermentative processes or enzymatic digestion.

It is not unlikely that such simple peptide materials will be among the first taking advantage of new hybrid synthetic strategies as biotechnology and materials science will synergistically act to finally disclose the forthcoming "Protein Age".

Appendix A – Theory of Adsorption

App A 1.   IUPAC adsorption isotherms

The main characterization for adsorption properties of a nanoporous materials towards a gaseous (or vapor) species consists in the measurement of the so called "adsorption isotherm". In fact, for each value of external gas pressure, at a constant temperature and in equilibrium, an exact ratio between adsorbed gas amount and the matrix amount in the system exists. It is possible to write the equation:

$$\frac{n_{ads}}{m_{pore}} = f(p_{eq})_T$$

where n_{ads} is the amount of adsorbed gas (in mol or other units), m_{pore} is the amount of porous sorbent (in mol or other units), p_{eq} is the equilibrium pressure and T is temperature.

The analytical form of f function (adsorption isotherm) depends on the kind of adsorptive system involved: in fact, according to the IUPAC classification, six kinds of isotherms exist. The characteristics of each one are described briefly below.
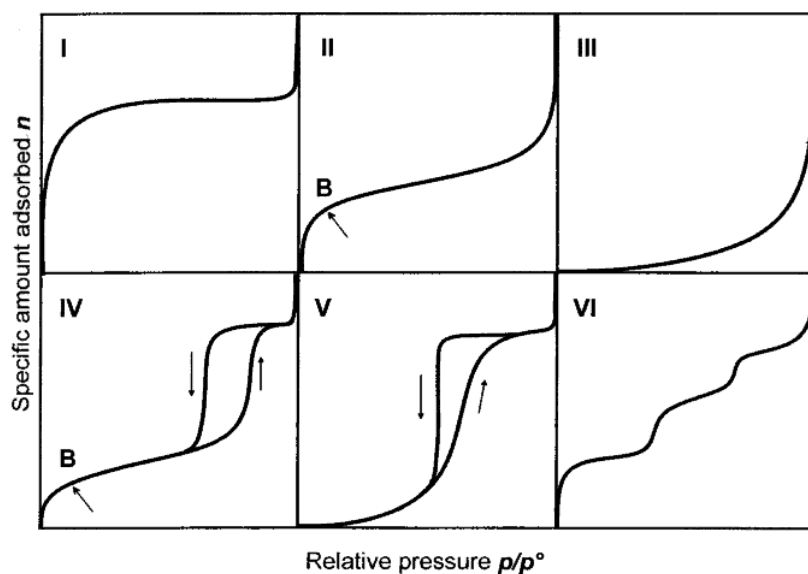
Fig. 108 – Forms of the six different adsorption isotherms according to IUPAC classification

Type I isotherm: it is also called Langmuir isotherm after Irving Langmuir, who pioneered the study of interfaces, surfaces and films in the beginning of XX century. This isotherm is typical of microporous systems (<2 nm pore diameter): as equilibrium pressure is increased, the amount of species adsorbed increases as well, up to a limiting value. Asymptotic *plateau* can be ascribed to the formation of a monolayer of adsorbed gas. In microporous systems, the decreasing of pore size leads to the increase of the adsorption energy. A tight fit between the pore size and the size of the species adsorbed is able to maximize the supramolecular interactions. A small pressure interval to reach for saturation is symptomatic of reduced volume.

Type II isotherm: this is the typical behavior of macroporous or non-porous materials and has sigmoidal shape. Systems which feature this dependency are characterized by the formation of more than one layer of adsorbed species. As pressure is increased from zero, its shape reminds of that of Langmuir isotherm (monolayer formation) but as pressure is increased to higher values the amount of adsorbed species doesn't approach a limiting value but is continuously increased (multilayer formation). Hysteresis is absent.

Type III isotherm: it shows a convex shape with respect to pressure axis at all equilibrium pressures and no saturation is evidenced. This kind of isotherm is rare and is reported to be

associated to non-porous solids where a new layer forms before the layer beneath is complete. Such a situation denotes preferential interaction between adsorbed species rather than with the surface.

Type IV isotherm: it is typical of mesoporous materials (2-50 nm pore diameter). At low coverage, the shape is analogous to type II isotherm, but a plateau is present at higher pressures. Passing from monolayer to multilayer, condensation of the adsorbed species occurs and the condensed phase fills all the available volume. Almost always, hysteresis is evidenced at high relative pressures, due to capillary condensation in tight pores. Hysteresis affected desorption curve is used to determine pore volume based on pore diameters.

Type V isotherm: analogous to type IV, with the difference that a multilayer is formed prior to condensation of adsorbed species. Hysteresis is also present, as for type IV.

Type VI isotherm: it is a step-shaped isotherm and it is associated to the formation of multilayers in an ordered way (layer-by-layer) or to materials with active sites having discrete differences in adsorption energy. Such kind of profile is rather rare.

Experimental measurement of adsorption isotherms is based on two methods: volumetric or gravimetric. In the volumetric determination (used in this work) the pressure drop due to adsorption by the porous material is measured at known temperature and volume. As gas is adsorbed, the pressure decreases until the equilibrium pressure is reached. The difference between starting pressure and final equilibrium pressure allows for the calculation of the amount of adsorbed gas by means of the equation of state of ideal gases. Gravimetric method is based on the increase of the adsorbent mass upon adsorption.

App A 2. Langmuir isotherm

With a simple model, based on reasonable assumptions, it is possible to calculate the analytical form of the Langmuir isotherm. Being θ the adimensional surface coverage, defined as

$$\theta = \frac{\text{number of occupied surface sites}}{\text{number of total surface sites}}$$

Langmuir isotherm defines the relationship between coverage of the first adsorbed layer and gas pressure at a constant temperature. In this model the following hypotheses are made:

1) all available adsorption sites are equivalently accessible to the adsorbed species;

2) monolayer adsorption occurs only;

3) adsorption energy on a site is independent from the occupation of the neighboring sites.

The aforementioned assumptions neglect the creation of new adsorption sites (exclusion of multilayer adsorption) or reciprocal cooperation/competition between adsorbed molecules. Adsorbed molecules are considered in dynamic equilibrium with unbound gaseous molecole according to the equation:

$$A(g) + M(\text{surface}) \xrightleftharpoons[\text{k des}]{\text{k ads}} AM(\text{surface})$$
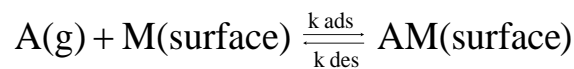
If we define k_{ads} is the kinetic constant of the adsorption process ([pressure time]$^{-1}$) and k_{des} the kinetic constant of the desorption process ([time]$^{-1}$), speed of adsorption v_{ads} is proportional to the gas pressure p and to the number of available sites on the surface (N is the total number of adsorption sites):

$$v_{ads} = \left(\frac{\partial \theta}{\partial t}\right)_{ads} = k_{ads}\, pN(1-\theta)$$

Analogously, desorption speed v_{des} is given by the equation:

$$v_{des} = \left(\frac{\partial \theta}{\partial t}\right)_{des} = k_{des} N\theta$$

As kinetic equilibrium is reached, both adsorption and desorption have the same speed yielding the expression of Langmuir isotherm as a function of the coverage:

$$\theta = \frac{Kp}{(1+Kp)}$$

with K = k_{ads}/k_{des} being the equilibrium constant [pressure^{-1}], dependent on the temperature. High values of K indicate a higher affinity for the gas towards the adsorbent. K increases as temperature decreases.
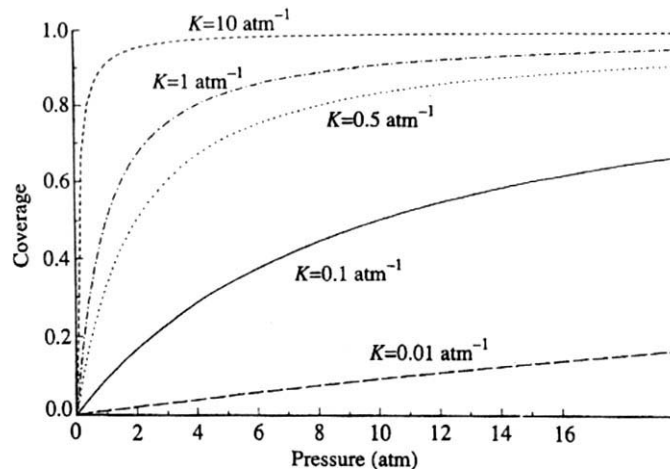
Fig. 109 – Trend of the Langmuir isotherm profile as K is increased

θ ranges from 0 to 1 and for this reason it is not correlated to the measured physical quantities. Langmuir isotherm must be normalized to the experimental values:

$$\theta_{mol} = \theta_{max} \frac{Kp}{(1+Kp)}$$

where θ_{mol} is the coverage expressed as the molar ratio between adsorbed gas and adsorbent material, while θ_{max} is the asymptotic value of the *plateau* for p_{eq} tending to $+\infty$. θ_{max} e K parameters can be obtained from the experimental data using the Langmuir linear regression:

$$\frac{p}{\theta_{mol}} = \frac{p}{\theta_{max}} + \frac{1}{K\theta_{max}} .$$

Plotting the ratio between equilibrium pressure and molar coverage vs. equilibrium pressure a line is obtained having θ_{max}^{-1} as slope and $(K\,\theta_{max})^{-1}$ as intercept.

Appendix B – Experimental methods

App. B 1.   X-ray powder diffraction

X-ray powder diffraction experiments on pure dipeptides, thermally treated IV, recrystallized cyclic IV and dipeptide⊃polymer nanocomposites were performed using a Bruker D8 diffractromer in the Bragg-Brentano geometry, at room temperature. The radiation wavelength λ of the incident X-rays was 1.54 Å and a 2θ range from 5° to 60° was investigated. Each step (0.02° intervals) was recorded for 20 s.

Synchrotron radiation (λ = 0.7277 Å) was used to record quantitative diffractograms for dipeptides and dipeptide   PAN nanocomposites at room temperature (European Synchrotron Radiation Facility - ESRF, in Grenoble - France). Each diffractogram was collected for 600s.

Variable temperature XRPD experiments on L-isoleucyl-L-valine were performed at ESRF, using a heating ramp of 2°C min^{-1} from 80°C to 240°C. Diffractograms were acquired during heating under N_2, and were accumulated for 120s each. After cooling, the diffractogram of the cyclized dipeptide was recorded at room temperature (120s).

Cell parameters of dipeptides were refined on the room temperature synchrotron diffractograms by Rietveld refinement using the literature reported crystal structures of dipeptides[126]. Cell parameters of dipeptides⊃polymer samples were further refined by the Le Bail structureless procedure to accurately match peak intensities. Refinements were performed by least squares analysis using GSAS[119]+EXPGUI[120] softwares.

Tentative solution of "thermal" cycle IV structure from synchrotron powder pattern was performed as follows. Powder pattern was indexed using DICVOL04 (FullProf[127]+winPLOTR[128] suite) to identify the cell parameters and space group. Then, CHECKCELL[129] was used to compare calculated reflection positions and experimental diffractogram to choose the best matching unit cell. "Simulated Annealing" was run with EXPO 2009[116] software (SA conditions: initial temperature = 23, temperature reduction = 0.80, n. of cycles per temperature =238, tolerance for termination = 2.00, cost function = R weighted profile). A molecular model of cyclic(L-isoleucyl-L-isoleucine) was used as fragment with 13 degrees of freedom (6 external + 7 internal-torsional). Among the ten structures output by the algorithm, the best was further refined by Rietveld method using GSAS+EXPGUI softwares (cell parameters, thermal factors and atomic positions).

App. B 2.   Thermogravimetric Analisys (TGA)

TGA measurements were performed on a Mettler Toledo TGA/DSC 1 STAR^e System with horizontal furnace. Accurately weighted (~10 mg) samples were run from 30 to 400 °C at a heating rate of 10 °C min^{-1} under a protective atmosphere (N$_2$ flow, 50 ml min^{-1}). Standard 70 μL alumina pans were used. Raw experimental curves were corrected by subtracting a blank run under the same experimental conditions.

App. B 3.   Differential Scanning Calorimetry (DSC)

Differential Scanning Calorimetry (DSC) was performed on a Mettler Toledo DSC821^e STAR^e System. Samples (~5 mg) were usually run from 25 to 350 °C at 10 °C min^{-1} heating rate (were not otherwise specified), under protective N$_2$ flow (80 ml min^{-1}). Standard 40 μL aluminum pans were used.

App. B 4.   Liquid NMR

Solution ^{1}H and ^{13}C NMR experiments were performed on a Varian MERCURY AS-400 spectrometer operating at 400 MHz. Chemical shifts (δ) are reported in parts per million (ppm) downfield from tetramethylsilane (TMS) using the residual solvent peak as an internal reference or TMS where added.

^{13}C NMR spectra of polymers were recorded on 20-40 polymer mg/ml solutions in deuterated solvents (polyacrylonitrile solvent: DMSO-d*6*, polypentadiene and polyisoprene solvent: CDCl$_3$). Due to high viscosity of the polyacrylonitrile solutions, measurements were performed at 80°C. Pulse width: 90°, acquisition time: 1.6 s, recycle delay: 10 s, 5000-10000 scans. Inverse gate decoupling was used for quantitativity, with decoupling ON during acquisition only, to suppress the Nuclear Overhauser Effect. However, higher resolution spectra of polyacrylonitrile were acquired with full decoupling, without affecting the internal ratios of sequence-sensitive signals[130]. ^{1}H NMR spectra of polymers were recorded in diluted solutions (1-2 mg polymer/ml) at room temperature. Pulse width: 45°, acquisition time: 1.2s, recycle delay: 5 s, 128 scans.

^{1}H NMR spectra of linear and cyclic dipeptides were recorded at 45°C in deuterated methanol (1 mg/ml).

App. B 5.   Solid State NMR

The ^{13}C solid-state NMR spectra were run at 75.5 MHz on a Bruker Avance 300 instrument operating at a static field of 7.04 T equipped with either 4 mm or 7 mm double resonance MAS probe. The samples were spun at the magic angle at a spinning speed ranging from 5 to 15 kHz, and ramped-amplitude cross-polarization (RAMP-CP) transfer of magnetization was applied. For recycle delays and contact times in ^{13}C cross-polarization (CP) MAS experiments, refer to text.

^{1}H CRAMPS 1D NMR spectra were collected at 500 MHz on a Bruker Avance 500 instrument equipped with a 2.5 mm double resonance MAS probe.

App. B 6.   Viscosimetric estimation of PAN molecular weight

Viscosimetric molecular weight (Mw_v) was estimated for PAN by means of the Mark-Houwink equation

$$[\eta] = K \, Mw_v^{a}$$

where [η] is the intrinsic viscosity and K (0.0520 ml g^{-1}) and a 0.690 (adimensional) are experimental parameters for DMF solution at room temperature[131]. Intrinsic viscosity [η] was obtained by linear extrapolation of reduced and inherent viscosities at infinitesimal PAN concentration. Measures were performed on an Ostwald viscometer. A minimum of five different concentrations were used for each polymer with at least ten efflux times recorded at each concentration.

App. B 7.   Steric-Exclusion Gel Permeation Chromatography

1,4-*trans*-polypentadiene and 1,4-*trans*-polyisoprene molecular weight distribution was evaluated by Size Exclusion - Gel Permeation Chromatography (SEC-GPC) on a Waters instrument (module 1515) equipped with two Styragel columns (HT 4 and HT 5) and refractive index detector (module 2414), using chromatographically pure THF and toluene as solvent and internal standard, respectively. Calibration curve was measured using 10 polystyrene narrow standards ranging from 2 kDa to 1 MDa molecular weight. Polypentadiene molecular weighs are expressed in polystyrene equivalents.

App. B 8.   Optical Microscopy

Optical microscopy photographs were obtained using a Leica DMLM microscope equipped with a Leica DFC 280 digital camera.

App. B 9.   Scanning Electron Microscopy and Energy Dispersive X-ray microanalysis

Scanning Electron Microscopy (SEM) images were obtained by a TESCAN-VEGA TS 5136 XM-SEM instrument operating at 20 kV. The samples were deposited on an adhesive graphite disc

and sputter-coated with a thin layer of gold before imaging. Pyrolized samples were not coated. Energy Dispersive X-ray microanalysis of graphitized microfibrils (EDAX-GENESIS 4000 microanalysis accessory) was performed on sample deposited on a silicon holder with electron beam focused on individual pyrolyzed fibrils.

App. B 10. μRaman Scattering

μRaman Scattering experiments were performed in the backscattering configurations X(Z,Z+Y)-X and X(Y,Z+Y)-X, with fibril axis parallel to Z, using a linearly polarized argon laser (λ_L = 488 nm). Samples were accurately selected by *in situ* optical microscopy in order to focus the irradiation spot over a single fibrillar particle. To fit the experimental data, five *pseudo*-Voigt peaks were used in the profile refinements to account for all the superposing Raman active bands in the range 900 to 2000 cm^{-1} (namely the I, D, D', D'' and G bands, according to reference 132). Generalized Tuinstra-Koenig (TK) equation[133]

$$L_a \text{ (nm)} = 2.4 \times 10^{-10} \, \lambda_L^4 \, (I_D/I_G)^{-1}$$

where λ_L is the laser wavelength expressed in nanometer units and I_D and I_G are the integrated intensities of the D and G bands respectively, was used to evaluate the "in plane" L_a graphite crystals dimensions.

App. B 11. Attenuated Total Reflection FT-IR Spectroscopy

FT-IR spectra were recorded on a Perkin Elmer 100-TF Infrared operating in Universal ATR configuration. Spectral width: 650-4000 cm^{-1}, 16 scans.

App. B 12. Determination of nanochannel morphology

Morphology of the channels was determined as follows. Structural atoms were rendered as spheres with canonical Van der Waals *radii* (1.55 Å, 1.52 Å, 1.70 Å and 1.2 Å for N, O, C and H, respectively) plus 1 Å. The resulting solid was subtracted to a cylinder with axis of symmetry coincident with the structure's 6-fold screw axis, using Constructive Solid Geometry (CSG) function provided by POV-Ray[134] software. The obtained "carved" solid corresponds therefore to the volume accessible by a 1 Å radius sphere exploring the channel. Channel slices are obtained intersecting the cavity solid with a plane perpendicular to the *c* axis. This plane was

lifted from origin to *c*/6, in ten evenly spaced steps. Areas of the sections were measured using ImageJ[135] and channel profile was plotted as section area vs. section height. CSG allows unlimited detail of the rendered voids with respect to ordinary techniques; for instance, probe-on-grid exploration in CCDC's Mercury[136] can produces an equivalent "solvent accessible surface" but at a much higher computational cost.

App. B 13. Vapor adsorption experiments

Vapor adsorption isotherms were collected using a manifold composed of three known volumes (V_1, V_2 and V_3) interconnected by teflon Rotaflos valves (R_1, R_2 and R_3) as depicted in Fig. 109. 200 mg of activated dipeptide (60°C at 10^{-2} mmHg overnight) is transferred to a glass vial which is then connected to the manifold (Fig. 109-a) and evacuated for additional 2 hours at room temperature. Liquid *n*-pentane (2 ml, Sigma-Aldrich) was transferred in a second vial which is connected to the manifold in position b). Pentane was degassed by means of three freeze-vacuum-thaw cycles using liquid N_2. Liquid pentane was allowed to equilibrate with its own vapors at room temperature and vapors were dosed in volume V_2. Dipeptide and pentane vapors were contacted by opening valve R_3 (while R_4 and R_2 valves are kept closed). To the drop in pressure due to the abrupt expansion of vapor against *vacuum*, additional pressure decrease was evidenced, due to the entering of pentane vapors into the nanopores. Adsorption kinetics (the decrease of pressure over time) were recorded until the reaching of a final equilibrium pressure $p_{eq,1}$. Molar amount of adsorbed *n*-pentane x_1 was calculated by means of the equation of ideal gases (which in case of *n*-pentane holds up to vapor pressure at room temperature). After equilibrium is attained, the volume containing the dipeptide was excluded (valve R_3 is closed) and additional vapors were allowed to enter volume V_2 from the vapors reservoir (volume V_1) through valve R_2. The procedure was repeated with the attaining of a new equilibrium pressure $p_{eq,2}$. So, vapors are dosed to the dipeptides in cumulative steps up to pentane vapor pressure (p_0 = 450 mmHg). Adsorbed *n*-pentane in each step was added to the amount already adsorbed during previous steps: $X_i = \Sigma_{n=0 \to i} x_n$. A list of ($p_{eq,i}$, X_i) is generated, which corresponds to the adsorption isotherm, which can be normalized to the molar amount of sorbent.
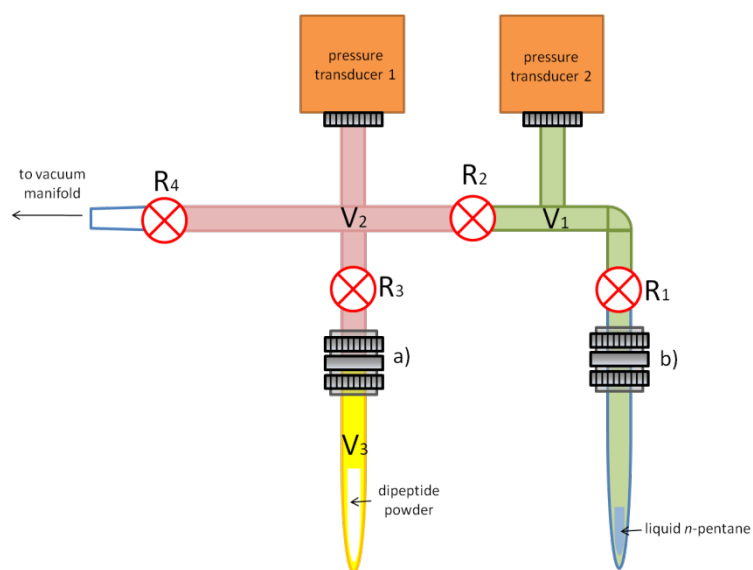
Fig. 110 – Scheme of manifold used in vapor adsorption measurements.

Temperature was monitored during the experiment using a thermocouple thermometer with a precision of 0.1°C, while precision of pressure active-strain gauge was 0.1 mmHg. *Vacuum* level was measured with a pressure transducer having 10^{-4} mmHg full scale. All pressure transducers were connected to a digital detector interfaced to a personal computer.

Appendix C – Additional Data

App. C 1. Powder X-ray Diffraction (Synchrotron radiation) of dipeptides and Rietveld refinements
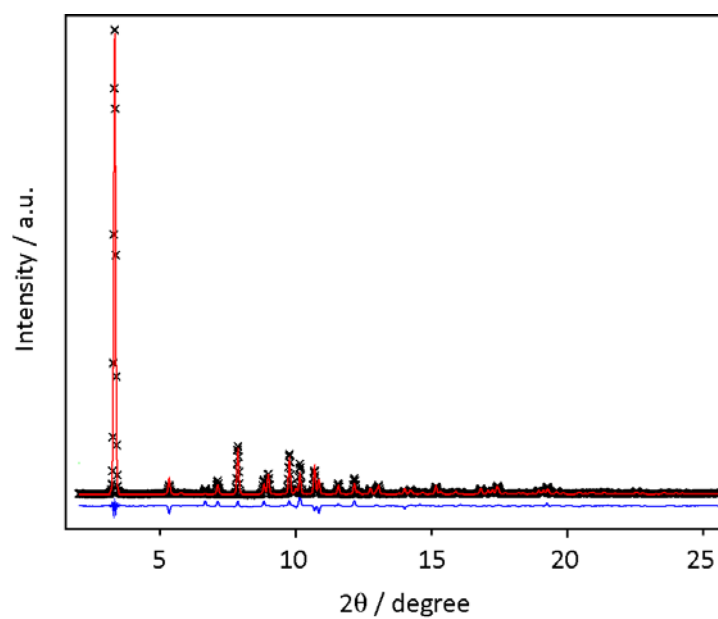
Fig. 111 - Synchrotron radiation diffractogram of AV dipeptide (black crosses), calculated Rietveld profile (red line) and difference plot (blue line)
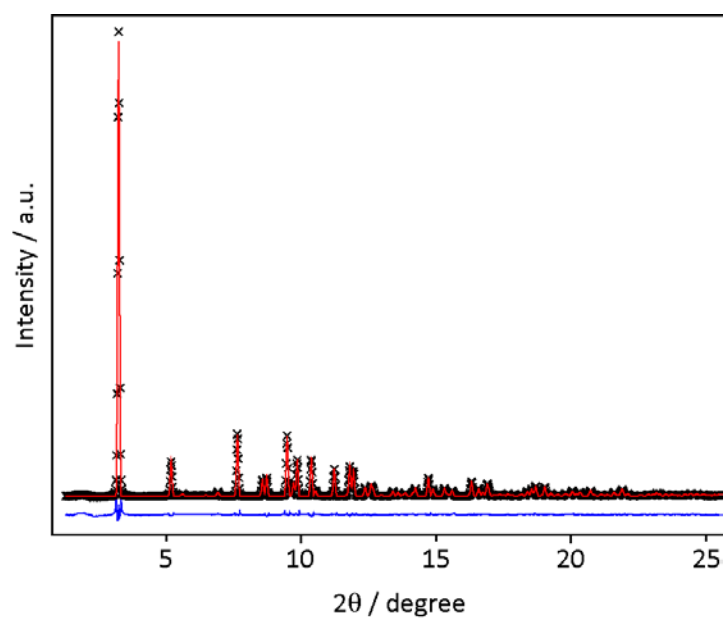
Fig. 112 - Synchrotron radiation diffractogram of IV dipeptide (black crosses), calculated Rietveld profile (red line) and difference plot (blue line)
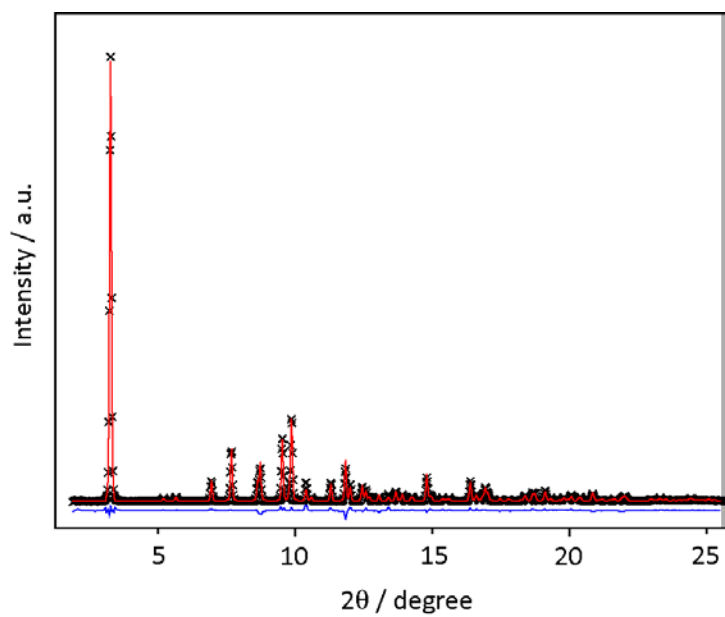
Fig. 113 - Synchrotron radiation diffractogram of VI dipeptide (black crosses), calculated Rietveld profile (red line) and difference plot (blue line)

App. C 2. Powder X-ray Diffraction (Synchrotron radiation) of dipeptide⊃PAN nanocomposites and Le Bail refinements
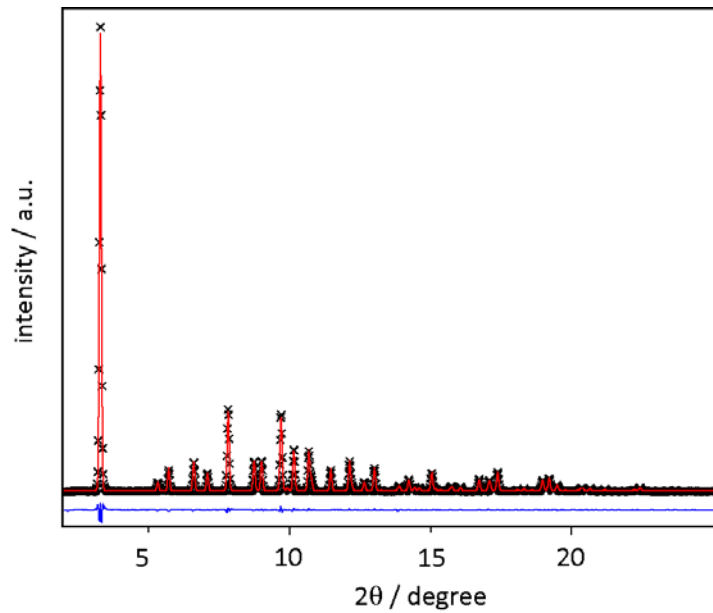
Fig. 114 - Synchrotron radiation diffractogram of AV ⊃ PAN nanocomposite (black crosses), calculated Le Bail profile (red line) and difference plot (blue line)
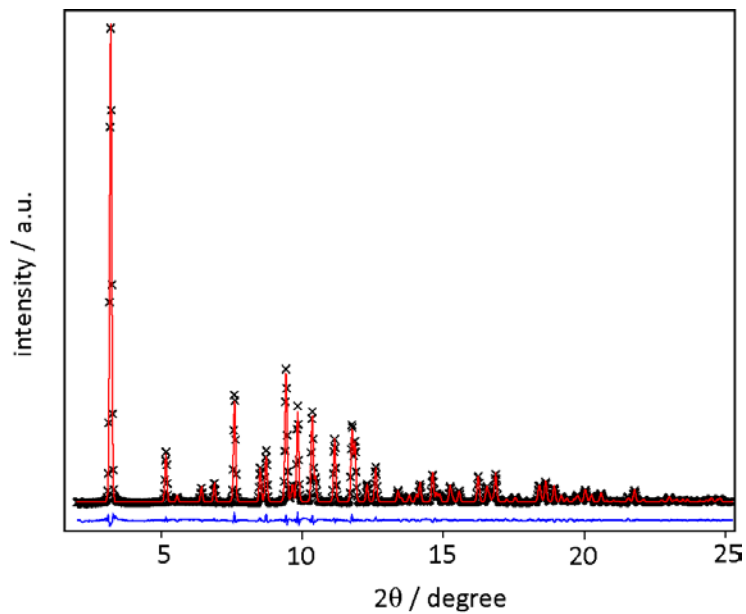
Fig. 115 - Synchrotron radiation diffractogram of IV ⊃ PAN nanocomposite (black crosses), calculated Le Bail profile (red line) and difference plot (blue line)
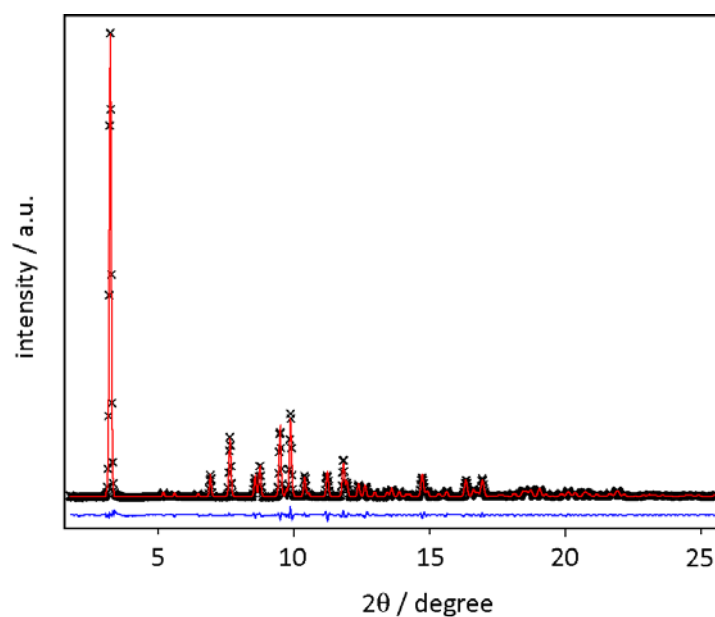
Fig. 116 - Synchrotron radiation diffractogram of VI⊃PAN nanocomposite (black crosses), calculated Le Bail profile (red line) and difference plot (blue line)

App. C 3. Powder X-ray Diffraction (Bragg-Brentano geometry) of dipeptide⊃PI nanocomposites and Le Bail refinements
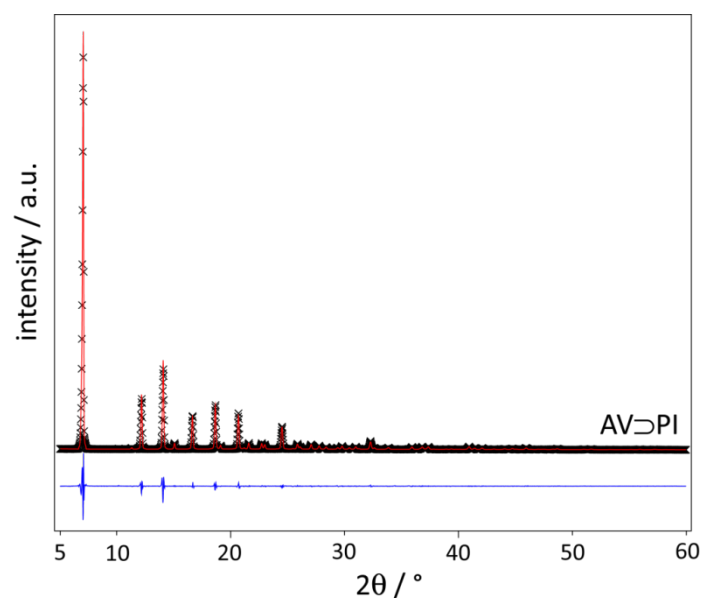
Fig. 117 - Diffractogram of AV⊃PI nanocomposite (black crosses), calculated Le Bail profile (red line) and difference plot (blue line)
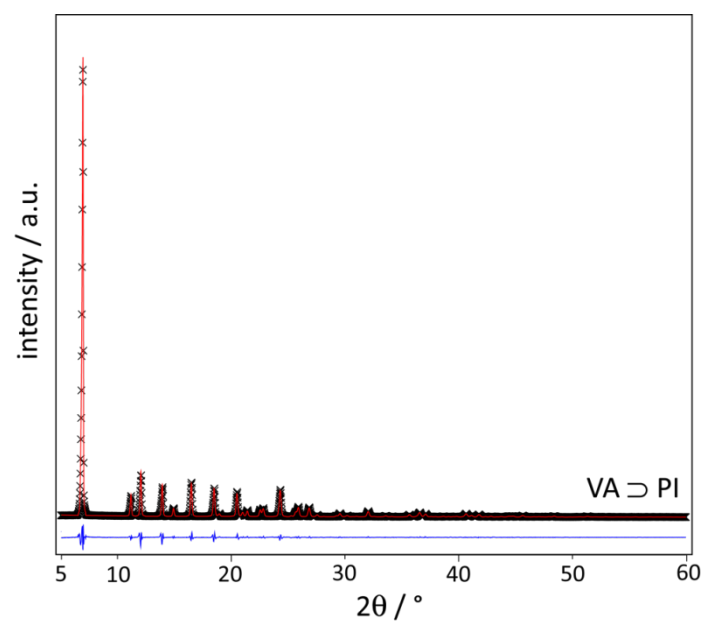
Fig. 118 - Diffractogram of VA ⊃ PI nanocomposite (black crosses), calculated Le Bail profile (red line) and difference plot (blue line)

App. C 4. Structural data and cell parameters of dipeptides and dipeptide⊃polymer nanocomposites

Table 12 - Room temperature crystal structure data and refined unit cell parameters of dipeptides and dipeptide PAN nanocomposites.

Compound	AV	AV PAN	IV	IV PAN	VI	VI PAN
Empirical formula	$C_8H_{16}N_2O_3$	$C_8H_{16}N_2O_3$ $(CH_2CHCN)_n$	$C_{11}H_{22}N_2O_3$	$C_{11}H_{22}N_2O_3$ $(CH_2CHCN)_n$	$C_{11}H_{22}N_2O_3$	$C_{11}H_{22}N_2O_3$ $(CH_2CHCN)_n$
Molecular mass / g mol^{-1}	188.2	-	230.3	-	230.3	-
Crystal system	Hexagonal	Hexagonal	Hexagonal	Hexagonal	Hexagonal	Hexagonal
Space group	$P6_1$	$P6_1$	$P6_1$	$P6_1$	$P6_1$	$P6_1$
a / Å	14.4448(5)	14.5697(2)	14.8787(6)	14.9787(2)	14.7892(5)	14.8758(5)
c / Å	10.0058(7)	9.9526(3)	10.3048(5)	10.2927(3)	10,3271(4)	10.2768(3)
Cell volume / Å^3	1808.0(2)	1829.43(7)	1975.6(1)	1999.89(7)	1956.2(1)	1969.4(2)
Z	6	6 (AV) and incommen-surate polymer	6	6 (IV) and incommen-surate polymer	6	6 (VI) and incommen-surate polymer
R_p / %	2.3	1.9	2.2	1.7	2.5	2.0
R_{wp} / %	4.5	2.9	3.6	2.0	3.9	2.8
N° observations	1659	1275	1473	1284	2073	2085

Table 13 - Room temperature crystal structure data and refined unit cell parameters of dipeptide PPD nanocomposites (Le Bail procedure)

Compound	AV PPD	IV PPD	VI PPD
Empirical formula	$C_8H_{16}N_2O_3 \ (C_5H_8)_n$	$C_{11}H_{22}N_2O_3 \ _n(C_5H_8)_n$	$C_{11}H_{22}N_2O_3 \ (C_5H_8)_n$
Crystal system	Hexagonal	Hexagonal	Hexagonal
Space group	$P6_1$	$P6_1$	$P6_1$
a / Å	14.5209(5)	15.1115(7)	15.0360(8)
c / Å	10.024(2)	10.304(2)	10.251(1)
Cell volume / Å^3	1830.6(3)	2037.8(3)	2007.1(3)
Z	6 (AV) and incommensurate polymer	6 (IV) and incommensurate polymer	6 (VI) and incommensurate polymer
R_p / %	16.38	14.32	14.86
R_{wp} / %	21.83	18.85	18.65
N° observations	2749	2749	2749

Table 14 – Room temperature structural data and refined unit cell parameters of dipeptide⊃PI nanocomposites (Le Bail procedure)

Compound	AV⊃PI	VA⊃PI
Empirical formula	$C_8H_{16}N_2O_3$ ⊐ $(C_5H_8)_n$	$C_8H_{16}N_2O_3$ ⊐ $(C_5H_8)_n$
Crystal system	Hexagonal	Hexagonal
Space group	$P6_1$	$P6_1$
***a* / Å**	14.5189(2)	14.5833(2)
***c* / Å**	9.9938(6)	10.0351(7)
Cell volume / Å³	1824.5(1)	1848.2(1)
Z	6 (AV) and incommensurate polymer	6 (VA) and incommensurate polymer
R_p / %	8.0	7.1
R_{wp} / %	10.1	10.0
N° observations	2749	2749

App. C 5.   Detailed TGA evaluation of nanocomposites

Table 15 – Estimation of experimental and maximum theoretical pore filling for dipeptide⊃PAN and dipeptide⊃PPD nanocomposites, according to TGA and crystallographic data.

Dipeptide⊃PAN nanocomposites													
Matrix	Pure matrix residue / %	Mass residue after main weight loss / % wt	Effective mass after main weight loss / % wt	Normalized starting PAN / % wt	PAN repetition length / Å	Channel repetition length / Å	Theoretical repeating PAN units per channel unit	Dipeptide molecular weight / Da	Channel unit molecular weight (Z=6) / Da	Molecular weight of PAN unit / Da	Theoretical PAN molecular weight / Da	Theoretical PAN - nanocomposite mass ratio / % wt	Pore filling / %
AV	0.7	13.8	13.1	14.6	2.5	10.71	4.28	188.2	1129.2	53.06	227.10	16.74	87
IV	0.7	8.1	7.4	8.2	2.5	11.80	4.72	230.3	1381.8	53.06	250.44	15.34	53
VI	0.5	10.5	10.0	11.1	2.5	10.51	4.20	230.3	1381.8	53.06	222.85	13.89	80
Dipeptide⊃PPD nanocomposites													
Matrix	Pure matrix residue / % wt	Mass residue after main weight loss / % wt	Effective PPD residue after main weight loss / % wt	PPD repetition length / Å	Channel repetition length / Å	Theoretical repeating PPD units per channel unit	Dipeptide molecular weight / Da	Channel unit molecular weight (Z=6) / Da	Molecular weight of PPD unit / Da	Theoretical PPD molecular weight / Da	Theoretical PPD - nanocomposite mass ratio / % wt	Pore filling / %	
AV	0.7	7.9	7.2	4.8	10.71	2.23	188.2	1129.2	68.12	151.91	11.86	61	
IV	0.7	5.6	4.9	4.8	11.80	2.46	230.3	1381.8	68.12	167.58	10.82	52	
VI	0.5	3.5	3.0	4.8	10.51	2.19	230.3	1381.8	68.12	149.18	9.74	31	

Dipeptide⊃PI nanocomposites												
Nanoporous matrix	Pure matrix residue / % wt	Mass residue after main weight loss / % wt	Effective PI residue after main weight loss / % wt	PI repetition length / Å	Channel repetition length / Å	Theoretical repeating PPD units per channel unit	Dipeptide molecular weight / Da	Channel unit molecular weight (Z=6) / Da	Molecular weight of PI unit / Da	Theoretical PI molecular weight / Da	Theoretical PI - nanocomposite mass ratio / % wt	Pore filling / %
AV	0.7	10.7	10	4.8	10.71	2.23	188.2	1129.2	68.12	151.91	11.86	84
VA	0.2	10.5	10.3	4.8	12.32	2.57	188.2	1129.2	68.12	175.07	13.42	77
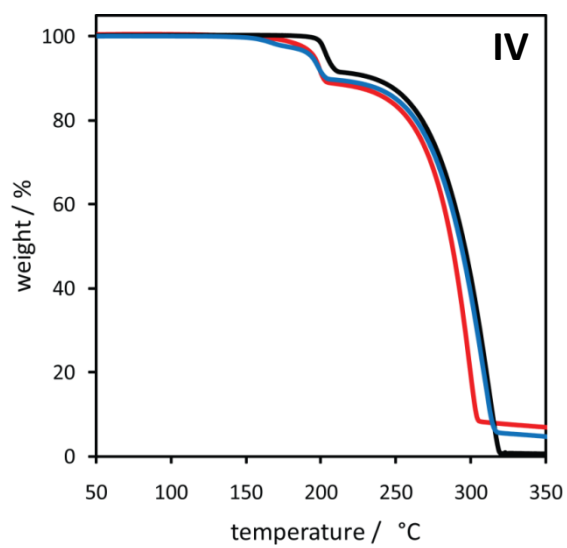
Fig. 119 – TGA profiles of IV (black), IV⊃PAN (red) and IV⊃PPD (blue) nanocomposites
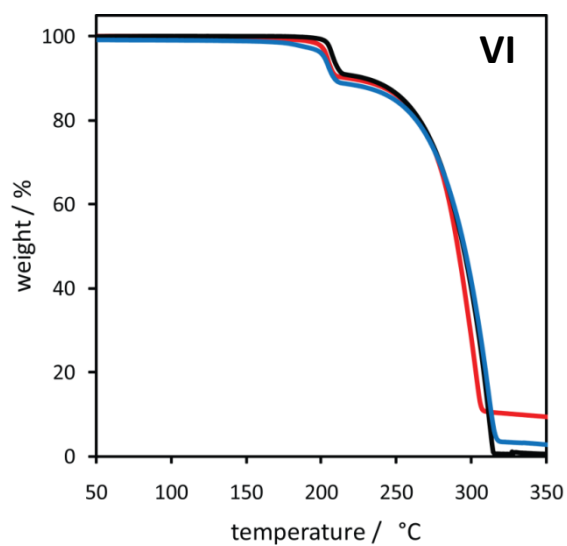
Fig. 120 – TGA profiles of VI (black), VI⊃PAN (red) and VI⊃PPD (blue) nanocomposites
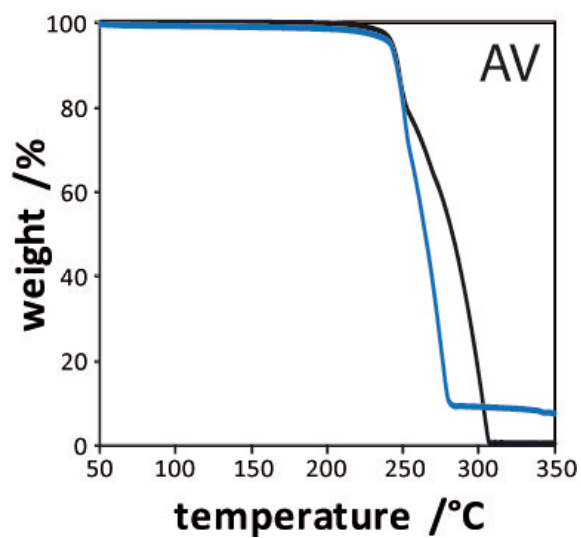
Fig. 121 - TGA profiles of AV (black), AV⊃PI (blue) nanocomposites
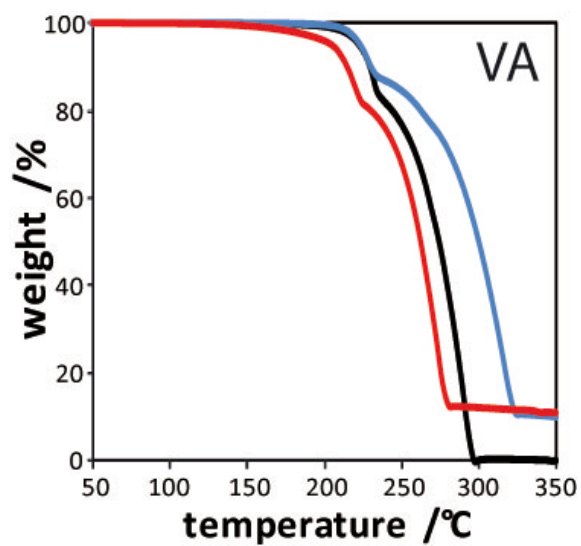
Fig. 122 – TGA profiles of VA (black), VA⊃PI (blue) and VA⊃PAN nanocomposites

App. C 6.   SS CP MAS ^{13}C NMR of dipeptides and nanocomposites
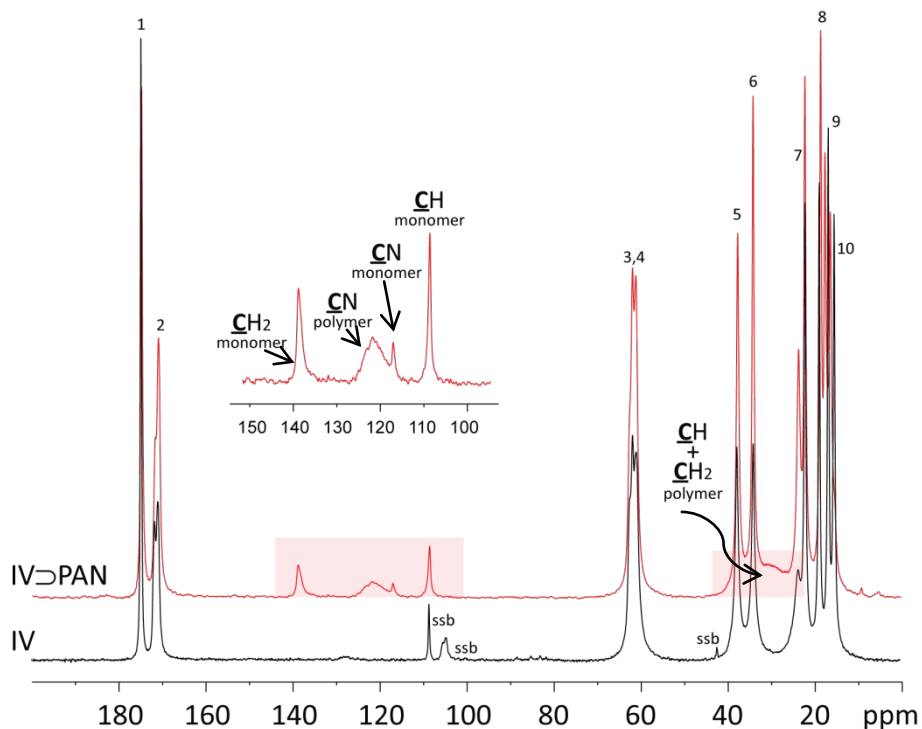
Fig. 123 – CP MAS ^{13}C NMR spectra of IV (black) and IV⊃PAN (red)
Experimental conditions:
IV: spinning speed 5 kHz, 2 ms contact time
IV⊃PAN: spinning speed 12.5 kHz, 2 ms contact time
"ssb" are spinning sidebands

	#	carbon	IV δ / ppm	IV⊃PAN δ / ppm
dipeptide	1	**C**OO$^-$ (V)	174.78	174.89
	2	**C**=O (I)	171.70 / 170.90	171.70 / 170.98
	3	α-**C**H (V) +	61.70	61.92
	4	α-**C**H (I)	60.88	61.17
	5	β-**C**H (I)	37.71	37.74
	6	β-**C**H (V)	33.96	34.19
	7	**C**H$_2$ (I)	23.63	23.71
	8	**C**H$_3$ (V)	22.03 / 18.77	22.26 / 18.64
	9	CH**C**H$_3$ (I)	16.69	17.64
	10	CH$_2$**C**H$_3$ (I)	15.33	16.42
PAN		**C**H$_2$	/	30 - 32
		CH	/	
		CN	/	121.70
AN		**C**H$_2$	/	138.85
		CH	/	108.61
		CN	/	117.03
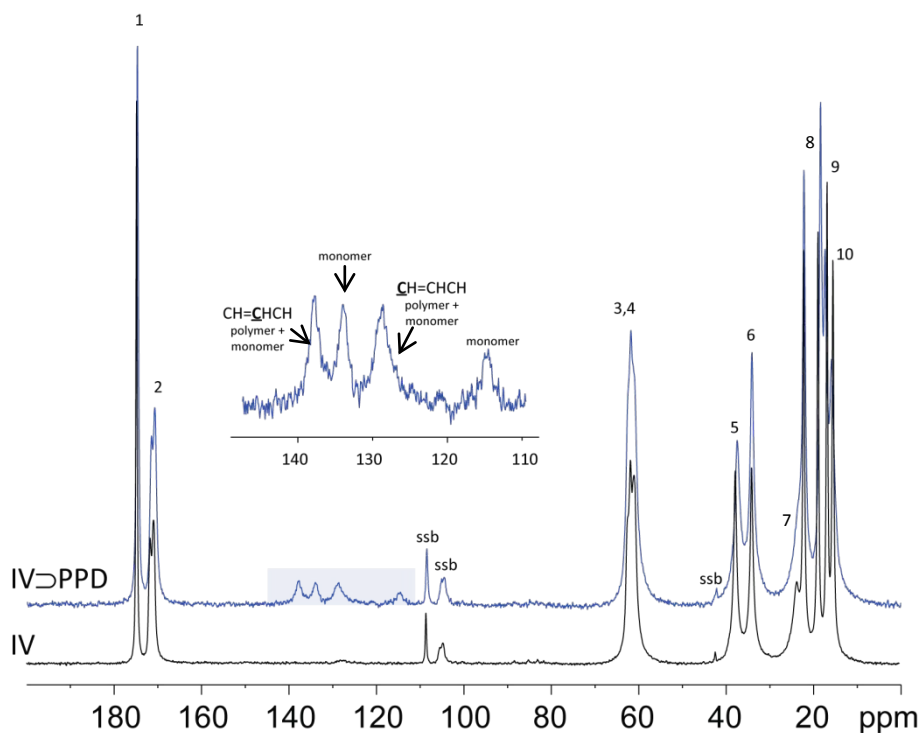
Fig. 124 - CP MAS 13C NMR spectra of IV (black) and IV⊃PPD (blue)
Experimental conditions:
IV: spinning speed 5 kHz, 2 ms contact time
IV⊃PPD: spinning speed 5 kHz, 2.5 ms contact time
"ssb" are spinning sidebands

	#	carbon	**IV** δ / ppm	**IV⊃PPD** δ / ppm
dipeptide	1	**C**OO⁻ (V)	174.78	174.82
	2	**C**=O (I)	171.70 170.90	171.59 170.84
	3	α-**C**H (V)	61.70	61.86
	4	α-**C**H (I)	60.88	(unresolved)
	5	β-**C**H (I)	37.71	37.53
	6	β-**C**H (V)	33.96	34.16
	7	**C**H₂ (I)	23.63	broad shoulder
	8	**C**H₃ (V)	22.03 18.77	22.25 18.46
	9	CH**C**H₃ (I)	16.69	17.44
	10	CH₂**C**H₃ (I)	15.33	15.95
PPD		**C**H=CHCH	/	137.84
		CH=**C**HCH	/	128.71
		CH=CH**C**H	/	"buried"
		CH₂	/	
		CH₃	/	

| | carbon | **IV⊃PPD** |
		δ / ppm
trans-1,3-PD	**C**H$_2$=CH	114.63
	CH$_2$=**C**H	137.84
	CH=CHCH$_3$	134.08
	CH=**C**HCH$_3$	128.71
	CH$_3$	"buried"

Fig. 125 – Comparison of the aliphatic regions of CP MAS ^{13}C NMR spectra of IV (black), IV⊃PAN (red) and IV⊃PPD (blue). Experimental conditions as indicated above
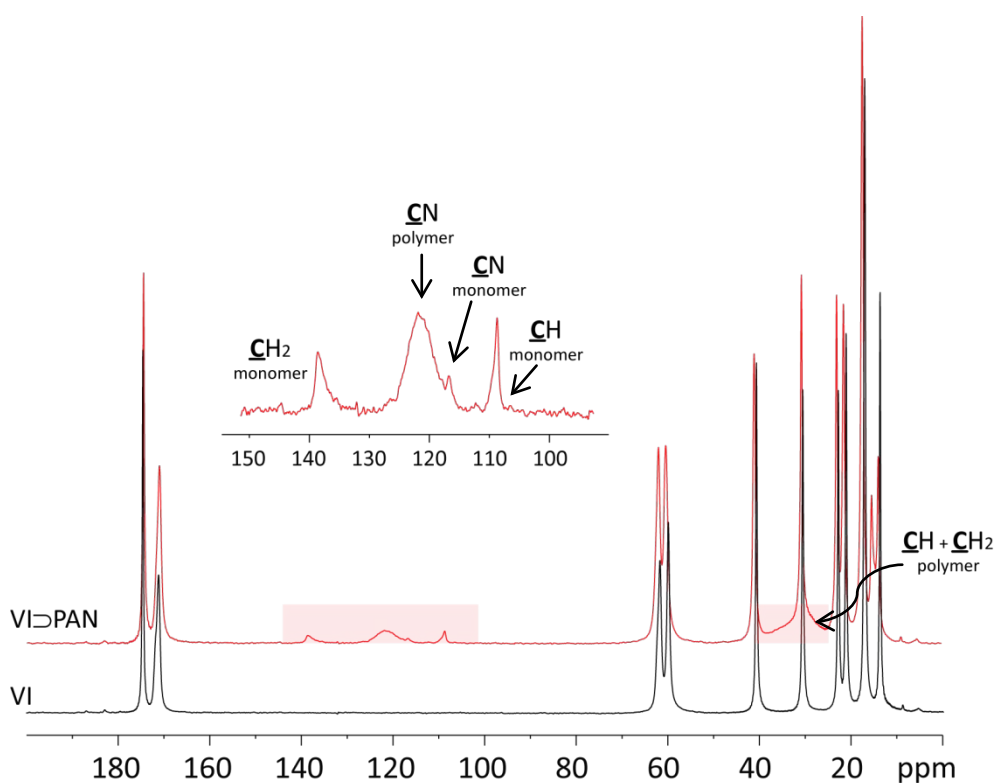
Fig. 126 - CP MAS ^{13}C NMR spectra of VI (black) and VI⊃PAN (red)
Experimental conditions:
VI: spinning speed 12.5 kHz, 2 ms contact time
VI⊃PAN: spinning speed 12.5 kHz, 2 ms contact time

	#	carbon	VI δ / ppm	VI⊃PAN δ / ppm
dipeptide	1	$\underline{C}OO^-$ (I)	174.56	174.54
	2	$\underline{C}$=O (V)	171.14	171.07
	3	α-$\underline{C}$H (I)	61.88	61.94
	4	α-$\underline{C}$H (V)	60.06	60.36
	5	β-$\underline{C}$H (V)	40.86	41.02
	6	β-$\underline{C}$H (I)	30.76	30.68
	7	$\underline{C}H_2$ (I)	23.02	22.99
	8	$\underline{C}H_3$ (V)	21.32 17.28 (superposed to CH$\underline{C}H_3$ ILE)	21.50 17.39 (superposed to CH$\underline{C}H_3$ ILE)
	9	CH$\underline{C}H_3$ (I)	17.28 (superposed to $\underline{C}H_3$ VAL)	17.39 (superposed to $\underline{C}H_3$ VAL)
	10	CH$_2\underline{C}H_3$ (I)	13.92	15.34 13.89
PAN		$\underline{C}H_2$	/	25-35 (broad)
		$\underline{C}H$	/	
		$\underline{C}N$	/	121.86
AN		$\underline{C}H_2$	/	108.69
		$\underline{C}H$	/	138.62
		$\underline{C}N$	/	116.75

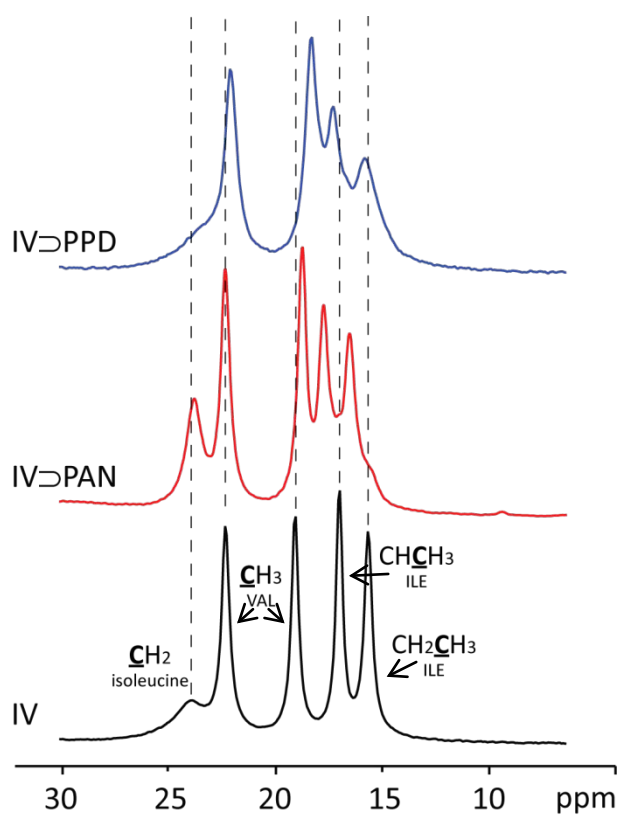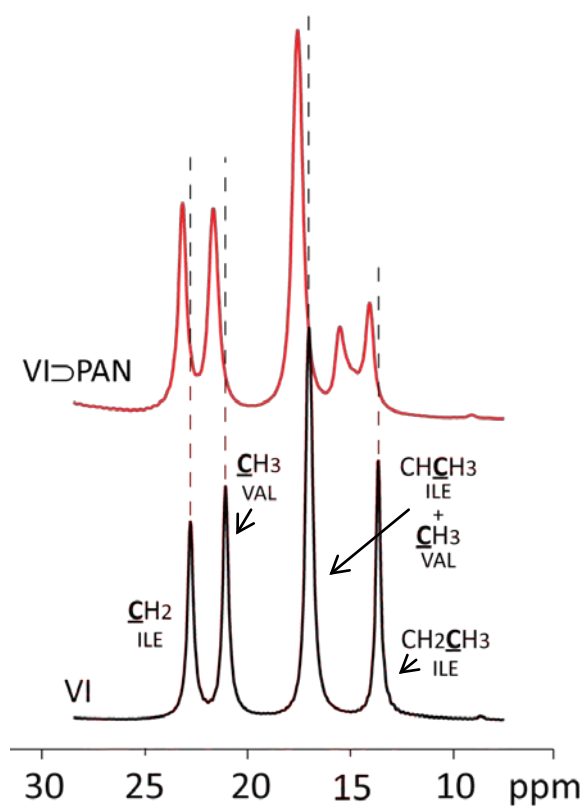**Fig. 127 – Comparison of the aliphatic regions of CP MAS ^{13}C NMR spectra of VI (black) and VI⊃PAN (red)**
Experimental conditions as indicated above

App. C 7. Liquid ¹H NMR of extracted 1,4-*trans*-polypentadiene
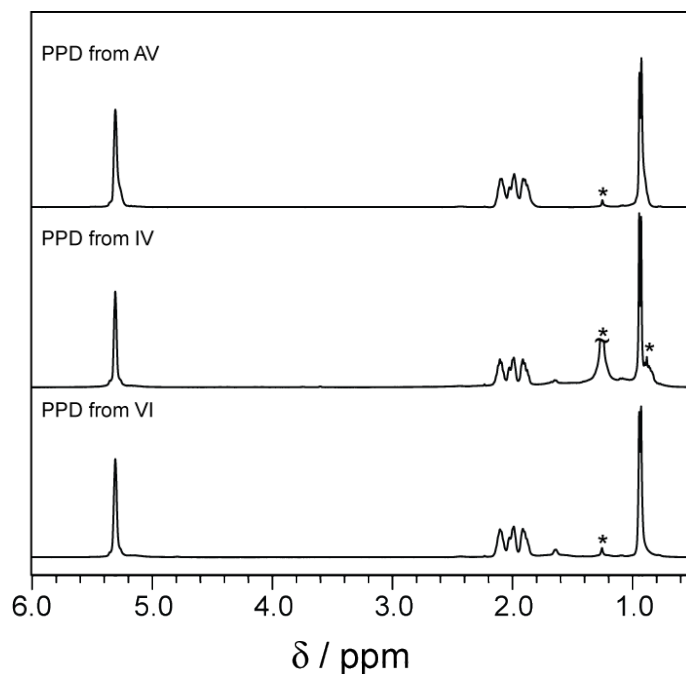
Fig. 128 – ¹H NMR (400 MHz, CDCl₃) spectra of 1,4-*trans*-polypentadiene obtained from AV (top), IV (middle) and VI (bottom) dipeptides. Asterisks designate trace impurities.

Table 16 - ¹H NMR assignments of 1,4-*trans*-polypentadienes obtained in AV, IV and VI
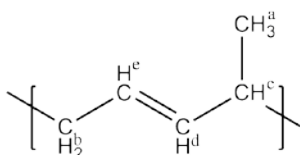
		PAN from AV		**PAN from IV**		**PAN from VI**	
¹H	Label	δ / ppm	Integral	δ / ppm	Integral	δ / ppm	Integral
C<u>H</u>₃	a	0.935 (d, J = 6.49 Hz)	3.00	0.934 (d, J = 6.52 Hz)	3.00	0.934 (d, J = 6.37 Hz)	3.00
C<u>H</u>₂	b	1.80 – 2.20 (b. m.)	3.02	1.80 – 2.20 (b. m.)	3.04	1.80 – 2.20 (b. m.)	2.92
C<u>H</u>	c						
C<u>H</u>	d	5.308 (b. m.)	2.08	5.310 (b. m.)	2.05	5.309 (b. m.)	2.01
C<u>H</u>	e						

153

App. C 8.   Viscosimetric Molecular Weight estimation of *in situ* polymerized PAN
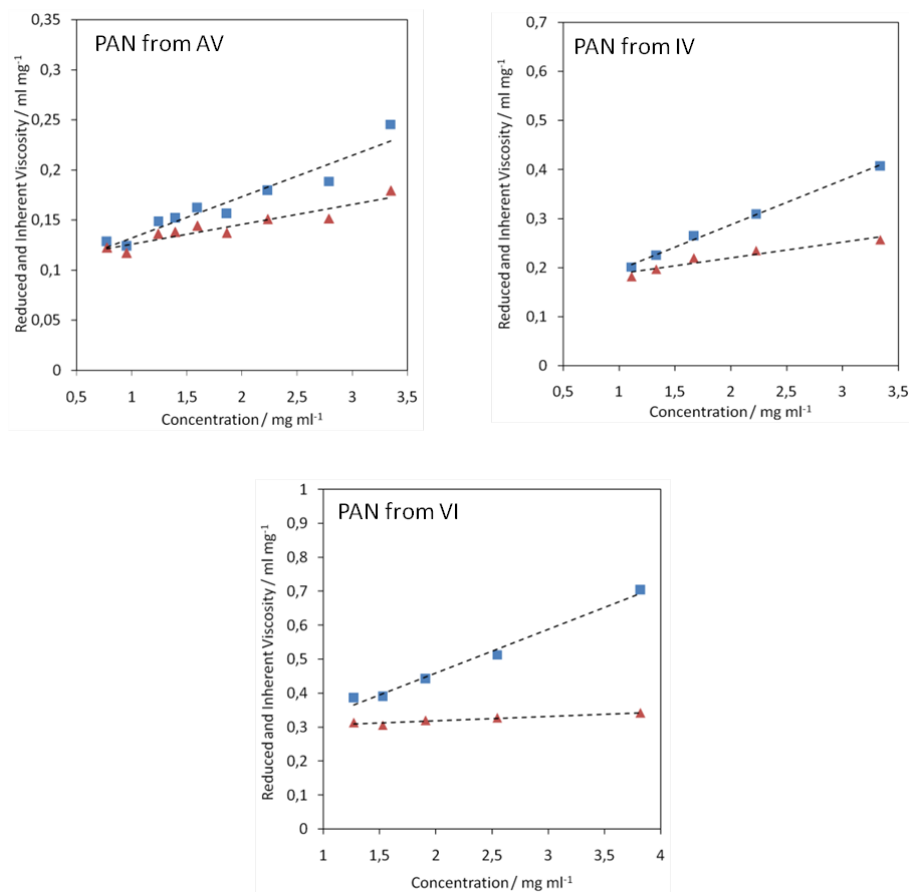
Fig. 129 - Reduced (red triangles) and Inherent (blue squares) Viscosity vs. Concentration for various AV (top left), IV (top right) and VI (bottom) polymerized PAN solutions in dimethylformamide (DMF) at room temperature

Table 17 – Summary of viscosimetric data and molecular weights for various *in situ* polymerized PAN samples

Nanoporous matrix	AV		IV		VI	
	Inherent viscosity	Reduced viscosity	Inherent viscosity	Reduced viscosity	Inherent viscosity	Reduced viscosity
Slope	0.041	0.019	0.032	0.091	0.012	0.128
Intercept / ml mg^{-1}	0.091	0.106	0.155	0.104	0.294	0.202
R^2	0.919	0.875	0.996	0.918	0.900	0.987
Mw$_v$ / kDa	~50	~60	~100	~60	~270	~160

App. C 9.   SEC-GPC measurements on PI from AV and VA
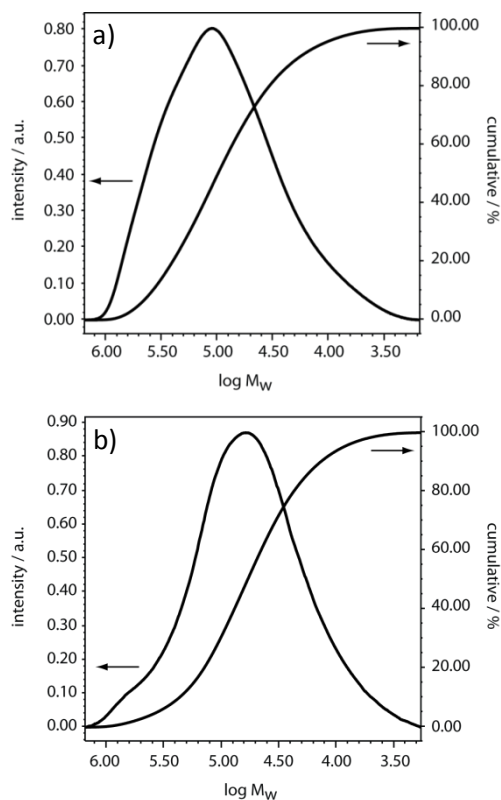
Fig. 130 - Gel Permeation Chromatography of 1,4-*trans*-polyisoprene polymerized in AV (a) and VA (b) after selective dipeptide dissolution.

Table 18 - Summary of GPC data on various in situ polymerized PI samples. Molecular weights are expressed in polystyrene equivalents.

Nanoporous matrix	AV	VA
M_w / kDa	156.0	103.9
M_n / kDa	42.7	31.5
Polydispersity index / $M_w M_n^{-1}$	3.65	3.30

App. C 11. Liquid ¹H NMR spectra of PAN from AV, IV and VI
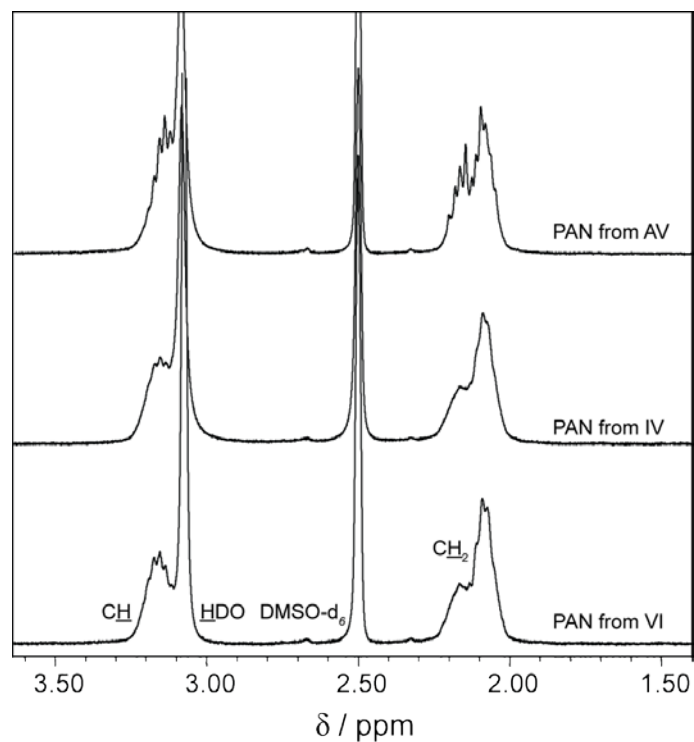
Fig. 131 - **¹H NMR spectra (100 MHz, DMSO-d₆) of PAN polymerized in AV (top), IV (middle) and VI (bottom) nanochannels.**

Table 19 – Assigment of PAN ¹H NMR signals
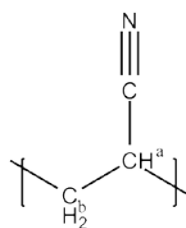
¹H	Label	PAN from AV	PAN from IV	PAN from VI
		δ / ppm		
C**H**	a	3.14 (broad m)	3.15 (broad m)	3.15 (broad m)
C**H**₂	b	2.00 – 2.25 (broad m)	2.00 – 2.25 (broad m)	2.00 – 2.25 (broad m)

App. C 12. Liquid ^{13}C NMR spectra of PAN from AV, IV and VI
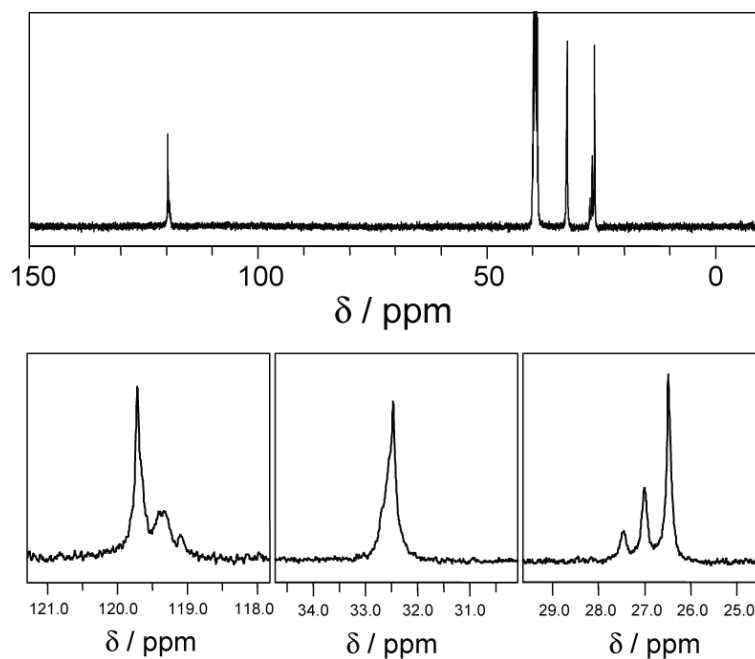
Fig. 132 – ^{13}C NMR (100 MHz, DMSO-d$_6$) spectrum of isotactic PAN polymerized in AV

Table 20 – Assignments and integrals of ^{13}C NMR spectrum of AV polymerized PAN

Label	^{13}C	triad	δ / ppm	Integral	
1	**C**H	*mm*-**C**H	26.49	0.59	
		mr-**C**H	27.00	0.29	1.00
		rr-**C**H	27.47	0.12	
2	**C**H$_2$	*mm*-**C**H$_2$ + *mr*-**C**H$_2$ + *rr*-**C**H$_2$	32.20 – 32.90 (broad asymmetric multiplet)	1.00	
3	**C**N	*rr*-**C**N	119.10	0.50	
		mr-**C**N	119.37		
		mm-**C**N	119.72		

App. C 13. Liquid ¹³C NMR spectrum of PAN from IV
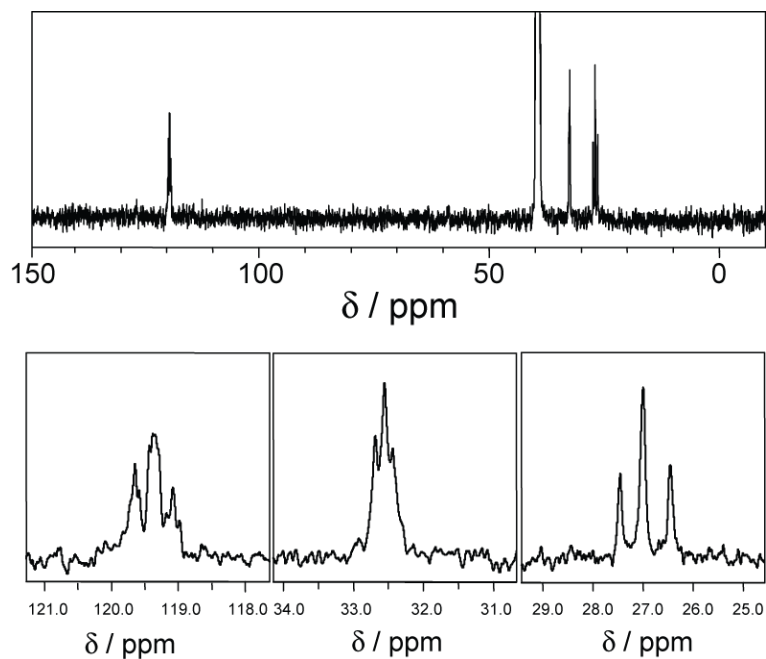
Fig. 133 – ¹³C NMR (100 MHz, DMSO-d₆) spectrum of atactic PAN polymerized in IV

Table 21 – Assignments and integrals of ¹³C NMR spectrum of IV polymerized PAN

label	¹³C	triad	δ / ppm	Integral	
1	**C**H	*mm*-**C**H	26.45	0.26	1.00
		mr-**C**H	26.99	0.52	
		rr-**C**H	27.45	0.22	
2	**C**H₂	*mm*-**C**H₂ + *mr*-**C**H₂ + *rr*-**C**H₂	32.20 – 32.90 (broad symmetric multiplet)	0.86	
3	**C**N	*rr*-**C**N	119.09	0.93	
		mr-**C**N	119.38		
		mm-**C**N	119.65		

App. C 14. Liquid ^{13}C NMR spectrum of PAN from VI
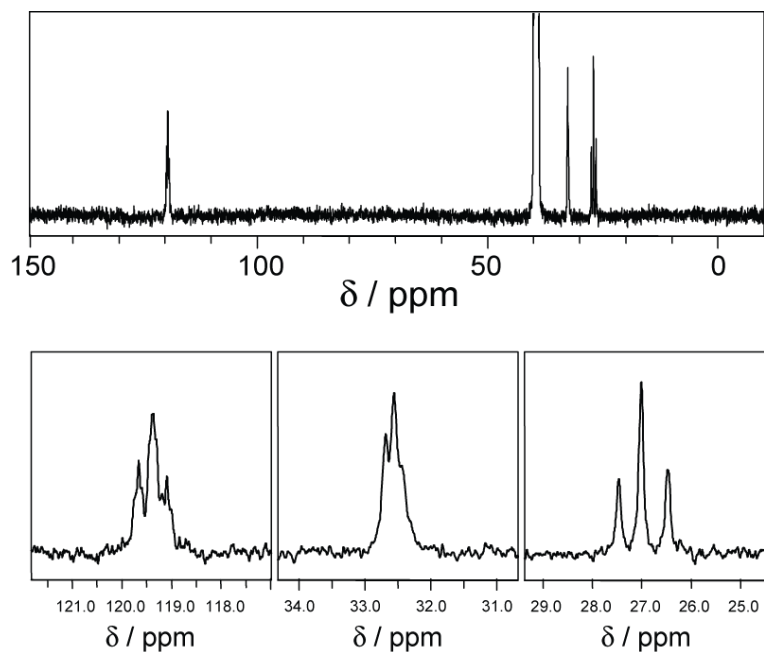
Fig. 134 – ^{13}C NMR (100 MHz, DMSO-d$_6$) spectrum of atactic PAN polymerized in VI

Table 22 – Assignments and integrals of ^{13}C NMR spectrum of VI polymerized PAN

label	^{13}C	triad	δ / ppm	Integral	
1	**C**H	*mm*-**C**H	26.48	0.26	1.00
		mr-**C**H	27.01	0.52	
		rr-**C**H	27.47	0.22	
2	**C**H$_2$	*mm*-**C**H$_2$ + *mr*-**C**H$_2$ + *rr*-**C**H$_2$	32.20 – 32.90 (broad symmetric multiplet)	0.96	
3	**C**N	*rr*-**C**N	119.09	1.07	
		mr-**C**N	119.39		
		mm-**C**N	119.66		

App. C 15. Liquid NMR ¹³C spectrum of PAN from VA
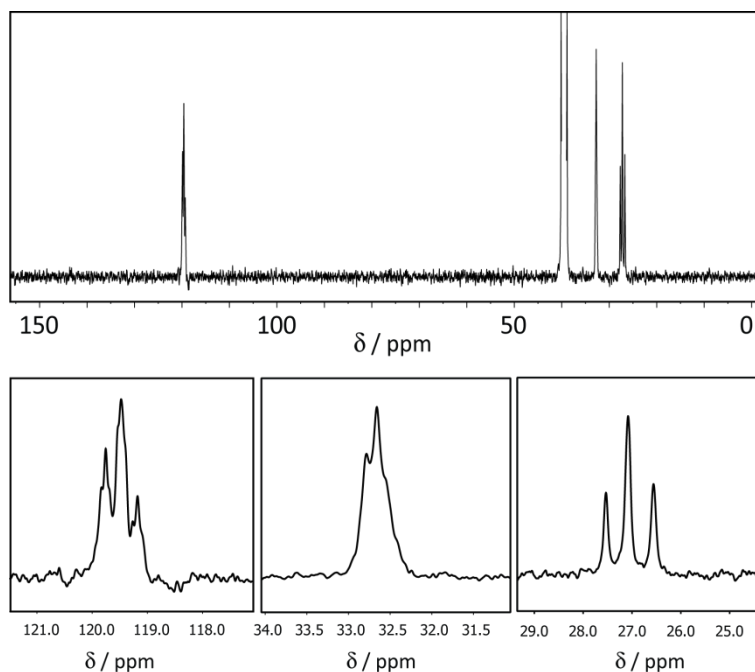
Fig. 135 – ¹³C NMR (100 MHz, DMSO-d₆) spectrum of atactic PAN polymerized in VA.

Table 23 – Assignments and integrals of ¹³C NMR spectrum of VA polymerized PAN

label	¹³C	triad	δ / ppm	Integral	
1	**C**H	*mm*-**C**H	26.49	0.27	
		mr-**C**H	27.01	0.51	0.98
		rr-**C**H	27.46	0.22	
2	**C**H₂	*mm*-**C**H₂ + *mr*-**C**H₂ + *rr*-**C**H₂	32.20 – 32.90 (broad symmetric multiplet)	0.97	
3	**C**N	*rr*-**C**N	119.10	1.07	
		mr-**C**N	119.39		
		mm-**C**N	119.67		

App. C 16. ^{1}H NMR spectra of PI polymerized in AV and VA
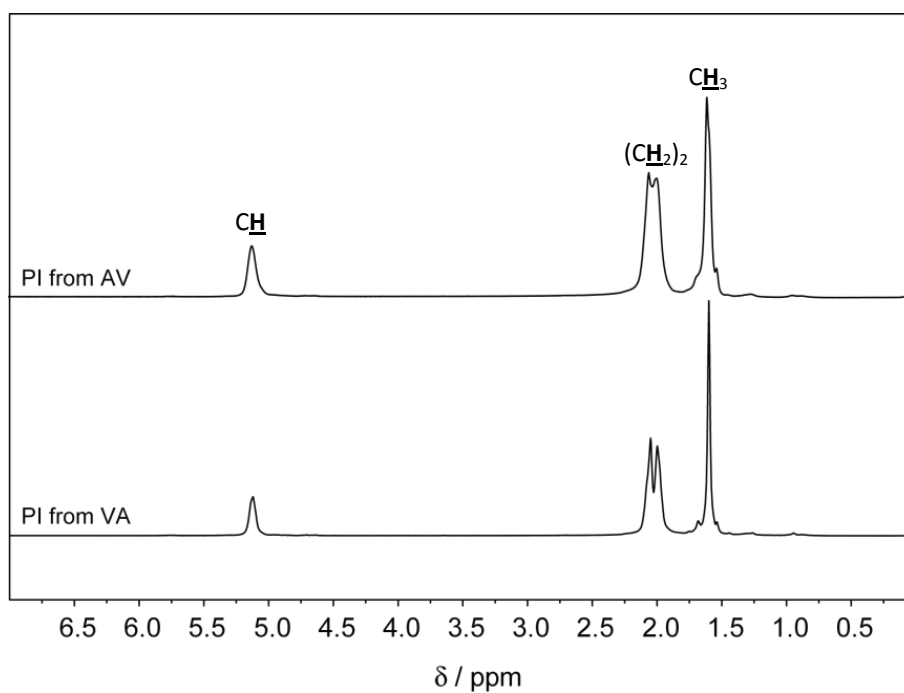
Fig. 136 - ^{1}H NMR (400 MHz, CDCl$_3$) spectra of PI polymerized in AV and VA

PI from AV: ^{1}H NMR (400 MHz, CDCl$_3$) δ 5.13 (1H, broad s, C**H**), 2.06 (2H, broad m, C**H**$_2$), 1.99 (2H, broad m, C**H**$_2$), 1.61 (3H, broad s, C**H**$_3$)

PI from VA: ^{1}H NMR (400 MHz, CDCl$_3$) δ 5.12 (1H, broad s, C**H**), 2.05 (2H, broad m, C**H**$_2$), 2.00 (2H, broad m, C**H**$_2$), 1.60 (3H, broad s, C**H**$_3$)

App. C 17. Liquid NMR spectrum of polyisoprene from VA
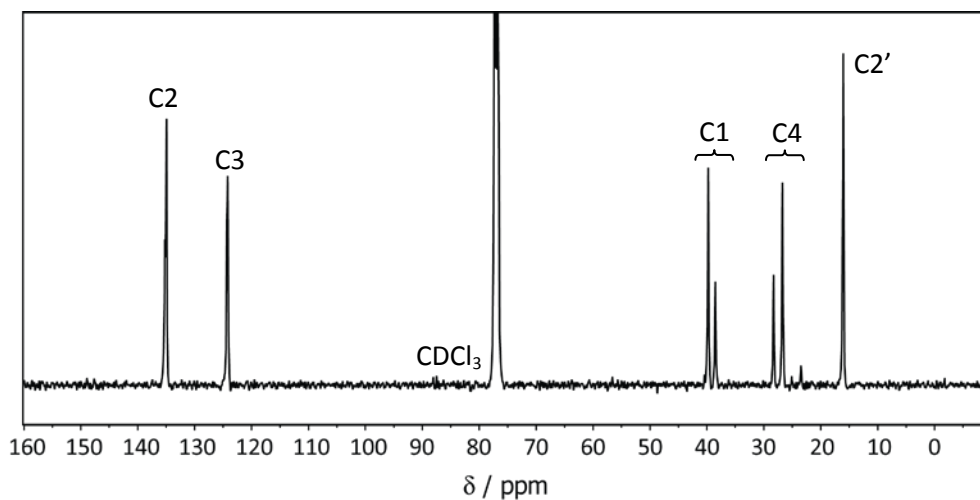
Fig. 137 – ^{13}C NMR spectrum of polyisoprene from VA nanochannels

Table 24 – Assignments, integrals and internal ratios between sequence-dependent contributions in PI obtained from VA nanochannels

label	^{13}C	sequence	δ / ppm	Integral	
C1	$\underline{C}H_2$	ht	39.75	0.90	0.68
		hh	38.50		0.32
C2	$\underline{C}(CH_3)=$	tt,hh	135.24	0.99	0.20
		tt,ht	135.11		0.14
		ht,hh	135.06		0.14
		ht,ht	134.93		0.52
C3	$=\underline{C}H$	-	124.20	0.96	
C4	$\underline{C}H_2$	tt	28.27	0.88	0.30
		ht	26.72		0.70
C2'	$\underline{C}H_3$	-	16.02	1.00	

App. C 18.   Variable temperature synchrotron radiation diffractograms of VI dipeptide
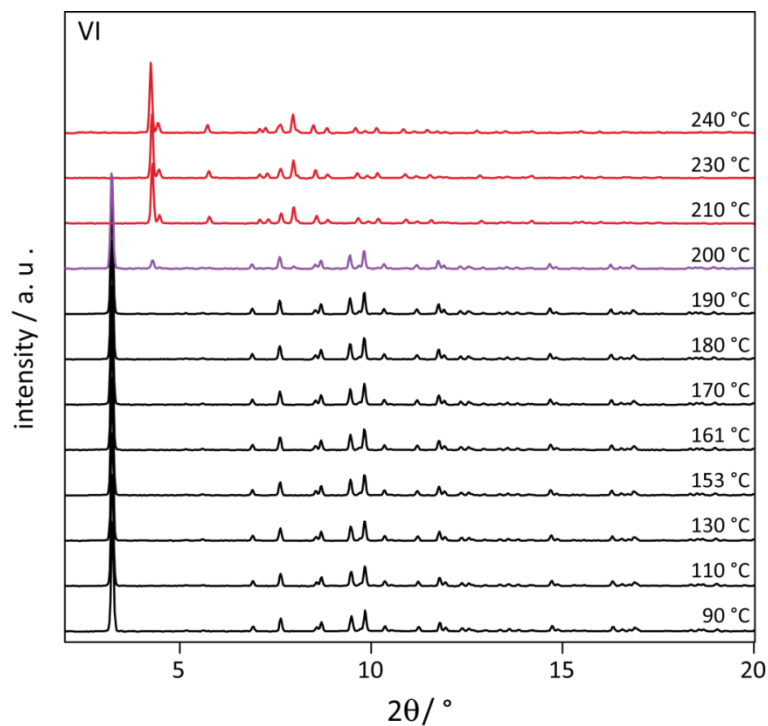
Fig. 138 – Series of variable temperature synchrotron radiation diffractograms performed on VI dipeptide. Thermal cyclization occurs at 200°C, in accordance to DSC data, with the appearance of the same high temperature phase as in IV thermal cyclization (see Fig. 98)

App. C 19. Atomic positions and bond lengths of thermal cyclic IV structure
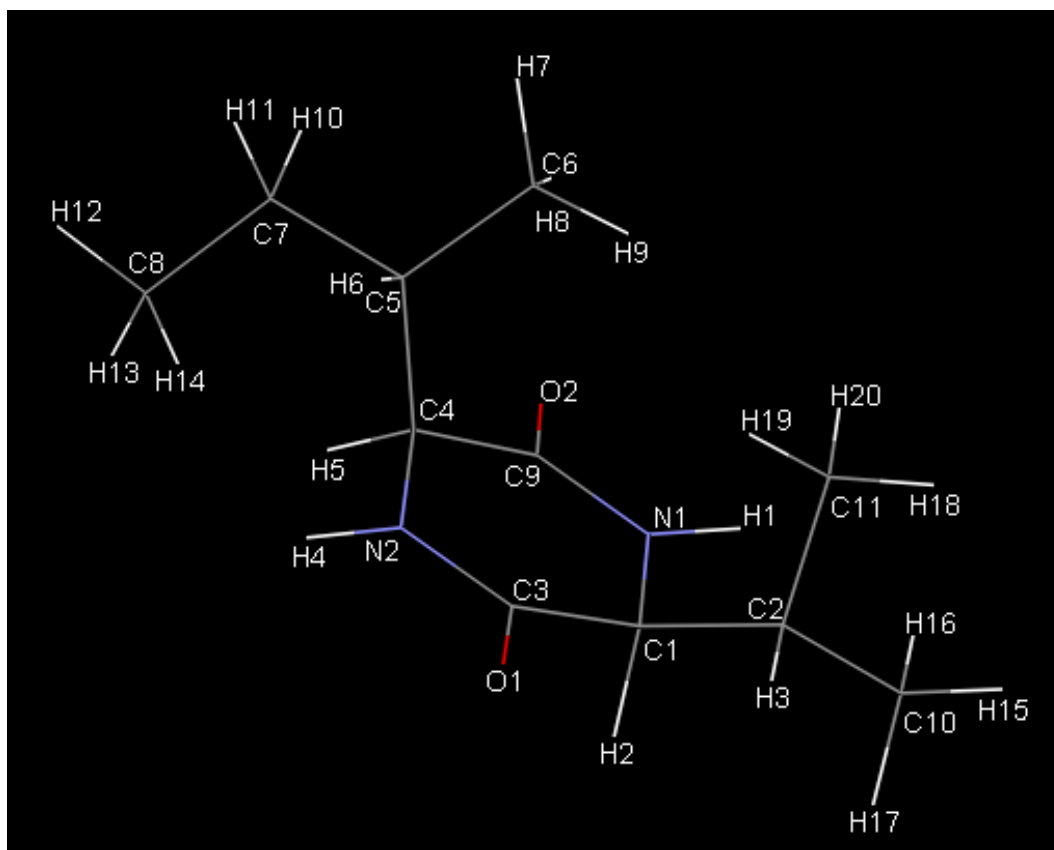
Fig. 139 - Molecular conformation and atomic labels of thermal cyclic IV

Table 25 – Atomic positions of the thermally cyclized L-isoleucyl-L-valine dipeptide structure

Number	Label	SybylType	Xfrac + ESD	Yfrac + ESD	Zfrac + ESD	Symm. op.
1	N1	N.am	0.18259	0.20083	0.62764	x,y,z
2	C1	C.3	0.36981	0.2676	0.65683	x,y,z
3	C2	C.3	0.36468	0.26397	0.74176	x,y,z
4	N2	N.am	0.59937	0.16956	0.56098	x,y,z
5	C3	C.2	0.59007	0.23664	0.62381	x,y,z
6	O1	O.2	0.75614	0.27578	0.64967	x,y,z
7	C4	C.3	0.41517	0.09702	0.53493	x,y,z
8	C5	C.3	0.47018	-0.04005	0.54284	x,y,z
9	C6	C.3	0.3159	-0.11187	0.59333	x,y,z
10	C7	C.3	0.48401	-0.10726	0.46831	x,y,z
11	C8	C.3	0.53817	-0.02628	0.40165	x,y,z
12	C9	C.2	0.19411	0.13303	0.56512	x,y,z
13	O2	O.2	0.02819	0.09983	0.53619	x,y,z
14	C10	C.3	0.17186	0.33552	0.77324	x,y,z
15	C11	C.3	0.36862	0.13345	0.77389	x,y,z
16	H1	H	0.03571	0.20451	0.65464	x,y,z
17	H2	H	0.36427	0.36518	0.63778	x,y,z
18	H3	H	0.51913	0.30303	0.76372	x,y,z
19	H4	H	0.74229	0.16977	0.53192	x,y,z
20	H5	H	0.38271	0.11916	0.47577	x,y,z
21	H6	H	0.64057	-0.05022	0.56288	x,y,z
22	H7	H	0.36782	-0.21009	0.59627	x,y,z
23	H8	H	0.14668	-0.10628	0.57111	x,y,z
24	H9	H	0.31976	-0.07181	0.65003	x,y,z
25	H10	H	0.32943	-0.15775	0.45821	x,y,z
26	H11	H	0.60549	-0.18349	0.4721	x,y,z
27	H12	H	0.54408	-0.08384	0.35097	x,y,z
28	H13	H	0.699	0.01822	0.41099	x,y,z
29	H14	H	0.41067	0.04566	0.3946	x,y,z
30	H15	H	0.17502	0.32992	0.83478	x,y,z
31	H16	H	0.01677	0.29508	0.75171	x,y,z
32	H17	H	0.18305	0.4331	0.75589	x,y,z
33	H18	H	0.36415	0.13872	0.83567	x,y,z
34	H19	H	0.51924	0.08584	0.75567	x,y,z
35	H20	H	0.2242	0.08191	0.7536	x,y,z

Table 26 – Interatomic bond lengths of the thermally cyclized L-isoleucyl-L-valine dipeptide structure

Number	Atom1	Atom2	Length / Å
1	N1	C1	1.4695(1)
2	N1	C9	1.3595(1)
3	N1	H1	1.0343(1)
4	C1	C2	1.5455(2)
5	C1	C3	1.5282(1)
6	C1	H2	1.1231(1)
7	C2	C10	1.5382(1)
8	C2	C11	1.5433(1)
9	C2	H3	1.1210(1)
10	N2	C3	1.3593(1)
11	N2	C4	1.4681(1)
12	N2	H4	1.0307(1)
13	C3	O1	1.2091(1)
14	C4	C5	1.5447(1)
15	C4	C9	1.5265(1)
16	C4	H5	1.1210(1)
17	C5	C6	1.5406(1)
18	C5	C7	1.5445(1)
19	C5	H6	1.1217(1)
20	C6	H7	1.1231(1)
21	C6	H8	1.1247(1)
22	C6	H9	1.1208(1)
23	C7	C8	1.5386(1)
24	C7	H10	1.1203(1)
25	C7	H11	1.1253(1)
26	C8	H12	1.1170(1)
27	C8	H13	1.1214(1)
28	C8	H14	1.1222(1)
29	C9	O2	1.2100(1)
30	C10	H15	1.1211(1)
31	C10	H16	1.1275(1)
32	C10	H17	1.1155(1)
33	C11	H18	1.1254(1)
34	C11	H19	1.1185(1)
35	C11	H20	1.1197(1)

App. C 20. Liquid ^{1}H NMR data of linear and cyclic dipeptides

Linear L-isoleucyl-L-valine (IV): ^{1}H NMR (400 MHz, MeOD, 45°C) δ 4.22 (1H, αC**H** ILE, d, J = 5.1 Hz), 3.73 (1H, αC**H** VAL, d, J = 5.2 Hz), 2.17 (1H, βC**H** VAL, dq, J = 13.1, 6.6 Hz), 1.93 (1H βC**H** ILE, m), 1.59 (1H, C**H**H ILE, m), 1.24 (1H, CH**H** ILE, m), 1.03 (3H, C**H**$_3$ VAL, d, J = 6.9 Hz), 0.98 (3H C**H**$_3$ VAL, d, J = 7.0 Hz), 0.96 (3H, C**H**$_3$ ILE, d, J = 5.8 Hz), 0.95 (3H, CH$_2$C**H**$_3$ ILE, t, J = 6.6 Hz)

cyclo(L-isoleucyl-L-valyl), thermally treated: ^{1}H NMR (400 MHz, MeOD, 45°C), δ 3.89 (1H, αC**H** VAL), 3.82 (1H, αC**H** ILE), 2.29 (1H, βC**H** VAL, dt, J = 7.1, 13.6), 1.98 (1H, βC**H** ILE, m), 1.55 (1H, C**H**H ILE, m), 1.27 (1H, CH**H** ILE, m), 1.05 (6H, C**H**$_3$ VAL, t, J = 8.2 Hz), 0.96 (3H, C**H**$_3$ ILE, d, J = 5.7 Hz), 0.94 (3H, CH$_2$C**H**$_3$ ILE, t, J = 7.1 Hz)

cyclo(L-isoleucyl-L-valyl), solution synthesis: ^{1}H NMR (400 MHz, MeOD, 45°C), δ 3.89 (1H, αC**H** VAL, dd, J = 1.7, 4.0 Hz), 3.82 (1H, αC**H** ILE, dd, J = 1.7, 4.1), 2.29 (1H, βC**H** VAL, dtd, J =4.2, 7.0, 13.9), 1.98 (1H, βC**H** ILE, m), 1.55 (1H, C**H**H ILE, m), 1.27 (1H, CH**H** ILE, m), 1.05 (6H, C**H**$_3$ VAL, dd, J = 7.1, 9.5 Hz), 0.96 (3H, C**H**$_3$ ILE, d, J = 6.8 Hz), 0.94 (3H, CH$_2$C**H**$_3$ ILE, t, J = 7.3 Hz)

Linear L-valyl-L-isoleucine (VI): ^{1}H NMR (400 MHz, MeOD, 45°C) δ 4.27 (1H, αC**H** VAL, d, J = 5.4 Hz), 3.66 (1H, αC**H** ILE, d, J = 5.5 Hz), 2.19 (1H, βC**H** ILE, m), 1.89 (1H βC**H** VAL, m), 1.59 (1H, C**H**H ILE, m), 1.22 (1H, CH**H** ILE, m), 1.05 (3H, C**H**$_3$ VAL, d, J = 6.9 Hz), 1.02 (3H, C**H**$_3$ VAL, d, J = 6.9 Hz), 0.96 (3H C**H**$_3$ ILE, d, J = 6.9 Hz), 0.93 (3H, CH$_2$C**H**$_3$ ILE, t, J = 7.4 Hz)

cyclo(L-valyl-L-isoleucyl) ≡ cyclo(L-isoleucyl-L-valyl), thermally treated VI: ^{1}H NMR (400 MHz, MeOD, 45°C), δ 3.89 (1H, αC**H** VAL, dd, J = 1.7, 4.0 Hz), 3.82 (1H, αC**H** ILE, dd, J = 1.8, 4.2), 2.30 (1H, βC**H** VAL, m), 1.98 (1H, βC**H** ILE, m), 1.55 (1H, C**H**H ILE, m), 1.27 (1H, CH**H** ILE, m), 1.05 (6H, C**H**$_3$ VAL, dd, J = 7.1, 9.5 Hz), 0.96 (3H, C**H**$_3$ ILE, d, J = 6.8 Hz), 0.94 (3H, CH$_2$C**H**$_3$ ILE, t, J = 7.5 Hz)

Linear L-valyl-L-valine (VV): ^{1}H NMR (400 MHz, MeOD, 45°C) δ 4.23 (1H, αC**H** VAL, d, J = 5.2 Hz), 3.66 (1H, αC**H** VAL, d, J = 5.3 Hz), 2.19 (2H, βC**H** VAL, m), 1.06 (3H, C**H**$_3$, d, J = 6.9 Hz), 1.02 (3H, C**H**$_3$, d, J = 6.9 Hz), 0.98 (3H, C**H**$_3$, d, J = 6.9 Hz), 0.96 (3H, C**H**$_3$, d, J = 6.9 Hz)

cyclo(L-valyl-L-valyl), thermally treated VV: ^{1}H NMR (400 MHz, MeOD, 45°C), δ 3.82 (2H, αC**H** VAL, d, J = 3.7 Hz), 2.29 (2H, βC**H** VAL, dh, J = 4.2, 6.8 Hz), 1.06 (6H, C**H**$_3$, d, J = 7.1 Hz), 0.96 (6H, C**H**$_3$, d, J = 6.8 Hz)

References

[1] M. Xu and R. V. Lewis, *PNAS*, Vol. 87, pp. 7120-7124, September 1990

[2] J. P. Mayer, F. Zhang and R. D. Di Marchi*, Peptide Science*, Vol. 88, 5, 687-713

[3] C. M. Joyce and S. J. Benkovic, *Biochemistry*, Vol. 43, No. 45, 2004, 14317 -14324

[4] R. Fairman and K. S. Åkerfeldt*, Current Opinion in Structural Biology*, 2005, 15, 453–463

[5] J. S. Mohammed and W. L. Murphy, *Adv. Mater.*, 2009, 21, 2361–2374

[6] J. C. M. van Hest *et al.*, *Chem. Commun.*, 2001, 1897–1904

[7] D. J. Adams and P. D. Topham, *Soft Matter*, 2010, 6, 3707–3721

[8] R. J. Mart *et al.*, *Soft Matter*, 2006, 2, 822–835

[9] L. Stryer *et al.*, *Biochemistry* (5ᵗʰ edition), W. H. Freeman ed., 2002

[10] J. F. Almine *et al.*, *Chem. Soc. Rev.*, 2010, 39, 3371–3379

[11] S. G. Wise *et al.*, *Int. J. Biochem. Cell Biol.*, 2009, 41, 494–497

[12] S. Dutoya *et al.*, *Biomaterials*, 2000, 21, 1521–1529

[13] Y. Yin *et al.*, *Biomaterials*, 2009, 30, 1675–1681

[14] L. Buttafoco *et al.*, *Biomaterials*, 27, 2006, 724-734

[15] H. A. Hosein *et al.*, *Langmuir*, 2004, 20, 10283

[16] K. T. Kim *et al.*, *Nanoscale*, 2010, 2, 844–858 and references within

[17] C. Pejoux *et al.*, *Small*, 2010, 6, 999

[18] T. Douglas *et al.*, *Nature*, 1998, 393, 152

[19] A. Sugawara *et al.*, *Angew. Chem. Int. Ed.* 2006, 45, 2876 –2879

[20] R. L. Brutchey *et al.*, *Chem. Rev.*, 2008, 108, 4915

[21] L. Z. Vilenchik *et al.*, *J. Am. Chem. Soc.* 1998**,** 120*,* 4290-4294

[22] A. L. Margolin *et al.*, *Angew. Chem. Int. Ed.* 2001, 40, 2204 – 2222

[23] C. M. Wong, *Appl. Microbiol. Biotechnol.*, 2008, 78, 927–938

[24] G. Liu, *Electrochemistry Communications,* 8, 2006, 251–256

[25] J. C. M. van Hest *et al., Chem. Commun.*, 2001, 1897–1904

[26] Y. Qu *et al.*, JACS, 2000, 122, 5014-5015

[27] C. L. Nykiforuk, *Plant Biotechnology Journal*, 2006, 4, pp. 77–85

[28] R. B. Merrifield, *J. Am. Chem. Soc.*, 1963, 85, (14), 2149–2154

[29] S. Zhang, *Biotechnology Advances*, 20, 2002, 321–339

[30] S. Zhang *et al.*, PNAS, 1993, 90, pp. 3334-3338

[31] M. Altman *et al.*, *Protein Science*, 2000, 9, 1095–1105

[32] S. Zhang *et al.*, *Biomaterials*, 20, 1999, 1213-1220

References

[33] S. Vauthey *et al.*, PNAS, 2002, 99 5355–5360

[34] M. G. Ryadnov and D. N. Woolfson, *Angew. Chem.*, 2003, 115, 3129 – 3131

[35] E. F. Banwell, E. S. Abelardo, D. J. Adams, M. A. Birchall, A. Corrigan, A. M. Donald, M. Kirkland, L. C. Serpell, M. F. Butler and D. N.Woolfson, *Nature Materials*, VOL 8, JULY 2009, 596-600

[36] J.K. Kretsingera, L. A. Hainesa, B. Ozbasb, D. J. Pochanb and J. P. Schneidera, *Biomaterials*, 26 (2005) 5177–5186

[37] M. R. Ghadiri *et al.*, *Nature*, 1993, 366, 324

[38] *R. J. Brea et al., Chem. Soc. Rev., 2010, 39, 1448–1456*

[39] *M. Reches and E. Gazit, Science,* 25 april 2003, vol 300, 625-627

[40] T. H. Han, J. Kim, J. S. Park, C. B. Park, H. Ihee and S. O. Kim, *Adv. Mater.*, 2007, 19, 3924–3927

[41] Y. Song, .S. R. Challa, C. J. Medforth, Y. Qiu, R. K. Watt, D. Peña, J. E. Miller, F. van Swol and J. A. Shelnutt, *Chem. Commun.*, 2004, 1044-1045

[42] M Reches and E. Gazit, *Nano Lett.,* 2004, Vol. 4, No. 4, 581-585

[43] N. Sanchez de Groot, T. Parella, F. X. Aviles, J. Vendrell and S. Ventura, *Biophysical Journal*, 2007, 92(5), 1732-1741

[44] *C. H. Gørbitz, Acta Cryst., 2010, B66, 84–93*

[45] C. H. Gørbitz, *Chem. Eur. J.*, 2007, 13, 1022−1031

[46] C. H. Gørbitz, *Acta Cryst.*, 2002, B58, 849-854; I. G. Efimova, *Protection of Metals and Physical Chemistry of Surfaces*, 2009, Vol. 45, No. 5, pp. 525-528

[47] D. V. Soldatov *et al.*, JACS, 2006, 128, 6737-6744

[48] C.H. Cheng *et al.*, JACS, 2007, 129, 13997-14002

[49] H. Zhang *et al.*, JACS, 2008, 130, 17846–17857

[50] S. A. Moggach, *CrystEngComm*, 2010, 12, 2322–2324

[51] A. Comotti *et al.*, *Chem. Comm.*, 2009, 284–286

[52] R. J. Fletterick *et al.*, *J. Phys. Chem.*, 1971, 75 (7), 918-922

[53] R. V. Afonso *et al.*, *Angew. Chem. Int. Ed.*, 2010, 49, 3034 −303

[54] A. Y. Robin and K. M. Fromm, *Coordination Chemistry Reviews*, 2006, 250, 2127–2157

[55] N. W. Ockwig *et al.*, *Acc. Chem. Res.*, 2005, 38, 176-182

[56] S. Horike *et al.*, *Nature Chemistry*, VOL 1, DECEMBER 2009, 695-704

[57] N. B. McKeown, *J. Mater. Chem.*, 2010, 20, 10588-10597

[58] G. Couderc and J. Hulliger, *Chem. Soc. Rev.*, 2010, 39, 1545–1554

[59] J. D. Figueroa, *International Journal of Greenhouse Gas Control*, 2, 2008, 9-20

[60] S. Cavenati *et al.*, *Energy & Fuels*, 2006, 20, 2648-2659

[61] S. Sircar, *Ind. Eng. Chem. Res.*, 2002, 41, 1389-1392; S. Sircar, *Ind. Eng. Chem. Res.*, 2006, 45, 5435

[62] A. Comotti *et al.*, *Chem. Commun.*, 2009, 284–286

References

[63] B. Wang *et al.*, *Nature*, 2008, 453, 207; Y.-S. Bae *et al.*, *Chem. Commun.*, 2008, 4135

[64] P. Sozzani and G. Di Silvestro, *Polymerization in Clathrates* in *Comprehensive Polymer Science*, G. C. Eastmond, Pergamon, London, 1998

[65] P. Enzel et al., *Chem. Mater.*, 1992, 4, 819-824

[66] T. Uemura *et al.*, *Macromolecules*, 2008, 41 (1), 87-94; T. Uemura *et al.*, *Chem. Soc. Rev.*, 2009, 38, 1228–1236; T. Uemura *et al.*, *Top. in Curr. Chem.* 2010, 293, 155-173

[67] D. M. White, *J. Am. Chem. Soc.*, 1960, 82, 5678; M. Minagawa *et al.*, *Macromolecules*, 1992, 25, (2), 1992

[68] F. Shaeper et al., J. Am. Chem. Soc., 2004, 126, 2114-2124; P. Yang *et al.*, *Organometallics*, 2004, 23, 2752-2761

[69] M. Minagawa *et al.*, *Macromolecules*, 2001, 34, 3679 - 3683

[70] C. H. Goerbitz, *Acta Cryst.*, 2002, B58, 849-854

[71] D. V. Soldatov et al., *J. Am. Chem. Soc.* 2006, 128, 6737 – 6744

[72] K. Katsuraya *et al.*, *Polymer*, 42, 2001, 6323-6326

[73] F. C. Schilling *et al.*, *Macromolecules*, Vol. 24, No. 15, 1991

[74] S. J. Heyes *et al.*, *Macromolecules*, 1992, 25, 3617-3623

[75] H. E. Gottlieb *et. al.*, *J. Org. Chem.*, 1997, 62 (21), 7512–7515

[76] G. Gatti *et al.*, *Makromol. Chem.*, 1974, 175, 1627

[77] L. Zetta *et al.*, *Macromolecules*, Vol. 11, No. 4, July-August, 1978

[78] K. F. Elgert *et al.*, *Makromol. Chem.*, 1976, 177, 2021

[79] M. Farina *et al.*, *Macromolecules*, Vol. 3, No. 5, September- October 1970, 475 – 480

[80] I. W. Bassi *et. al.*, *Macromolecules*, Vol. 4, No. 5, September-October 1971, 575 – 579

[81] M. Surianarayanan *et al.*, *J. Polym. Sci., Part A: Polym. Chem.*, 1998, 36, 2503 – 2512

[82] P. H. Lindenmeyer *et al.*, *J. Appl. Phys.*, 1963, 34, 42

[83] M. Minagawa *et al.*, *Macromolecules*, 2001, 34, 3679-3683

[84] K. Matsuzaki *et al.*, *J. Polym. Sci.*, 1968, 6, 1475

[85] H. R. Allcock *et al.*, *Macromolecules*, 1985, 18, 1324-1330

[86] K. Tajima *et al.*, *Chem. Commun.*, 2000, 2399–2412

[87] K. T. Jung *et al.*, *Materials Letters*, 53, 2002, 180–185

[88] H. R. Allcock *et al.*, *Macromolecules*, 1994, 27, 7550–7555

[89] L. Yeo *et al., Acta Crystallogr. Sect B Struct. Sci.*, 1997, 53, 822

[90] A. Bondi, *J. Phys .Chem.*, 68, 441-452, 1964

[91] J.E. Puskas *et al.*, *Prog. Polym. Sci.*, 31, 2006, 533–548

[92] P. H. Liang *et al.*, *Eur. J. Biochem.*, 2002, 269, 3339–54

[93] C. Bazzini *et al.*, *Macromol. Rapid Commun.*, 2002, 23, No. 15

References

[94] P. Sozzani *et al.*, *Macromolecules*, 1984, 17 (12), 2532-2538

[95] G. Di Silvestro *et al.*, *Macromolecules*, 1987, 20, 999

[96] K. Takamura and D. Urban*, Polymeric Dispersions and Their Industrial Applications*, Wiley-VCH, Weinheim 2002

[97] D. Dendukuri *et al., Adv. Mater.*, 2009, 21, 1–16

[98] J.A. Champion *et al*., *Journal of Controlled Release*, 121, 2007, 3–9

[99] S. Freiberg *et al.*, *International Journal of Pharmaceutics*, 282, 2004, 1–18

[100] P. Sozzani *et al.*, *Nature Materials,* 5, 545 – 551, 2006

[101] M. Surianarayanan et al., *Polym. Sci., Part A: Polym. Chem, Vol. 36, 2503–2512, 1998*

[102] Z. Bashir, Carbon, 29, 8, 1081-1090, 1991

[103] E. Fitzer, *Carbon*, 27, 5, 621-645, 1989

[104] M. Minagawa *et al.*, *J. Appl. Pol. Sci.*, 79, 473–478, 2001

[105] F. Tuinstra *et al.*, *J. Chem. Phys.*, 53, 3, 1970, 1126 - 1130

[106] Y. Kawashima *et al.*, *Phys. Rev. B*, 59, 62-64, 1999

[107] E. B. Barros *et al.*, *Phys. Rev. B*, 71, 165422, 2005

[108] L. G. Cançado *et al.*, *Appl. Phys. Lett.*, 2006, 88, 163106

[109] M. S. Dunn *et al.*, *J. Biol. Chem.*, 1932, 99, 221-229

[110] R. M. Silverstein, F. X. Webster, D. Kiemle, *Spectrometric Identification of Organic Compounds*, Wiley 2005, 99-104

[111] B.C. Gerstein *et al.*, *Modern Magnetic Resonance*, Springer 2008, 363-371

[112] A. Shoji *et al.*, *Annual Reports on NMR Spectroscopy*, Volume 45, 2002, 69-150

[113] R. S. Macomber, *A complete introduction to modern NMR spectroscopy*, Wiley 1998, 82-85

[114] K. D. Kopple *et al.*, *J. Org. Chem.*, 1968, 33 (2), 862–864

[115] C. H. Görbitz, *New J. Chem.*, 2003, 27, 1789–1793

[116] A. Altomare *et al.*, *J. Appl. Cryst.*, 2009, 42, 1197-1202

[117] Y. Zhu *et al.*, *International Journal of Quantum Chemistry*, Vol 107, 745–753, 2007

[118] C. H. Görbitz *et al.*, *Acta Cryst.*, 2006, E62, o2358-o2360

[119] A.C. Larson and R.B. Von Dreele, "General Structure Analysis System (GSAS)", *Los Alamos National Laboratory Report LAUR*, 1994, 86 – 748

[120] B. H. Toby, "EXPGUI, a graphical user interface for GSAS", *J. Appl. Cryst.* 2001, 34, 210-213

[121] R. Degeilh *et al., Acta Cryst.*, 1959, 12, 1007

[122] S. Palacin *et al*, *J. Am. Chem. Soc.*, 1997, 119*,* 11807-11816

[123] T.-J. M. Luo *et al.*, *J. Phys. Org. Chem.*, 2000, 13, 870–879

[124] R. Taylor *et al.*, *Acc. Chem. Res.*, 1984, 17, 320-326

[125] C. H. Görbitz *et al.*, *Acta Crystallogr. Sect. E*, 2006, 62, o2358-o2360

References

[126] D. V. Soldatov *et al.*, *J. Am. Chem. Soc.*, 2006, 128, 6737 – 6744

[127] J. Rodriguez-Carvajal, *Physica B.*, 1993, 192, 55

[128] J. Rodriguez-Carvajal and T. Roisnel, *International Union for Crystallography*, Newletter N 20 (May-August) Summer 1998

[129] J. laugier and B. Bochu, LMGP-Suite, Suite of Programs for the interpretation of X-ray Experiments, ENSP/Laboratoire des Matériaux et du Génie Physique, BP 46. 38042 Saint Martin d'Hères, France. WWW: http://www.inpg.fr/LMGP and http://www.ccp14.ac.uk/tutorial/lmgp/

[130] Y. Inoue *et al.*, *Polymer Journal*, 1972, 3, 2, 149-152

[131] K. Kamide *et al.*, *Polym. J.*, 1985, 17, 607 – 619

[132] G. A. Zickler *et al.*, *Carbon*, 2006, 44, 3239 – 3246

[133] F. Tuinstra et *al.*, *J. Chem. Phys.*, 1970, 53, 1126; F. Tuinstra *et al.*, *J. Compos. Mater.* 1970, 4, 492; L. G. Cancado *et al.*, *Appl. Phys. Lett.*, 2006, 88, 163106

[134] Persistence of Vision Pty. Ltd. (2004), Persistence of Vision Raytracer (Version 3.6) [Computer software]. Retrieved from http://www.povray.org/download/

[135] W.S. Rasband, ImageJ, U. S. National Institutes of Health, Bethesda, Maryland, USA, http://imagej.nih.gov/ij/, 1997-2011.

[136] C. F. Macrae *et al.*, *J. Appl. Cryst.,* 2008, 41, 466-470